DYNAMIC COUPLING AND CHEMICAL TRANSPORT BETWEEN THE STRATOSPHERE AND THE TROPOSPHERE

A Dissertation

Presented to the Faculty of the Graduate School

of Cornell University

in Partial Fulfillment of the Requirements for the Degree of

Doctor of Philosophy

by

Huang Yang

August 2015

DYNAMIC COUPLING AND CHEMICAL TRANSPORT BETWEEN THE STRATOSPHERE AND THE TROPOSPHERE

Huang Yang, Ph.D.

Cornell University 2015

Although the stratosphere and troposphere are separately different in many aspects (thermal structure, dynamic circulation, chemical composition and etc.), studies in recent decades have indicated a much stronger connection between these two distinct layers. Dynamically, the stratospheric circulation is driven by the eddies that are dominantly generated in the troposphere, whereas the troospheric circulation varies, in some ocassion, mostly due to the circulation and eddy perturbation originated in the stratosphere. The exchange and transport between the two layers, on the other hand, tend to alter the chemical compostion on both sides, and hence induce subsequent influences on the chemistry and radiation within the two layers. In this study, we further enrich the understanding on the connection between the stratosphere and troposphere by examining their dynamic coupling and chemical exchange.

We first investigate the dynamic impact from the troposphere to the stratosphere by examining the role of tropical sea surface temperature (SST). By designing several idealized SST forcing simulations in an aqua-planet model, we find that the zonal distribution of SST perturbations has a major impact on the vertical and meridional structure of the BDC as compared with other SST characteristics. Zonally localized SST heatings tend to generate a shallow acceleration of the stratospheric residual circulation, whereas SST heatings with a zonally symmetric structure tend to produce a deep strengthening of the

stratospheric residual circulation. The shallow versus deep strengthening of the stratospheric residual circulation change has been linked to wave propagation and dissipation in the subtropical lower stratosphere rather than wave generation in the troposphere.

The dynamic impact from the stratosphere to the troposphere is then discussed by focusing on the downward influence of polar stratospheric ozone depletion. Three possible mechanisms are examined in an idealized dry model: the polar stratospheric cooling impacts tropospheric synoptic eddies via (a) the direct influences on the lower stratospheric synoptic eddies, (b) the planetary wave-induced residual circulation, and (c) the planetary eddy - synoptic eddy nonlinear interaction. It is argued that the planetary wave-induced residual circulation is not the dominant mechanism, and that the planetary eddies and further nonlinear interaction with synoptic eddies are more likely the key to the downward influence of the ozone depletion-like cooling.

Last, the chemical interaction between the stratosphere and troposphere is explored by quantifying the stratosphere-troposphere exchange (STE) of ozone. The specified dynamics (SD) version of the Whole Atmosphere Community Climate Model (WACCM) is used to estimate the ozone STE along different isentropic surfaces (isentropic ozone STE herein). Net troposphere-to-stratosphere ozone STE is diagnosed in the subtropics (350 K - 380 K), while net stratosphere-to-troposphere ozone STE is diagnosed in the extratropics (280 K - 350 K), with different magnitudes and seasonalities over different isentropic (meridional) regions. Potential vorticity (PV) sources induced by both differential diabatic heating and isentropic mixing contribute to the diagnosed isentropic ozone STE flux, but the latter is slightly larger. Moreover, results in the SD-WACCM are generally consistent with the analysis in a different model, the SD version of

the Canadian Middle Atmosphere Model (CMAM), but the SD-CMAM diagnoses a smaller STE flux. This difference is associated with the different extent of isentropic mixing between the two models.

BIOGRAPHICAL SKETCH

Huang Yang came from Changsha, China. During his high school years, he found his interest in earth sciences and potential in physics. That becomes his initial motivation to pursue an academic career in the Atmospheric Sciences, an interdisciplinary field with both his beloved two subjects deeply involved. Upon graduation from high school, he enrolled at the Nanjing University in the School of Atmospheric Sciences and earned a Bachelor Degree of Science in Meteorology through four years of study there. At his senior year, he got the opportunity to work with Prof. Ming Bao to investigate the remote forcing, from the Indian Ocean, on the anomalies in the East-Asia monsoon by a case study in summer 1991. This research helped him attain the basic understanding about large-scale climate dynamics as well as strengthen his belief to devote himself further onto this amazing subject. In the meantime, he had been accepted by the Department of Earth and Atmospheric Sciences at Cornell University. After the summer 2010, he flew half of the hemisphere to reach town of Ithaca, and worked as a graduate student with Prof. Gang Chen ever since on the project of stratosphere-troposphere interaction, which turns into the topic of this dissertation.

To Mom and Dad, and to my old neighbor and lifelong friend, Ms. Mei Yuan, who opened a young boy‘s heart to geosciences by a gift of globe at his tenth birthday. Salute to our marvelous atmosphere.

ACKNOWLEDGEMENTS

I would like to first present my deepest appreciation to my adviser Prof. Gang Chen. It is him who led me into this spectacular field of upper troposphere and lower stratosphere (UTLS), who taught me how to research, how to think, and how to live better. Without him, I would not have gone this far, and this smoothly. I would also like to thank my special committee members Profs. Stephen Colucci, Peter Diamessis and Peter Hess. Prof. Colucci attended the weekly reading group, offered a wide variety of ideas and comments for my research, and Prof. Hess assisted me a lot on the atmospheric chemistry and transport.

I also would like to acknowledge Drs. Lantao Sun, Qi Tang and Daniela Domeisen for their endless helps on the collaborated projects. And thanks to al the faculties, staffs, and my fellow graduate students (or undergrads) Michael Kelleher, David Alex Burrows, Aaron Perry, Aaron Match, Yun Zheng, Wenxiu Sun, Rachel Scanza, Flora Min, Andrew Montreuil, Thomas Ehrmann, Ryan Sullivan, Xiaolu Li, Dimitris Hernandez, Michael Roman, Stephen Jessup and Marcus Walter for your memorable company for the past five years.

Of course, mom and dad, always be the people I should appreciate most.

TABLE OF CONTENTS

LIST OF TABLES

LIST OF FIGURES

CHAPTER 1

INTRODUCTION

1.1 Distinct stratosphere and troposphere

The stratosphere and troposphere are the two closest atmospheric layers to the Earth's surface with the stratosphere laying above the troposphere. The stratosphere became departed from the troposphere since the finding of an isothermal layer of around 11-14 km, which is later called as the 'tropopause', by Léon Teisserenc de Bort and Richard Assmann in 1902 (Hoinka, 1997, and references therein). The troposphere is characterized by a negative lapse rate (decrease of temperature with height), with a large potential for atmospheric instability and convection. Consequently, most of the synoptic phenomena (e.g. hurricanes and storms) occur in this layer. In contrast, the stratosphere is demarcated by a general positive lapse rate (increase of temperature with height) due to the shortwave (SW) radiation absorption by the stratospheric ozone (Stocker et al., 2001). Thus, the stratosphere is thermally stable, with the horizontal motion significantly larger than the vertical motion.

On the dynamic aspect, the troposphere and stratosphere possess significantly different circulation patterns, and the atmospheric waves act to influence these atmospheric circulations via the wave-mean flow interaction (Andrews et al., 1987). These waves spread on a broad range of scales, including the planetary eddies due to large-scale topography and land-sea contrast, the synoptic eddies due to regional baroclinic instability, and even the gravity eddies due to finer orographic perturbation or diabatic processes at smaller scales. We can use the Elliassen-Palm (EP) flux to infer the location of where these waves are gen-

erated (flux divergence) and dissipated (flux convergence). It has been shown that most of the atmospheric waves are generated in the lower troposphere and dissipated in the upper troposphere. A frequently unstable troposphere with a negative Brunt-Väisälä frequency N^2, favors the vertical propagation of eddies at most of scales throughout the vertical column of the troposphere. By contrast, normally stable stratosphere with a positive N^2 suppresses the vertical propagation of eddies at smaller scales. Therefore, all of the planetary eddies, synoptic eddies and gravity eddies are active in the troposphere to drive the tropospheric circulation, whereas the synoptic eddies are largely damped in the stratosphere and are only active in the lowermost stratosphere. The planetary eddies is then the major dynamic forcing in driving the stratospheric circulation. Furthermore, the gravity eddies, albeit weak, tend to contribute essentially to emerge the meridional circulation in the stratosphere (Butchart et al., 2014).

The troposphere and stratosphere are additionally different in chemical composition. The troposphere comprises about 80% of the total atmospheric air mass. Thus, most of the important chemical species, of which have an substantial climate effect (e.g. water vapor, carbondioxide, methane and etc.), are much higher in concentration in the troposphere than that in the stratosphere. The most noticeable exception is the ozone, as the photochemical cycle in the stratosphere provides as the largest source for atmospheric ozone (Chapman, 1930). The difference in chemical composition between the two layers further enhances their difference in other aspects via complicated climate interplay among radiation, dynamics and chemistry. For instance, The abundant stratospheric ozone is crucial resulting in the distinctly stable thermal structure of the stratosphere. Higher concentration of water vapor makes the tropospheric circulation moist, especially over the regions where convection is robust. Contrarily, the strato-

spheric circulation is relatively dryer due to the lack of moisture.

1.2 Coupled two layers

The large discrepancy between the troposphere and the stratosphere may arise an impression that these two distinct layers are highly isolated from each other, and thus are lack of interaction. However, there is increased evidence that the troposphere is substantially coupled with the stratosphere via various dynamic and chemical feedbacks, despite the fact that this coupling is relatively weaker than the internal interaction among tropospheric systems.

Meridional circulations and jet streams are important large-scale dynamic features in the atmosphere that relates to major climate variabilities (e.g. global warming, El niño and etc.) as well as significant synoptic events. Fig. 1.1 summarizes the major meridional circulations and jet streams in the troposphere and stratosphere. In the troposphere, the meridional circulation is composed of three cells, including the Hadley cell in (sub)tropics, the Ferrel cell in mid-latitudes and the polar cell in high-latitudes. The subtropical jet situates at the poleward edge of the Hadley cell, resulting from the Coriolis effect diverting the poleward transport of air mass along the upper branch of the Hadley cell eastward. In the meantime, roughly at the boundary between the Ferrel cell and the polar cell, the polar front jet is formed due to the cyclonic-eddies related heat and momentum transport in the polar front region and these westerlies can reach the surface. Observation shows that these two tropospheric jet streams are geographically merged in most seasons in a year. In the stratosphere, the meridional circulaiton is characterized by the Brewer-Dobson circulation (BDC). At

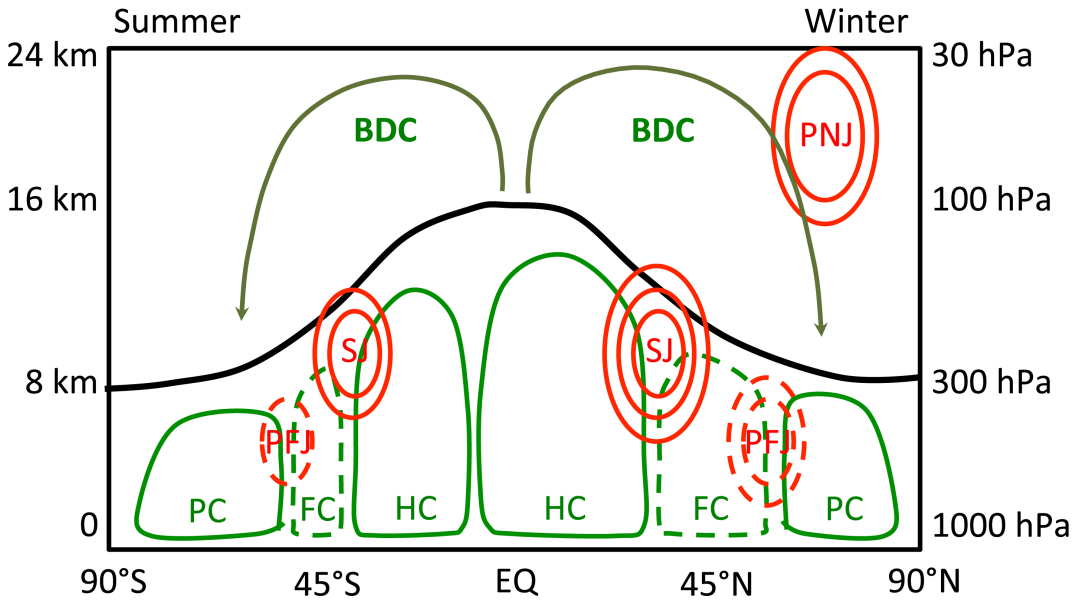

Figure 1.1: Schematic showing major meridional circualtions and jet streams in the stratosphere and the troposphere. Acronyms in the figure are listed below as: HC for Hadley Cell, FC for Ferrel Cell, PC for Polar Cell, SJ for Subtropical Jet, PFJ for Polar Front Jet, BDC for Brewer-Dobson Circulation, and PNJ for Polar Night Jet

its shallow branch within the lowermost stratosphere, hemispherically one cell is observed with upwelling in deep tropics and downwelling in extratropics. At higher altiudes (in the upper stratosphere, not shown), the BDC can evolve into a global one-cell structure, transporting air mass upward slightly towards the summer hemisphere and downward in the extratropical winter hemisphere. Furthermore, polar night jets are emerged in the winter hemisphere surrounding the superbly cooled stratospheric polar vortex. Despite the difference, the stratospheric circulation is dynamically connected with the tropospheric circulation via atmospheric waves that can propagate across the tropopause, or diabatic processes that overshoots pumping momentum and energy from the troposphere to the stratosphere.

On one hand, the stratospheric circulation is strongly influenced by the eddy perturbation originated in the troposphere. Fig. 1.2 shows that, following the downward control principle (Haynes et al., 1991), the stratospheric BDC is driven by an extratropical pump of planetary eddies linking to tropospheric baroclinic zones (Holton et al., 1995) and a tropical pump of planetary and gravity eddies associated with tropospheric deep convection (Norton, 2006). Furthermore, these eddy or convection anomalies result from the large-scale climate variability in the troposphere and have been suggeted to accelerate the BDC within recent decades, such as the long-term trend of greenhouse gases (GHG) induced global warming (Garcia and Randel, 2008), and the interannual events of El Niño and Southern Oscillation (ENSO) (Calvo et al., 2010). Also, Sjoberg and Birner (2012) document that the sudden stratospheric warming (SSW) events are normally preceded by strong heat flux anomalies in the troposphere, and the Arctic sea ice might play an important role in it (Sun et al., 2015).

On the other hand, strong stratospheric pertubation can act to alter the tropospheric circulation. Fig. 1.3 gives the example on how the sudden stratospheric warming (SSW) can exert a downward influence on the tropospheric circulation by weakening the Northern Annular Mode (NAM). Along with these anomalies in the NAM, the tropospheric jet tends to decelerate and shift equatorward (Lee and Feldstein, 2013). Note that the SSW is often preceded by anamolous high heat flux events in the troposphere, suggesting the stratosphere-troposphere dynamic coupling can be more complicated. Moreover, Kolstad et al. (2010) suggests that weak polar vortex events in the stratosphere can interact with the Northern Annular Mode (NAM) and the Northern Atlantic Oscillation (NAO) in the troposphere, and cause extreme cold air outbreak events near the surface

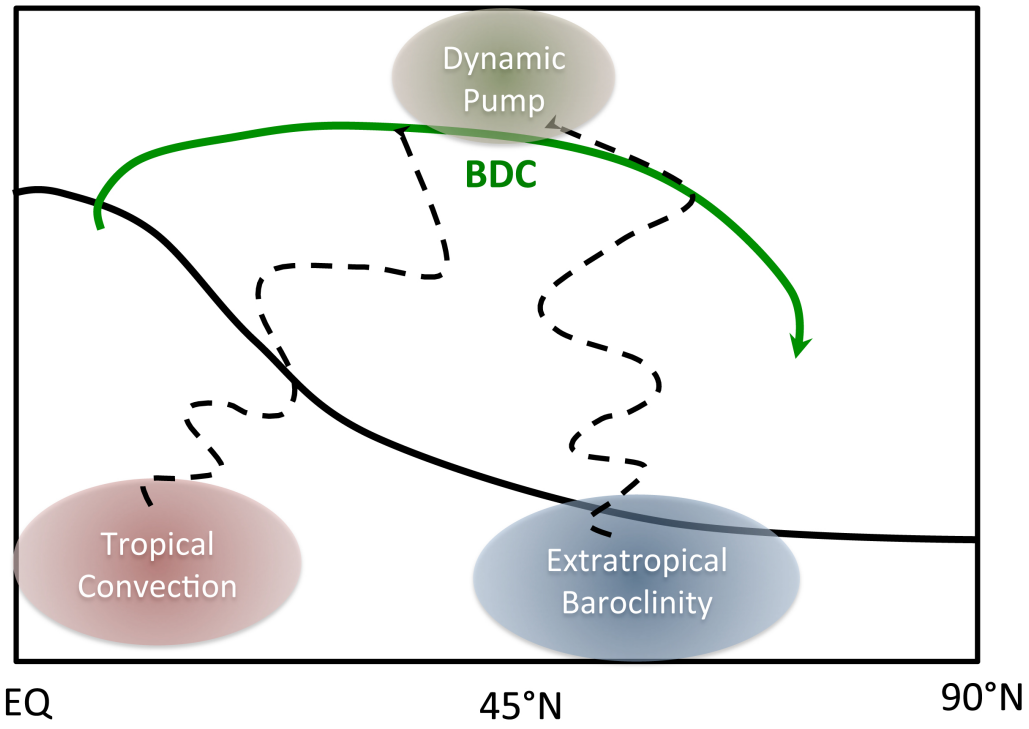

Figure 1.2: Schematic showing the mechansim of downward control in which the eddy perturbations, that are originated in the troposphere and are further propagated into the stratosphere (denoted by the green-shaded 'dynamic pump'), are of significant importance to drive the stratospheric residual circulation.

that bring blizzards and long-lasting cold winters in North America, Europe and Eastern Asia.

In addition, the tropospheric chemistry is coupled with that in the stratosphere via the air mass and chemical exhange between the two layers. Transport of water vapor and methane from the troposphere to the stratosphere feeds important precursors for stratospheric ozone production. Not to mention the notorious chlorofluorocarbon, mostly generated from the anthropogenic acitivities in the lower troposphere, that have caused the informed stratospheric ozone hole in the late 20th century (Crutzen and Oppenheimer, 2008) In the mean-

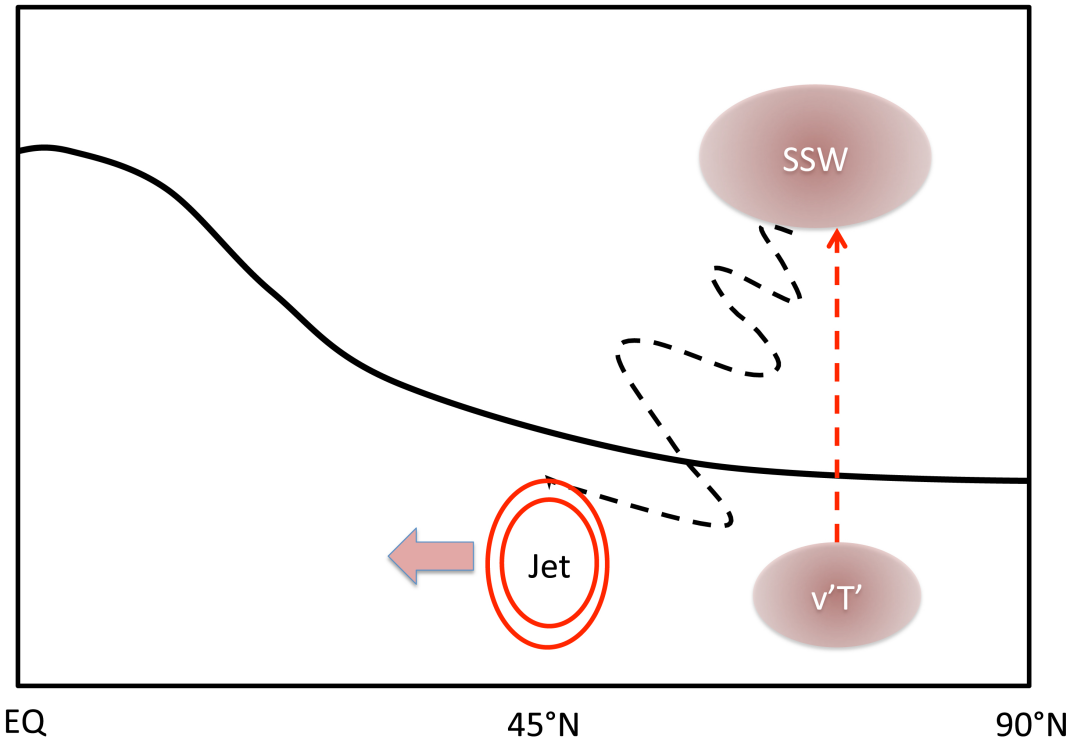

Figure 1.3: Schematic showing the evolution of a sudden stratospheric warming (SSW). With a tropospheric heat flux perturbation, stratospheric polar vortex tend to be weaken by the anomalous upward propagating eddies (dashed arrow) and results in the SSW. Further, SSW impacts the Northern Annular Mode (NAM) by weakening the tropospheric jet and by shifting the jet equatorward.

time, transport of ozone from the stratosphere to troposphere can be crucial to the tropospheric chemistry by enhancing the tropospheric oxidative capacity (Kentarchos and Roelofs, 2003). A deep intrusion of stratospheric ozone into the Earth's surface may further cause air quality concerns (Lin et al., 2012). More importantly, the influences induced by chemical exchange across the tropopause are not contrained in the chemical aspect. For instance, enhanced stratosphere-troposphere exchange (STE) of ozone can reduce the stratospheric column of ozone, and thus cause higher amount of ultraviolet (UV) radiation reaching the surface (Hegglin and Shepherd, 2009). These adjustment in the atmospheric ra-

diation budget can further affect the thermal structure in both the troposphere and the stratosphere, and feedback onto the chemistry via modifying the thermally sensitive reaction rate.

In all, the stratosphere and the troposphere are essentially affecting each other via complicated dynamic coupling and chemical transport. Their interaction certainly complicates the climate system, which requires a more sophiscated understanding.

1.3 Motivation and Outline

The troposphere and stratsophere are both important componnents in the climate system, and their complex feedbacks, noted in Section 1.2, can be essential to understand the status-quo of our climate, as well as to make future climate projection. This triggers us to study this general topic on the stratosphere-troposphere dynamic coupling and chemical transport.

In terms of the tropospheric impacts on the stratosphere via dynamic coupling, many studies (e.g. Garny et al., 2011, Calvo et al., 2010) have suggested that the change of stratospheric circulation within recent decades can be largely driven by the tropical sea surface temperature (SST) perturbation, orignated from either the global warming or the interannual varibility of ENSO or etc. A few idealized simulations by Chen et al. (2010) further show that a zonally-symmetric SST forcing leads to an acceleration of BDC. Therefore, it is natural to raise the question that what if the SST perturbation is zonally asymmetric, as the surface heating in nature is inherently zonally asymmetric due to the land-sea contrast and many other important factors. On the other hand, composites

of climate models (Waugh, 2009) have consistently indicate a strengthening of BDC in both its shallow branch and deep branch, while observations, by quantifying the mean Age of Air (AOA, see details in Section 2.2.2) and the transit time of BDC, suggest the acceleration of BDC is only significant in the shallow branch in the last decade (Bönisch et al., 2011). This structural change of BDC further intrigues us to implement the first projection in this thesis (see Chapter 2) to examine whether the zonal asymmetry of tropical SST forcing can play an important role in it.

As to the stratospheric impact on the troposphere via dynamic couplling, It is well known that the accuracy of traditional weather forecast in the troposphere is limited within 1-2 weeks due to the dominant non-linear effect. However, Baldwin and Dunkerton (2001) propose that, the stratospheric harbinger (e.g. SSW), which can persistently remains the anomalous pattern in months and exert a downward influence on the tropospheric circulation afterwards, may provide as a powerful idenfier to extend our weather prediction. Plus, Polvani et al. (2011) demonstrated that the ozone depletion is the dominant factor influencing the Southern Hemisphere (SH) stratospheric perturbation, as well as subsequent tropospheric changes, in the second half of last century. For the downward dynamic influence from the stratosphere to the troposphere, there are at least three mechanisms potentially at play, with complicated interplay among radiation, mean flow and wave drags. It is important to know which mechanism is more dominant, or, at which ocassion, the mechanism becomes dominant. This motivates to excute the second project in this thesis (see Chapter 3) to examine the dominant mechanism for downward influence of the polar stratospheric ozone depletion-like cooling.

Last, in terms of chemical transport between the two layers, there is more evidence showing that the downward influence from stratospehric ozone transport into the troposphere is highly sensitive to the location of transport (i.e. where stratospheric ozone enters the troposphere). Cross-tropopause transport of ozone at lower latitudes normally limits its influence merely in the upper troposphere via increasing the tropospheric oxidative capacity, while cross-tropopause transport of ozone at higher latitudes can extend further to affect the surface air quality. Hence, it is substantial to quantify the spatial distribution of ozone exchange at the tropopause such that it can distinguish potential different climate impacts in the troposphere. Moreover, it is also of significant importance to find out what physical processes are driving the stratosphere-troposphere exchange (STE) of ozone, and which one is dominant. All these interesting ideas drive us to perform the third project by developing a new STE diagnostic that can identify the location of exchange and discuss the beneath mechanisms.

The general goal of this thesis is to elucidate the complex interplay between the troposphere and stratosphere by advancing our knowlege on some facets of the processes involving with their dynamic coupling and chemical transport. In Chapter 2, the dynamic impacts from the troposphere to the stratosphere is investigated by focusing on the role of tropical sea surface temperature (SST) anomalies. This work is summarized as Yang et al. (2014). Chapter 2 then explores the dynamic impacts from the stratosphere to the troposphere by examining the mechanisms of downward influence of polar stratospheric ozone depletion on the tropospheric circulation. Details about this project refer to Yang et al. (2015). The chemical transport between the stratosphere and the troposphere is studied in Chapter 4 by diagnosing the stratosphere-troposphere exchange (STE) of ozone. A brief summary on all three components of this thesis

is given in Chapter 5. The copyright of the context in Chapter 2 and Chapter 3 have been transferred to the American Meteorological Society (AMS).

CHAPTER 2

TROPOSPHERIC IMPACTS ON THE STRATOSPHERE: THE ROLE OF TROPICAL SST

2.1 Introduction

The Brewer-Dobson Circulation (BDC, Brewer 1949, Dobson 1956) is important for the dynamics and distribution of chemical constituents in the stratosphere, and consequently impacts stratospheric chemistry and climate. In the lower stratosphere, the upwelling across the tropical tropopause acts as a primary path for troposphere-to-stratosphere mass transport, and the isentropic mixing across the subtropical and extratropical tropopause provides a two-way exchange of air masses through blocking anticyclones, cut-off cyclones or tropopause folds (e.g. Holton et al., 1995).

It is well known that tropical Sea Surface Temperature (SST) can impact the lower stratospheric transport. The latent heat released from deep convection can induce an upwelling across the tropical tropopause layer (TTL) by local wave drag (Norton, 2006, Ryu and Lee, 2010), and this has been used to explain the seasonal cycle of the tropical upwelling (Kerr-Munslow and Norton, 2006, Deckert and Dameris, 2008). During the warm phase of the El Niño - Southern Oscillation (ENSO) cycle, the isentropic mixing near the tropopause is found to be weaker than normal (Scott and Cammas, 2002, Scott et al., 2003), but the mean residual meridional circulation is intensified in the lower tropical troposphere (Calvo et al., 2010, Simpson et al., 2011), with a negative correlation between tropical Pacific SSTs and temperature in the tropical lower stratosphere (Hardiman et al., 2007, Calvo et al., 2010). Furthermore, under greenhouse gas

warming, chemistry-climate models (CCMs) predict a consistent acceleration of the residual circulation in the tropical lower stratosphere and a reduction in the age of stratospheric air (e.g. Li et al., 2008, Garcia and Randel, 2008, McLandress and Shepherd, 2009, Butchart et al., 2010, Garny et al., 2011), accompanied with more stratosphere-to-troposphere ozone transport in the extratropics (e.g. Hegglin and Shepherd, 2009). The increase in tropical upwelling is consistent with radiosonde observations with a cooling trend of tropical tropopause temperature (Thompson and Solomon, 2005) and this effect of greenhouse gas warming has been primarily attributed to tropical SST heating (Garny et al., 2011). However, it is difficult to detect this trend in the age of stratospheric air from balloon-borne measurements of stratospheric trace gases (Engel et al., 2008), since the mean age trends estimated from the observations can have large uncertainties due to sparse spatial sampling (Ray et al., 2010, Garcia et al., 2011). It is then important to understand how the SST variability impacts different diagnostics of stratospheric transport circulations.

The mean isentropic circulation, often approximated by the Transformed Eulerian Mean (TEM) residual circulation (Andrews et al., 1987), generally rises in the deep tropics and descends at middle and high latitudes. The strength of the tropical upwelling can be derived from either resolved or parameterized wave drag through the well-known downward control mechanism (Haynes et al., 1991, Holton et al., 1995), which provides a framework to attribute the tropical upwelling to individual wave forcings. The increased tropical upwelling during El Niño has been linked to Northern Hemisphere (NH) planetary waves (Garcia-Herrera et al., 2006), orographic gravity wave drag in the NH (Calvo et al., 2010), or the transient synoptic-scale wave drag in the Southern Hemisphere (SH) (Simpson et al., 2011). The acceleration of the BDC under climate

change has been attributed to the individual contributions from the resolved planetary-scale waves, synoptic-scale waves or parameterized gravity waves, and different forcing mechanisms are found to be equally important for the trend in the BDC (McLandress and Shepherd, 2009). More specifically, the increased planetary wave drag has been explained as a consequence of changes in the propagation characteristics in the stratosphere (e.g. Rind et al., 1998, Olsen et al., 2007), increased wave generation in the lower troposphere (Eichelberger and Hartmann, 2005), or increased wave flux from the troposphere into the stratosphere (Garcia and Randel, 2008, McLandress and Shepherd, 2009). Recently, Shepherd and McLandress (2011) argued that these changes in resolved wave drag can be explained by a critical layer control of the subtropical wave breaking, which in turn can be attributed to the strengthened upper flank of the subtropical jet associated with robust tropical warming and stratospheric cooling.

Another important, albeit less studied, ingredient of the BDC is isentropic mixing. For long-lived constituents in the stratosphere, their equilibrium distributions are controlled by a balance between a slow overturning circulation and rapid mixing along isentropic surfaces (e.g. Holton, 1986, Mahlman et al., 1986). Plumb (2002) showed with a scale analysis that the isentropic stirring dominates the tracer budget within the surf zone over the mean isentropic transport. Using the concept of effective diffusivity (Nakamura, 1996), it is found that isentropic mixing is characterized by enhanced mixing within the surf zone and mixing barriers in the subtropics and at the polar vortex edge (Haynes and Shuckburgh, 2000a,b, Allen and Nakamura, 2001), and that the locations of enhanced (weakened) isentropic mixing coincide with the regions of weak (strong) zonal winds. Furthermore, Shuckburgh et al. (2009) showed that ENSO modulates the Lya-

punov diffusivity across the subtropical jet in agreement with the results in Scott et al. (2003) with effective diffusivity.

In this study, we will investigate the connection between the tropical SST variability and the BDC. Given the uncertainties of the tropical circulation to model physical parameterizations, we employ an idealized aqua-planet model with simple SST profiles. While the simplicity of the model does not allow for a direct comparison to observations (as discussed in Section 2.22.2.3, the idealized model does not include stationary planetary waves in the control run), it allows for a systematic investigation of the mechanisms that link tropical SST variability and transport changes in the lower stratosphere.

It is noteworthy that while El Niño and global warming are both characterized by warming in the tropical upper troposphere, the latitudinal changes in the jet streams are opposite in sign (e.g. Lu et al., 2008, Chen et al., 2008, 2010), which may result in different characteristics in tropospheric wave generation and propagation. We vary both the zonal distribution and the meridional width of the SST perturbations. We found that the key to the response in the stratospheric transport is the zonal distribution of the SST heating: a longitudinally localized heating drives a shallow acceleration of the BDC, but a zonally symmetric heating intensifies the BDC up to a higher altitude associated with an upward-shifted subtropical jet. The different responses can be attributed to the combined effects of tropical heating on the lower stratospheric zonal wind versus the convection-induced planetary waves.

The model and methods applied in this study are briefly described in Section 2.2. In Section 2.3, we will compare the BDC responses to longitudinally localized versus zonally symmetric tropical heating and the responses to meridion-

ally narrow versus broad tropical heating, with a highlight on the changes in the residual circulation, isentropic mixing, and AOA. Section 2.4 further examines the sensitivities of the lower-stratospheric transport to the zonal asymmetry of tropical SST heating. Section 2.5 explores the mechanisms behind the changes in the residual circulation and isentropic mixing. A summary and discussion are given in Section 2.6.

2.2 Aqua-planet model and transport diagnostics

2.2.1 The aqua-planet model and experiment setup

We use the aqua-planet version of the Geophysical Fluid Dynamics Laboratory (GFDL) atmospheric model, AM2.1 (Delworth et al., 2006), but with increased stratospheric resolution. The model is run at a horizontal resolution of approximately 2.5° (longitude) by 2° (latitude), and the standard 24 vertical levels of AM2.1 are increased to 48 levels with the top close to 0.01 hPa, following the vertical levels of AM3 (Donner et al., 2011). There is no subgrid parameterization for orographic or convective gravity waves. At the top of the model, the linear drag at the top layer in AM2.1 has been replaced by a simple sponge layer described in Polvani and Kushner (2002), with a linear damping increasing gradually from 0.5 hPa to the model top.

The model physics package follows the specifications in the Aqua-Planet Experiment (APE) project described in Neale and Hoskins (2000). The solar radiative forcing is fixed in the equinoctial condition but the diurnal cycle is included. The ozone mixing ratio is prescribed as the annual mean climatology

used in the Atmospheric Model Intercomparison Project (AMIP) II. Other radiatively active gases such as CO_2 are well mixed and their mixing ratios adopt the AMIP II recommendations and there are no radiatively active aerosols. There is no topography at the surface, and an idealized SST profile is specified with no sea ice. In the control simulation, the SST is specified as the Qobs profile described in Neale and Hoskins (2000):

$$T_{ctrl} = 27 \times \left(\frac{1}{2} \sin^2 \phi' + \sin^4 \phi' \right), \tag{2.1}$$

where $\phi' = \max\left(\min\left(\frac{3}{2}\phi, \frac{\pi}{2}\right), -\frac{\pi}{2}\right)$ and ϕ denotes latitude. The SST profile can be thought of as the annual and zonal mean SST in the observations (contours in Figure 2.1). In this simple setting, there are no stationary waves in the model but transient planetary waves exist.

We investigate the impact of tropical SST perturbations on the BDC. The control SST profile, Eq.(2.1), is perturbed by

$$T_{anmly} = A_0 \times \exp\left[-\left(\frac{\lambda - \lambda_0}{\lambda_S} \right)^2 - \left(\frac{\phi - \phi_0}{\phi_S} \right)^2 \right], \tag{2.2}$$

where the SST anomaly has a peak of amplitude $A_0 = 3$K centered at the longitude $\lambda_0 = 180°$ and the equator $\phi_0 = 0°$. Our primary focus are the parameters for the meridional width of the tropical SST perturbation ϕ_S and its zonal asymmetry given by λ_S. We start by comparing the circulation responses to the four SST anomalies illustrated in Figure 2.1 with varied zonal asymmetry and meridional width.

- **LATnLONn heating:** latitudinally narrow with $\phi_S = 15°$, longitudinally narrow with $\lambda_S = 30°$

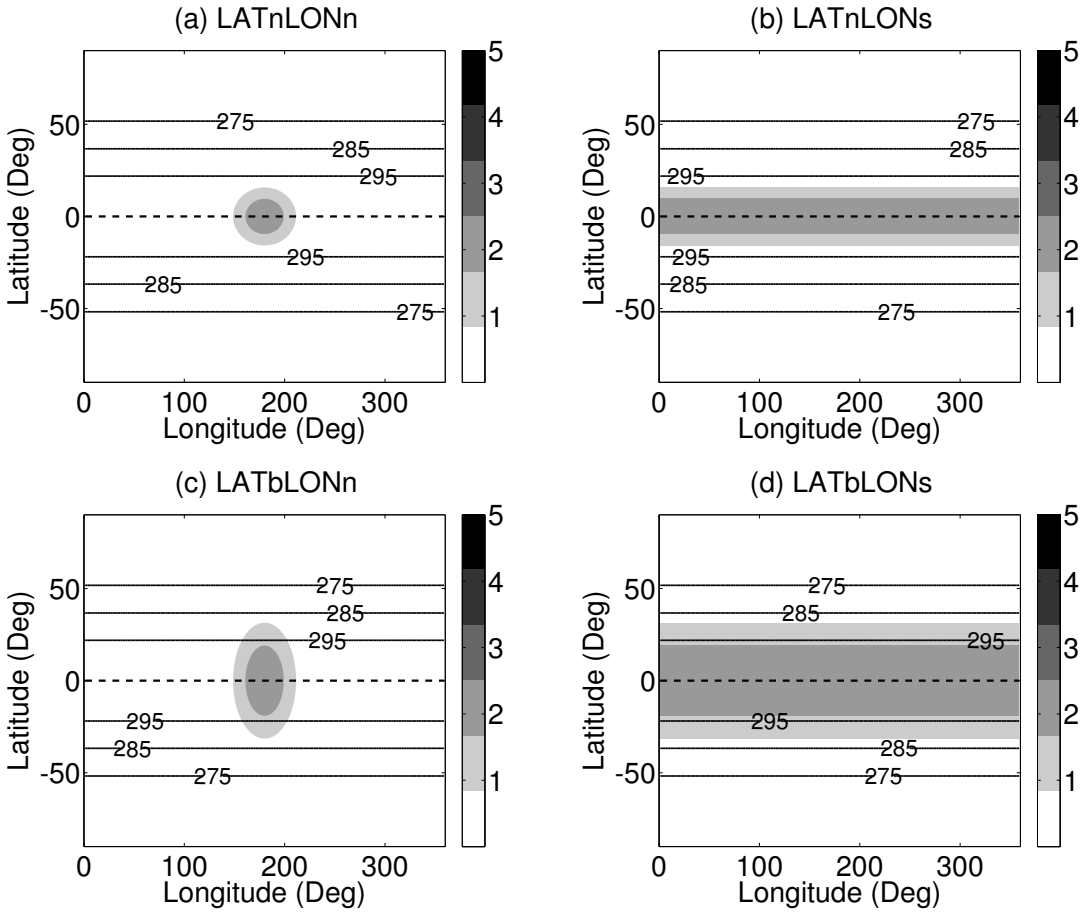

Figure 2.1: Prescribed SST forcing (units: K): the control run is shown as the solid contours and the SST perturbations are depicted by the shading. (a) Latitudinally narrow and longitudinally narrow (LATnLONn) heating ($\phi_S = 15°, \lambda_S = 30°$); (b) latitudinally narrow and longitudinally symmetric (LATnLONs) heating ($\phi_S = 15°, \lambda_S = \infty$); (c) latitudinally broad and longitudinally narrow (LATbLONn) heating ($\phi_S = 30°, \lambda_S = 30°$); (d) latitudinally broad and longitudinally symmetric (LATbLONs) heating ($\phi_S = 30°, \lambda_S = \infty$). The equator is marked by the dashed line.

- **LATnLONs heating:** latitudinally narrow with $\phi_S = 15°$, longitudinally symmetric with $\lambda_S = \infty$
- **LATbLONn heating:** latitudinally broad with $\phi_S = 30°$, longitudinally narrow with $\lambda_S = 30°$
- **LATbLONs heating:** latitudinally broad with $\phi_S = 30°$, longitudinally symmetric with $\lambda_S = \infty$

It will be demonstrated that the zonal distribution of tropical heating has a stronger effect on the lower stratospheric transport although the meridional width of the heating has a stronger effect on the tropospheric jet latitude. In order to further illustrate the effect of the zonal SST distribution, the longitudinal extent of the SST perturbation λ_S is varied using values of $15°, 30°, 60°, 90°, 150°$ and ∞. The monotonic increase of λ_S allows for a change in the longitudinal extent of the SST perturbation from a longitudinally narrow heating ($\lambda_S = 15°$) to a zonally symmetric setup ($\lambda_S = \infty$). Additionally, we have also varied the latitude of maximum heating, ϕ_0 and the amplitude of SST heating, A_0. The results are qualitatively similar and are reported briefly in Section 2.4.1. All integrations are run for 14 years, with the first-year spin-up data discarded. As we are mostly interested in dynamically consistent patterns, we choose to focus on the dominant features of the circulation response. Our results can be reproduced by half of the time series, confirming the statistical significance of our results. The data are sampled instantaneously at a frequency of four times daily for the diagnostics of eddy fluxes and isentropic mixing.

2.2.2 Diagnostic methods

Transport and mixing in the stratosphere are diagnosed using three metrics: 1) the residual mean meridional circulation that approximates the mean diabatic circulation, 2) the equivalent lengths of Potential Vorticity (PV) contours that describe the isentropic eddy mixing, and 3) the mean AOA in the stratosphere.

Residual meridional mean circulation

In the limit of quasi-geostrophic scaling, the mean diabatic circulation in the stratosphere can be approximated by the Transformed Eulerian Mean (TEM) circulation in geometric coordinates (Edmon Jr et al., 1980, Andrews et al., 1987). More specifically, the residual vertical velocity can be written as

$$\bar{w}^* = \bar{w} - \frac{1}{\rho_0 g a \cos\phi} \frac{\partial}{\partial \phi} \left(\cos\phi \frac{\overline{v'\theta'}}{\bar{\theta}_p} \right) \tag{2.3}$$

Here ϕ, p, g, a, ρ_0, and θ denote latitude, pressure, gravitational acceleration, radius of the Earth, zonal mean density, and potential temperature, respectively. $\bar{w}$ is the conventional Eulerian mean (zonal mean) vertical velocity and $\overline{v'\theta'}$ represents the eddy heat flux.

The residual circulation can be diagnosed from the resolved or parameterized wave drag through the 'downward control' principle in the TEM equations (Haynes et al., 1991). From the momentum balance, the residual vertical velocity averaged between the latitudes ϕ_1 and ϕ_2 can be calculated from the integral of the resolved wave drag **DF** above the layer of interest.

$$\langle \bar{w}_m^* \rangle (p) = \frac{1}{\rho_0 (p)\, g \int_{\phi_1}^{\phi_2} a \cos\phi \, \mathrm{d}\phi} \left\{ -\cos\phi \int_0^p \frac{\left[\mathbf{DF}(\phi, p') - \bar{X} \right]}{\hat{f}(\phi, p')} \mathrm{d}p' \right\}_{\phi_1}^{\phi_2} \tag{2.4}$$

where $\langle\ \rangle$ denotes the latitudinal average, and $\bar{X}$ denotes the parameterized wave drag in the model. The modified Coriolis parameter is given by $\hat{f} = f - (1/a\cos\phi)(\partial/\partial\phi)(\bar{u}\cos\phi)$. The curly bracket $\{\ \}$ denotes a subtraction of the quantity inside the bracket at the latitude ϕ_2 by its value at the latitude ϕ_1. We set $\phi_1 = -15^\circ$ and $\phi_2 = 15^\circ$ over the deep tropics following Randel et al. (2008). This latitudinal average avoids the singularity of the Coriolis parameter near the equator and facilitates the calculation of the averaged vertical velocity from the meridional mass flux across the northern and southern boundaries. The resolved wave drag **DF** is given by the Eliassen-Palm (EP) flux divergence:

$$\mathbf{DF} = \frac{1}{a\cos\phi} \nabla \bullet \mathbf{F} = \frac{1}{a\cos\phi} \left[\frac{1}{a\cos\phi} \frac{\partial \left(F_\phi \cos\phi \right)}{\partial \phi} + \frac{\partial F_p}{\partial p} \right] \tag{2.5}$$

where **F** is the EP flux vector with components

$$F_\phi = a\cos\phi \left[-\overline{v'u'} + \left(\frac{\partial \bar{u}}{\partial p} \right) \frac{\overline{v'\theta'}}{\bar{\theta}_p} \right] \tag{2.6a}$$

$$F_p = a\cos\phi \left[\hat{f} \frac{\overline{v'\theta'}}{\bar{\theta}_p} + \rho_0 g \overline{w'u'} \right]. \tag{2.6b}$$

Furthermore, the residual vertical velocity can also be diagnosed from the thermodynamic balance with the diabatic heating $\bar{Q}$:

$$\bar{w}_Q^* = -\frac{1}{\rho_0 g} \frac{\bar{Q}(\theta, p)}{\bar{\theta}_p} \tag{2.7}$$

The comparison between $\bar{w}^*$ and $\bar{w}^*_m$ determines to what extent the tropical upwelling is wave-driven, and the consistency between $\bar{w}^*$ and $\bar{w}^*_Q$ indicates the adjustment in diabatic heating approximately balances the wave-driven circulation.

Isentropic mixing

Tracers in the stratosphere are subject to rapid eddy mixing along isentropic surfaces. For a passive tracer that varies monotonically with latitude, we can characterize the isentropic mixing by the 'equivalent length' of tracer contours (Nakamura, 1996, Haynes and Shuckburgh, 2000a, Allen and Nakamura, 2001), given by

$$L_e^2 = \frac{\partial}{\partial A} \iint\limits_{A(q,t)} |\nabla q|^2 \, dA \Big/ \left(\frac{\partial q}{\partial A} \right)^2 \tag{2.8}$$

where q is the mixing ratio of a passive tracer, and A is the area bounded by the tracer contour q around the North Pole. The area A is defined by an equivalent latitude ϕ_e by $A = 2\pi a^2(1 - \sin\phi_e)$. In regions of strong mixing along isentropic surfaces, the tracer contours are expected to be long and complex in geometry. The equivalent length is greater than or equal to the actual length of tracer contours (Haynes and Shuckburgh, 2000a). If the tracer contour exactly follows a latitude circle, its equivalent length shrinks to its minimum value, i.e. the length $2\pi a \cos\phi_e$ of that latitude circle for a given latitude ϕ_e. Thus, the equivalent length ratio $\tilde{\kappa}_{eff} = L_e^2 \,/\, (2\pi a \cos\phi_e)^2$ provides a non-dimensional measure of the strength of isentropic eddy mixing. If the diffusion coefficient (κ in Eq. 3 of Haynes and Shuckburgh, 2000a) is a constant, $\tilde{\kappa}_{eff}$ is proportional to the effec-

tive diffusivity in isentropic mixing that is defined by the mass flux across the tracer contours (Nakamura, 1996). More generally, if the exact form of small-scale diffusion is not known, the equivalent length can still describe the degree of eddy mixing as the effective diffusivity is dictated by the large-scale stirring and stretching (Allen and Nakamura, 2001).

The tracer in the equivalent length calculation can either be a dynamical tracer such as Ertel's PV or a long-lived chemical tracer in the stratosphere like SF_6. Haynes and Shuckburgh (2000a) also calculated the equivalent length of a passive tracer advected by the isentropic winds, which is consistent with the mixing length of the PV. In this study, we will calculate the equivalent length using Ertel's PV, $q = -g\zeta_a \frac{\partial \theta}{\partial p}$ where ζ_a is the absolute vorticity on an isentropic surface.

Age of Air

Another diagnostic of stratospheric transport is the mean age of stratospheric air (AOA), the transit time from the tropical tropopause to a location within the stratosphere (e.g. Hall and Plumb, 1994, Waugh and Hall, 2002). In this diagnostic, a clock tracer is specified to grow linearly in time in the source region below 750 hPa, and above this level the tracer is conservative except for small-scale diffusion. For a tracer concentration growing linearly at its source, the mixing ratio of the tracer elsewhere is expected to increase linearly with the same growth rate but reaches a certain magnitude later than at the source (see Figure 1 in Waugh, 2009). This time lag defines the mean AOA, given by

$$\Gamma = t(\chi; \phi, p) - t(\chi; \phi_0, p_0) \tag{2.9}$$

where χ is the mixing ratio of the tracer, and ϕ_0 and p_0 denote the latitude and pressure of the reference point. The mean AOA can be influenced by both mean isentropic circulation and eddy mixing. For the age of stratospheric air, the reference point is generally chosen at the tropical tropopause. We follow Garcia et al. (2011) by calculating the mean AOA using the monthly averaged mixing ratio of the age tracer, and setting the reference point at $\phi_0 = 0,\ p_0 = 150\,\text{hPa}$.

2.2.3 Atmospheric circulation in the control simulation

The control simulation can approximately reproduce the basic features of the observed annual mean atmospheric circulation and transport, also shown in the contours of Figs. 2-5. The dome-shaped tropopause and the tropical 'cold point' aloft are both captured in this simulation (Figure 2.2), as well as the tropospheric subtropical jets and stratospheric jets (Figure 2.3). However, due to the absence of stationary planetary waves in this simulation, the zonal mean zonal winds are stronger in magnitude than those in observations, particularly in the NH stratosphere where stationary planetary waves exert a strong wave drag on the stratospheric winter circulation. We therefore focus on the annual mean responses in this study, rather than the winter season that most other studies concentrate on when exploring the stratosphere-troposphere coupling and transport. Similarly, the transient planetary waves and synoptic scale waves in the model can simulate a reasonable magnitude of the residual circulation in the troposphere and lower stratosphere, whereas the residual circulation in the

middle and upper stratosphere is weaker than the observed circulation due to a lack of stationary planetary waves (Figure 2.4). As a result, the model can simulate a reasonable structure in AOA (Figure 5), although the air the upper stratosphere is older than in observations. In the next section, we will compare these climatological patterns with the SST-forced changes shown in color.

As for isentropic mixing, Figure 2.6 shows the climatological mean isentropic eddy mixing and EP flux divergence in the control run. The equivalent length is calculated on each isentropic surface, and the time mean equivalent length is interpolated linearly to pressure surfaces. As found in observations (Haynes and Shuckburgh, 2000b), the intensity of isentropic eddy mixing is roughly anti-correlated with the strength of the zonal mean zonal wind. Mixing maxima occur in the stratospheric surf zone and at the flanks of the tropospheric jets where the zonal winds are weak. Isentropic mixing is suppressed at the stratospheric jet and subtropical jet with prevailing westerlies, and the weak mixing results in transport barriers that lead to a large latitudinal gradient in mean AOA (not shown here). Furthermore, the regions of strong eddy mixing are also roughly consistent with the regions of large EP flux convergence where wave breaking is frequent. Baroclinic synoptic-scale eddies are generated within the extratropical lower troposphere and are mostly dissipated in the extratropical middle and upper troposphere. Even in the absence of topographical forcing, transient planetary waves can be generated through eddy-eddy interactions (Scinocca and Haynes, 1998). These planetary-scale waves are allowed to propagate vertically into the stratosphere, and the subsequent breaking of stratospheric waves results in rapid mixing of air masses along isentropic surfaces.

Conventionally, research has focused on the winter hemisphere when dis-

cussing stratosphere-troposphere coupling and transport (e.g. Gerber, 2012). Here, our simulations correspond to the annual mean condition for simplicity. Without topography and land-sea contrast, the simulated polar vortex in the stratosphere will be unrealistically strong if the aqua-planet model adopts a solstitial condition. Therefore, the current setting of the control simulation is more suitable for the problem we are investigating. As the result of the simplicity of the aquaplanet model, we will not examine the effects of gravity waves or orographic Rossby waves. However, similarities of the residual circulation response are still found by comparing the results from our idealized simulation (see details in Section 2.3) with the ones in a comprehensive model where these waves are resolved or parameterized (Garny et al., 2011).

2.3 BDC responses to different zonal and latitudinal distributions of tropical SST heating

We begin to investigate the patterns of tropical SST-forced stratospheric transport changes using four types of tropical heating as illustrated in Figure 2.1. Specifically, we compare longitudinally narrow ($\lambda_S = 30^\circ$, denoted by LONn) heating (Fig. 2.1, left column) with longitudinally symmetric ($\lambda_S = \infty$, denoted by LONs) heating (Fig. 2.1, right column). For both LONn and LONs, we also compare latitudinally narrow ($\phi_S = 15^\circ$, denoted by LATn) heating (Fig. 2.1, top row) with latitudinally broad ($\lambda_S = 30^\circ$, denoted by LATb) heating (Fig. 2.1, bottom row). The changes in atmospheric circulation and transport are presented in the same fashion.

Figure 2.2 displays the changes in zonal mean temperature (shading) in each simulation with respect to the climatology of the control run (contours). All tropical heating patterns lead to warming in the tropical upper troposphere, cooling in the tropical lower stratosphere, and warming in the polar stratosphere. This spatial pattern is qualitatively consistent with the temperature response associated with the ENSO cycle (e.g. Randel et al., 2009) and with the tropical SST heating due to greenhouse gases (Garny et al., 2011). The warming over the stratospheric polar caps in the experiments with LONn heating (left column) is larger than that with LONs heating (right column). The tropospheric warming, on the other hand, is pronounced only in the tropical upper troposphere and subtropics for LONn heating, while the warming is spread over the entire tropics for LONs heating.

As for zonal mean zonal wind (Fig. 2.3), for LONn heating (left column) the easterlies in the deep tropics are weakened and even transition to westerlies. With the biggest eastward acceleration at approximately 150 hPa, superrotation develops through equatorial deep convection as found in Liu and Schneider (2011). The tropospheric subtropical jet is decelerated on its equatorward flank, and the jet in the stratosphere is weakened. By contrast, for LONs heating (right column) the tropospheric subtropical jet is shifted upward, and the zonal mean zonal wind is increased on the equatorward flank of the stratospheric jet. With less deceleration about the stratospheric jet for LONs heating, less warming is observed over the stratospheric polar caps as compared to LONn heating. This suggests a smaller wave drag in the (lower) stratosphere given a zonally symmetric heating in the LONs runs. Moreover, for the two LONs experiments, the subtropical jet moves equatorward for the LATn heating but the jet shifts poleward when the meridional width of the heating is increased in LATb. This is

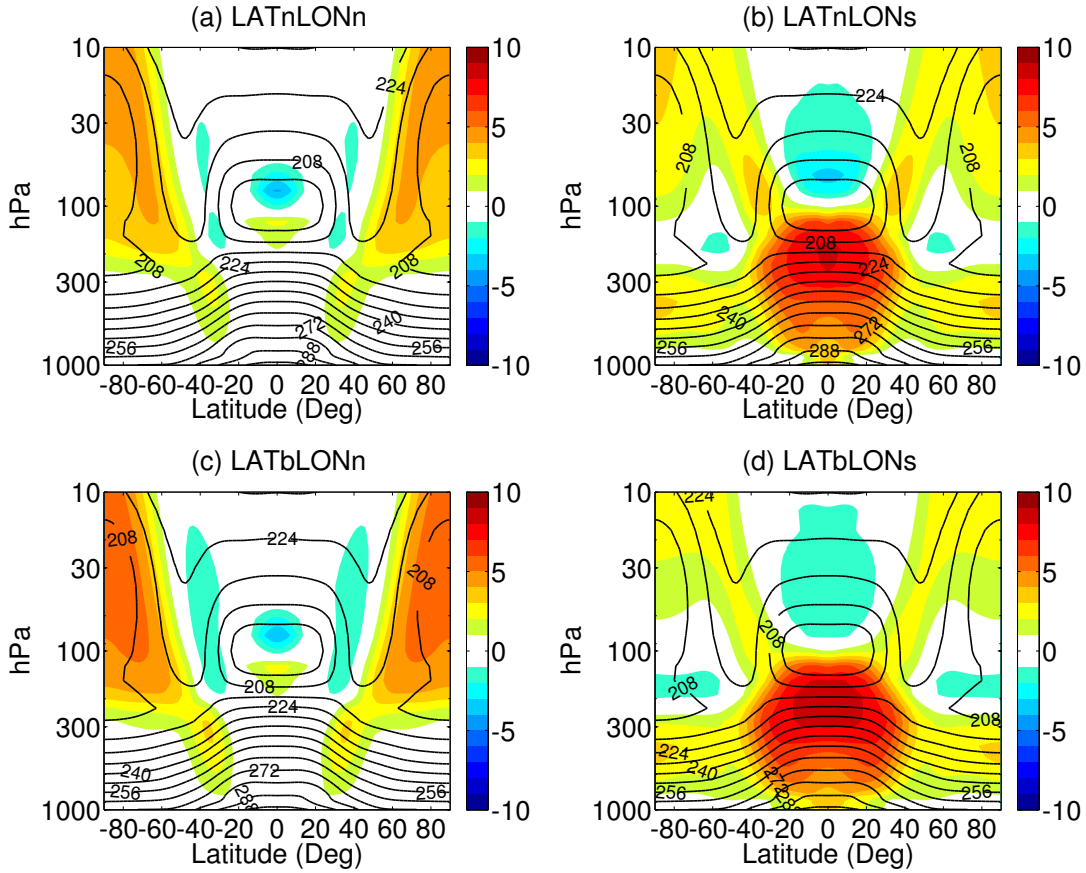

Figure 2.2: Climatology of the control run and the change in zonal mean temperature (shading) (units: K) for (a) LATnLONn; (b) LATnLONs; (c) LATbLONn; and (d) LATbLONs.

consistent with what was found in Lu et al. (2008) and Chen et al. (2010), who argued that the differences between LATn and LATb are analogous to the jet response for El Niño forcing versus global warming.

Changes in zonal wind and temperature are accompanied by changes in stratospheric transport and mixing. The stratospheric mean diabatic circulation, denoted by the residual stream function, is strengthened above 100 hPa in all four experiments (Figure 2.4). However, the spatial pattern of the strengthening depends critically on the zonal distribution of the SST forcing. LONn heating (left column) drives a shallow strengthening of the residual circulation, while

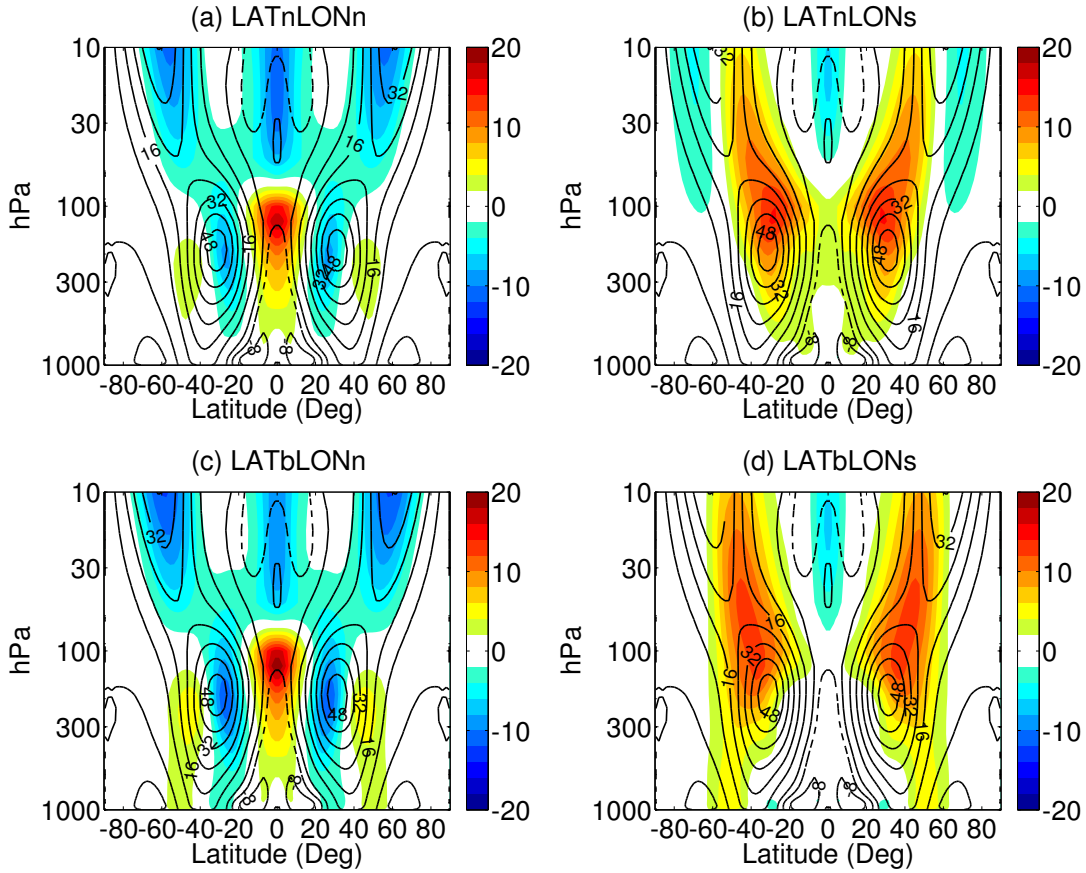

Figure 2.3: As in Figure 2.2, but for the zonal mean zonal wind (units: $\mathrm{m\,sec^{-1}}$, solid contours for positive, dashed contours for negative).

LONs heating (right column) generates a deep acceleration of the BDC. Interestingly, the latitudinal extent of the heating has little effect on the stratospheric circulation response, although it alters the position of the tropospheric subtropical jet (cf. Figure 2.3). The change in the residual circulation is also in agreement with the tropical temperature adjustment noted above, as expected from the thermodynamical balance in Eq. 2.7. In addition, an intensification of the tropical upwelling in the lower stratosphere is accompanied by an upward shift of the tropical tropopause, as well as a decrease in the cold point temperature, which in turn produces the upper-troposphere warming / lower-stratosphere

cooling dipole pattern shown in Figure 2.2. More importantly, while the climatological diabatic circulation exhibits a single hemispherical cell in the stratosphere, the different depths of the residual circulation response suggest distinct dynamical controls of the diabatic circulation. In a different idealized model, Gerber (2012) also found a tropospheric control of the shallow branch of the BDC by surface topographic forcing, and a stratospheric control of the deep branch by the intensity of the polar vortex. Our results suggest that a zonally symmetric SST forcing can also control the deep branch of the BDC through the strength of the subtropical jet and the associated thermal wind aloft, while a zonally localized SST forcing can control the shallow branch by convection-induced planetary waves.

It should be noted that Birner and Bönisch (2011) found the deep branch of the stratospheric residual circulation is generally broader in meridional width than the shallow branch, which seems to be the opposite to our results. In fact, the meridional width of the shallow branch simulated in this study is consistent with the one in Birner and Bönisch (2011) within the latitudinal band equatorward of 70°N/S, and then the difference lies in the deep branch. One important factor that can cause this difference in the deep branch is the strength of the stratospheric polar vortex. As noted in Section 2.22.2.3, the polar vortex is much stronger due to the absence of stationary waves in the control run. Thus, the descending branch of the deep circulation takes place near the edge of the polar vortex, which in turn greatly limits the meridional width of the deep branch (see Fig. 2 in Plumb, 2002). Also, it seems that the anomalous residual circulation cell near 60°N/S in LONn heating runs could be counted as a deep response if smaller values of contours are plotted in Fig. 2.4(a)(c). However, we argue that it should not be regarded as a deep response for the entire BDC, as it seems to

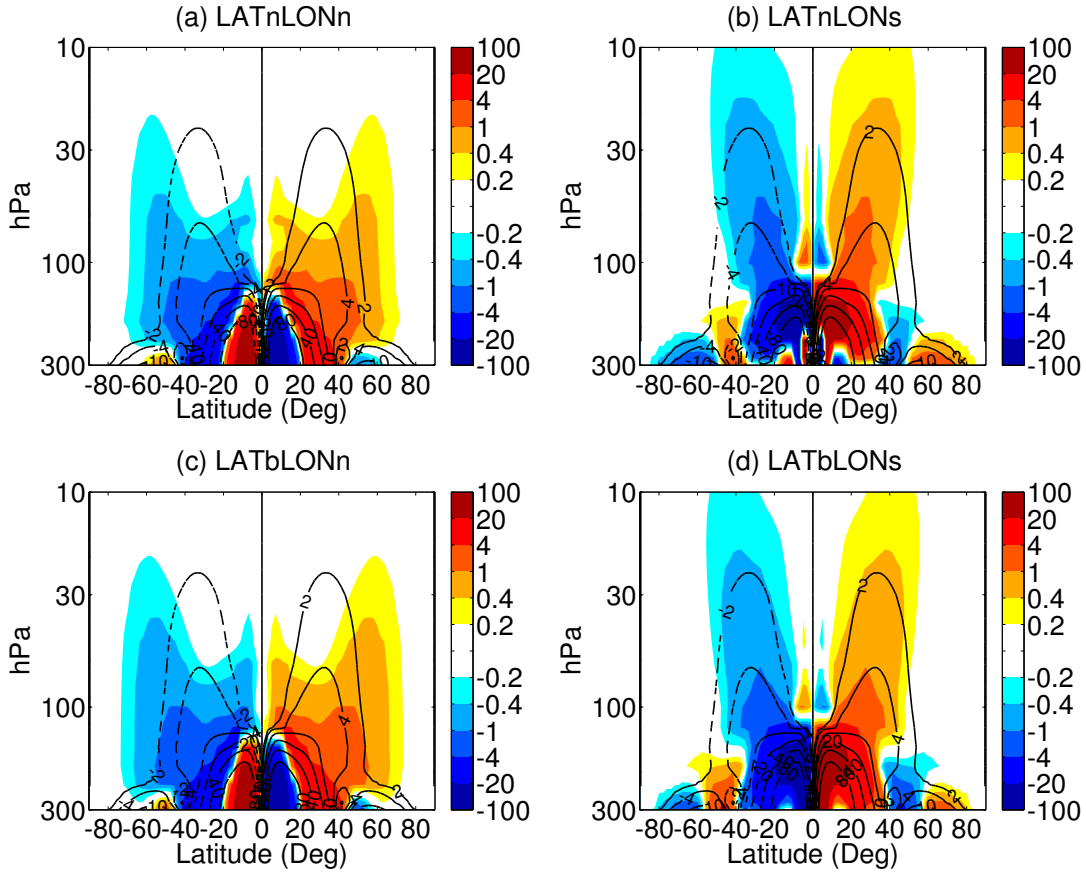

Figure 2.4: Similar to Figure 2.3, but for the residual stream function $\bar{\chi}^*$ (units: 10^9 kg sec^{-1}). Warm shading and solid contours depict anticyclonic circulation whereas cold shading and dashed contours depict cyclonic circulation. Note that the vertical axis has been changed to 10-300 hPa.

be disconnected from the tropical upwelling that determines the hemispheric mass transport in the stratosphere along the deep branch of BDC.

The changes in the residual circulation have important consequences for the mean AOA in the stratosphere (cf. Figure 2.5). Given an acceleration of the lower-stratospheric tropical upwelling in all four experiments, the mean AOA is reduced along the trajectory of the diabatic circulation. Therefore, in spite of the varied depths of the BDC change, the stratospheric air becomes fresher at the

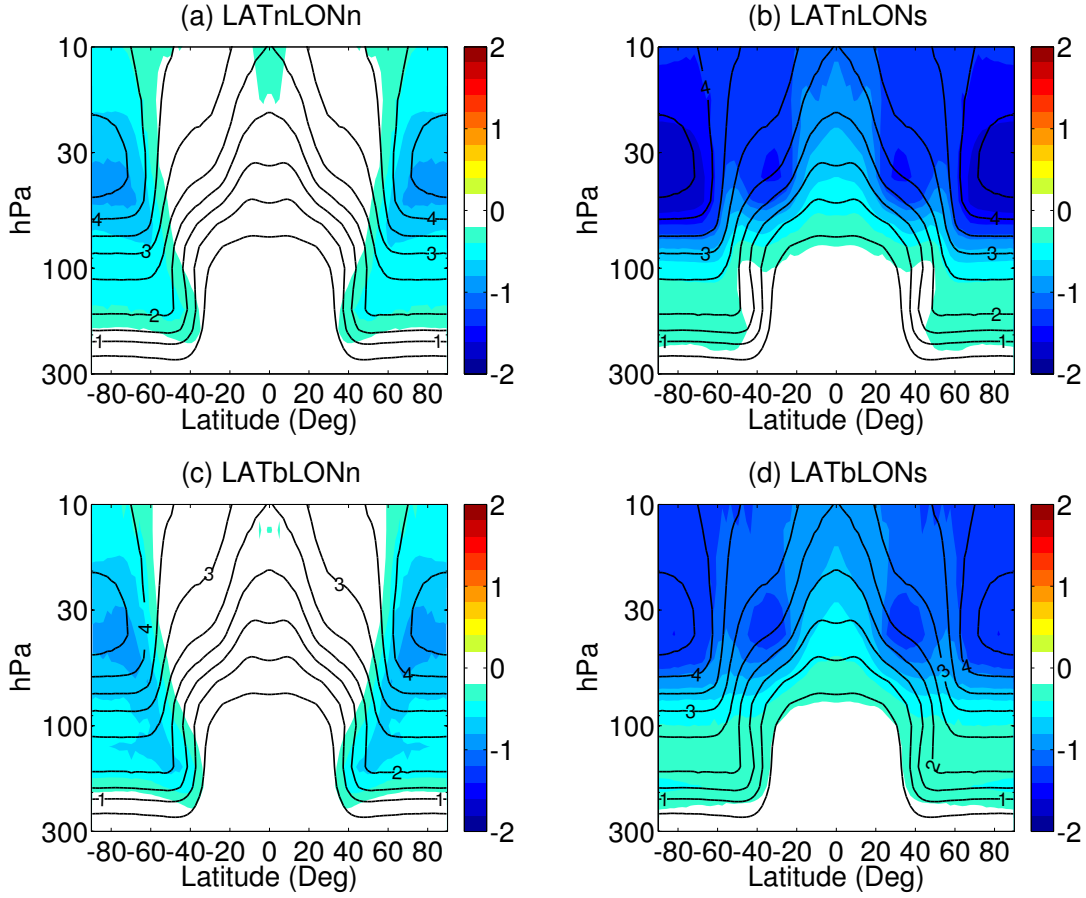

Figure 2.5: As in Figure 2.3, but for the mean AOA (units: years). Note that the vertical axis has been changed to 10-300 hPa.

location of the polar vortex. Furthermore, with a deeper strengthening of the residual circulation for LONs heating, the mean AOA declines dominantly in the tropics and subtropics in addition to the extratropical decrease (cf. Figure 2.5 (b)(d)). This low-latitude freshening of stratospheric air is small in the absolute change or relative change for LONn heating due to the absence of the tropical deep branch response in the BDC (cf. Figure 2.4 (a)(c)). Again, the response of the mean AOA in the stratosphere does not depend on the latitudinal width of the SST heating, consistent with the change in the residual circulation.

Besides the mean diabatic circulation, the isentropic mixing can also be influ-

enced by the tropical SST perturbation. The corresponding changes in isentropic mixing to different tropical SST forcings are shown in Figure 2.7. Similar to the changes in the stratospheric residual circulation and AOA, the changes in isentropic mixing in the upper troposphere / lower stratosphere (UTLS) region are more strongly influenced by the zonal distribution of the tropical heating than by its latitudinal width. The anti-correlation between the changes in isentropic mixing and the zonal mean zonal flow still holds qualitatively. For LONn heating, isentropic mixing is predominantly increased in the regions where westerlies are strongly suppressed including the stratospheric jet and the tropospheric subtropical jet. The decrease in isentropic mixing in the tropical upper troposphere can be attributed to the appearance of equatorial superrotation. On the contrary, for LONs heating, isentropic mixing decreases within the cores of upward-shifted and intensified subtropical jets. These changes in isentropic mixing can impact the mean AOA in the stratosphere. In addition to the Lagrangian trajectory and transit time determined from the residual circulation, isentropic mixing will increase the transit time by moving air parcels horizontally away from their trajectories. Overall, by a comparison of the mean AOA change with the change in the diabatic circulation and isentropic mixing, the change in stratospheric mean AOA seems to be dominated by the change in the residual circulation (as will be discussed in Section 2.4.2).

In summary, the BDC response to longitudinally narrow (LONn) heating differs from its counterpart with longitudinally symmetric (LONs) heating in many aspects. Particularly, LONn heating generates a shallow acceleration of the residual circulation, while LONs heating generates a deep strengthening of the BDC. This difference in the residual circulation change impacts the dynamical response in terms of stratospheric temperature and zonal wind, resulting in

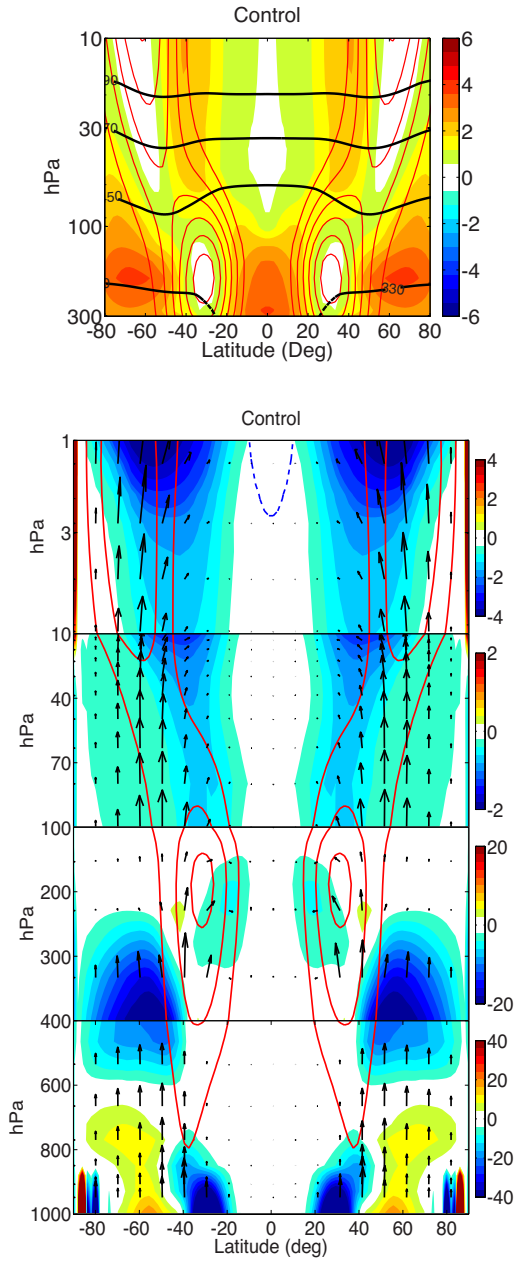

Figure 2.6: Climatology of the control run for (top) the isentropic mixing denoted by the logarithm of equivalent length ratio $\tilde{\kappa}_{eff}$ (shading) and zonal mean zonal wind (colored contours, units: $\mathrm{m\,sec^{-1}}$). Several isentropic surfaces are highlighted as bold black lines to show where the equivalent length ratio data are originally interpolated from; (bottom) EP flux (vectors) and associated divergence **DF** (shading, units: $\mathrm{m\,sec^{-1}day^{-1}}$), and zonal mean zonal wind (red contours: westerly wind, blue contours: easterly wind. Contour interval: $16\,\mathrm{m\,sec^{-1}}$). Warm shading denotes divergence (wave generation) and cold shading denotes convergence (wave dissipation). Note that a change in the vertical axis.

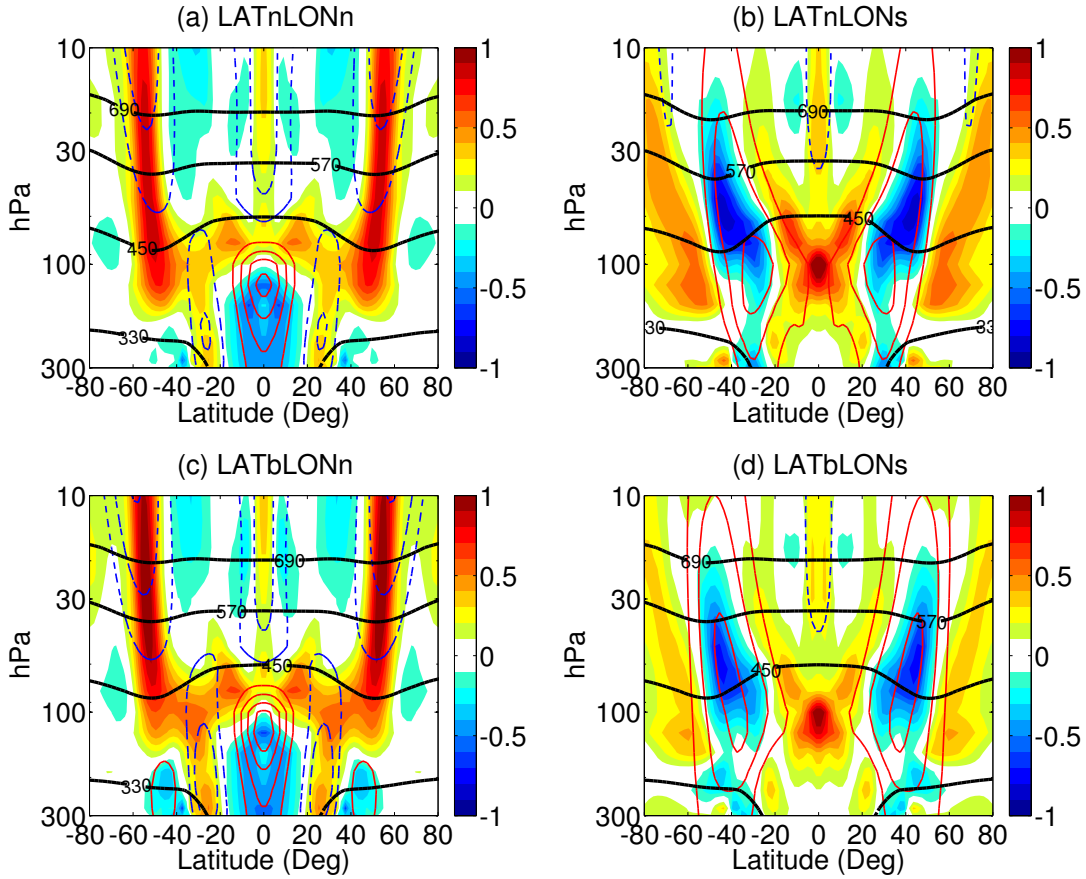

Figure 2.7: As in Figure 2.6 (top), but for the isentropic mixing anomalies. The contour interval is 4 m sec^{-1}.

a much broader reduction of mean AOA in the lower stratosphere in the LONs experiments. The change in isentropic mixing also corresponds to the change in zonal wind. Moreover, by varying the latitudinal extent of the heating, the tropospheric subtropical jet transitions between an equatorward El Niño-like shift and a poleward global warming-like change, but the jet shift in latitude has little impact on the diagnostics of stratospheric transport. Therefore, we will focus on the effect of the zonal distribution of the SST forcing on the BDC in the remainder of this study.

2.4 Sensitivity of the BDC response to tropical SST forcing

2.4.1 Sensitivity study

Here we summarize briefly the robustness of the shallow-to-deep transition in the BDC response to the zonal distribution of the tropical SST forcing. Figure 2.8 displays the change in the stratospheric transport as a function of the zonal distribution of tropical SST heating (LONn corresponds to $\lambda_S = 30^\circ$ and LONs corresponds to $\lambda_S = \infty$) for the latitudinally narrow (LATn) heating experiments. The eddy mixing anomaly is denoted by the equivalent length ratio $\tilde{\kappa}_{eff}$ on isentropic surfaces, and the rough correspondence between isentropic surfaces and pressure surfaces can be seen in Figure 2.6. For all the experiments with $\lambda_S < 90^\circ$, the residual vertical velocity $\bar{w}^*$ at 70 hPa exhibits anomalous upwelling in deep tropics and downwelling over the polar regions. Particularly, the anomalous downwelling occurs within the polar vortex, highlighting an extratropical response. As expected from a thermodynamical balance, temperature anomalies mirror the changes in residual vertical velocity, with cooling corresponding to strengthened upwelling at the equator and warming corresponding to strengthened downwelling at the poles. Moreover, positive anomalies of the equivalent length ratio $\tilde{\kappa}_{eff}$ are found at the 450K isentropic surface over the mid-latitude region. This indicates increased isentropic mixing in the mid-latitude lower stratosphere, consistent with a weakened polar vortex and polar warming. Subject to these changes, the mean AOA is reduced over the polar vortex. All of these characteristics are consistent with the LONn experiments described in Section 2.3.

For all the experiments with $\lambda_S > 90^\circ$, although $\bar{w}^*$ at 70 hPa also exhibits

an anomalous upwelling in the deep tropics, the center of anomalous downwelling moves from the high latitudes to the midlatitudes (Fig. 2.8 (a)), stressing a tropical and subtropical strengthening of the residual circulation as seen in Figure 2.4 (b)(d). Temperature anomalies also show dynamical warming in the midlatitudes mirroring the increased downwelling. Interestingly, the isentropic mixing at the 450K isentrope is strongly suppressed in the surf zone, which can be attributed to the upward shift and intensification of the subtropical jets. Accompanying these circulation changes is a broad decline of the mean AOA in the lower stratosphere extending into the deep tropics. All of these features are consistent with the LONs experiments.

It is noteworthy that the transition in the lower-stratospheric transport takes place abruptly around the value of $\lambda_S = 90^\circ$. Such a clear transition is not observed in the upper troposphere. A number of additional experiments are performed to confirm the robustness of the shallow-to-deep transition by exploring the parameters in the SST perturbation. The same diagnostics are presented in Figure 2.9 for the latitudinally broad (LATb) heating. A likewise transition is observed in the lower-stratospheric residual circulation, temperature, isentropic mixing, and mean AOA with the zonal asymmetry of tropical heating, which are consistent with the changes in the stratospheric polar vortex (not shown). Although the transition is qualitatively similar, the threshold value of the zonal extent ($\lambda_S = 150^\circ$) is larger than that for LATn forcing. Other than that, the increase in tropical upwelling is not monotonic with the longitudinal extent λ_S, but a maximum is observed in the cooling of the deep tropics for $\lambda_S = 60^\circ - 90^\circ$.

Furthermore, as the zonally averaged SST heating is much smaller in the LONn runs as compared to the LONs runs, we have conducted sensitivity ex-

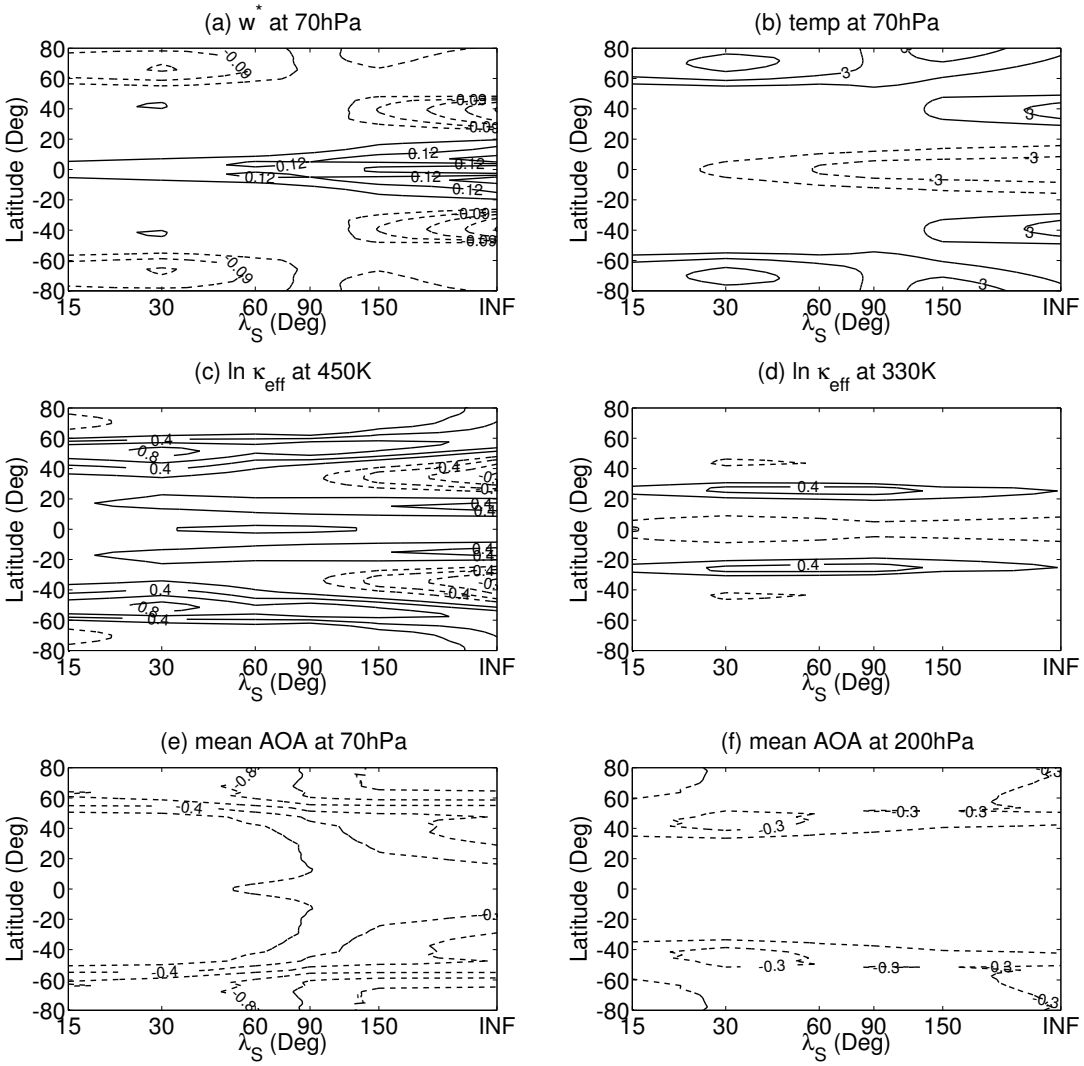

Figure 2.8: Atmospheric changes following the expansion of the longitudinal extent λ_S for the LATn heating: (a) residual vertical velocity w^* at 70 hPa denoting the structural change in the BDC; (b) zonal mean temperature change at 70 hPa; (c)(d) isentropic mixing denoted by the logarithm of the equivalent length ratio $\tilde{\kappa}_{eff}$ on isentropic surfaces of 450K and 330K, respectively, approximately equivalent to 70 hPa and 200 hPa; (e)(f) mean AOA at 70 hPa and 200 hPa, respectively.

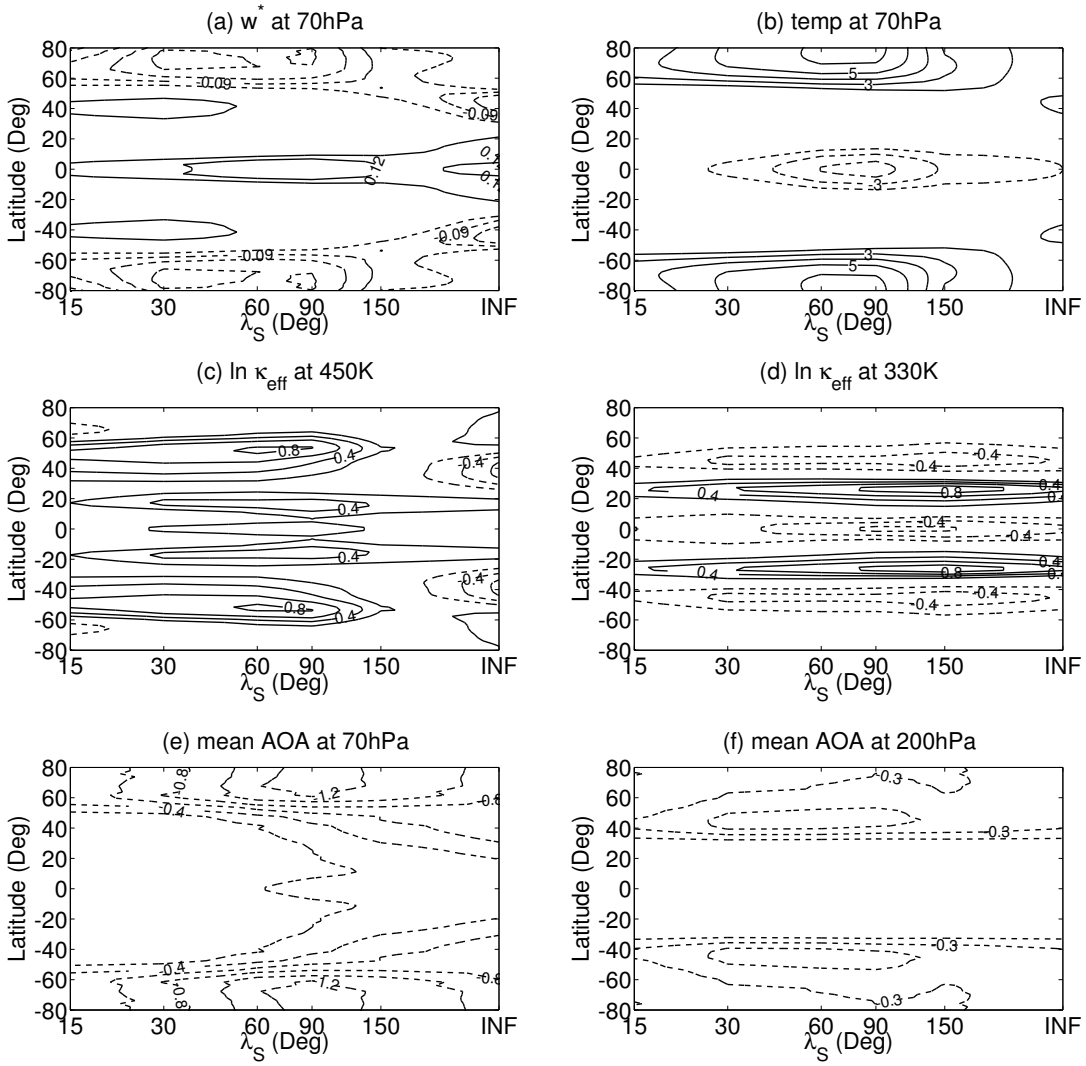

Figure 2.9: As in Figure 2.8, except for the LATb heating.

periments by increasing the SST heating amplitude in the LONn heating A_0 to match the zonal mean SST heating magnitude of the LONs run. Despite a much stronger local SST forcing, the new LONn run yields a qualitatively similar shallow circulation response in residual circulation and associated changes in zonal wind, as well as isentropic mixing (not shown). Finally, we have shifted the latitude of the maximum SST heating, ϕ_0, away from the equator as in Norton (2006). The BDC response is qualitatively similar, while the magnitude of the re-

sponse is gradually reduced as the heating center moves away from the equator (not shown). Overall, our sensitivity study confirms the robustness of the transition from a shallow branch response to a deep response with respect to the distribution of the tropical SST forcing, although the threshold of the transition can be sensitive to the structure or magnitude of the SST forcing.

2.4.2 Linkage between the residual circulation, isentropic mixing, and AOA

Using these sensitivity experiments, we will test the dynamical linkage between the mean residual circulation, isentropic mixing, and the AOA by a simple correlation analysis. In Section 2.3, we found that the stratospheric mean AOA change can be explained qualitatively by the change in the residual circulation. Given the experiments with separate changes in the zonal asymmetry and meridional width of tropical SST heating, we will test the dynamical relationship quantitatively. In particular, to what extent can a change in AOA be explained by the mean circulation versus the eddy mixing? Empirically, we found that the strength of tropical upwelling is well correlated with AOA in most of the stratosphere, and that the eddy mixing has almost no local correlation with AOA except near the subtropical tropopause. Here we present the results for remote and local effects on the mean AOA in two regions: the polar vortex region (averaged between 60°N – 65°N at 70 hPa) and near the subtropical tropopause (averaged between 40°N – 45°N at 200 hPa).

Figure 2.10 compares the mean AOA changes in the two regions with the changes in tropical upwelling (i.e., w^* averaged between 15°S-15°N at 70 hPa)

and local eddy mixing (i.e., the equivalent length of PV). For the AOA near the polar vortex (top row), the AOA is well correlated with the strength of tropical upwelling (R^2=0.64), but it displays almost no correlation with the strength of local eddy mixing. The experiment with larger tropical upwelling also corresponds to fresher air near the polar vortex, as expected from the transport by the overturning circulation from the tropics to the poles. This relationship holds for both LATn and LATb. This suggests statistically that when the tropical SSTs are perturbed, the strength of tropical upwelling has a dominant control on the polar AOA in the lower stratosphere over the effect of local mixing.

As for the mean AOA near the subtropical tropopause, the AOA exhibits almost no correlation with the strength of tropical upwelling in this case (Figure 2.10 (c)), but it is well correlated with the strength of eddy mixing on the equatorward flank of the subtropical jet, yielding R^2=0.52 (Figure 2.10 (d)). The experiment with larger isentropic mixing near the subtropical tropopause corresponds to fresher air locally. This can be explained by a rapid exchange of air masses near the tropopause associated with Rossby wave breaking, and the resulting freshening of air is more efficient in ventilating the air near the tropopause than the mean overturning circulation in the lower stratosphere.

2.5 Mechanisms of the residual circulation and isentropic mixing changes

In this section, we further investigate the mechanisms of the stratospheric transport changes in response to the distribution of tropical heating. Figure 2.11 compares the residual vertical velocities at 70 hPa from the (solid) TEM definition

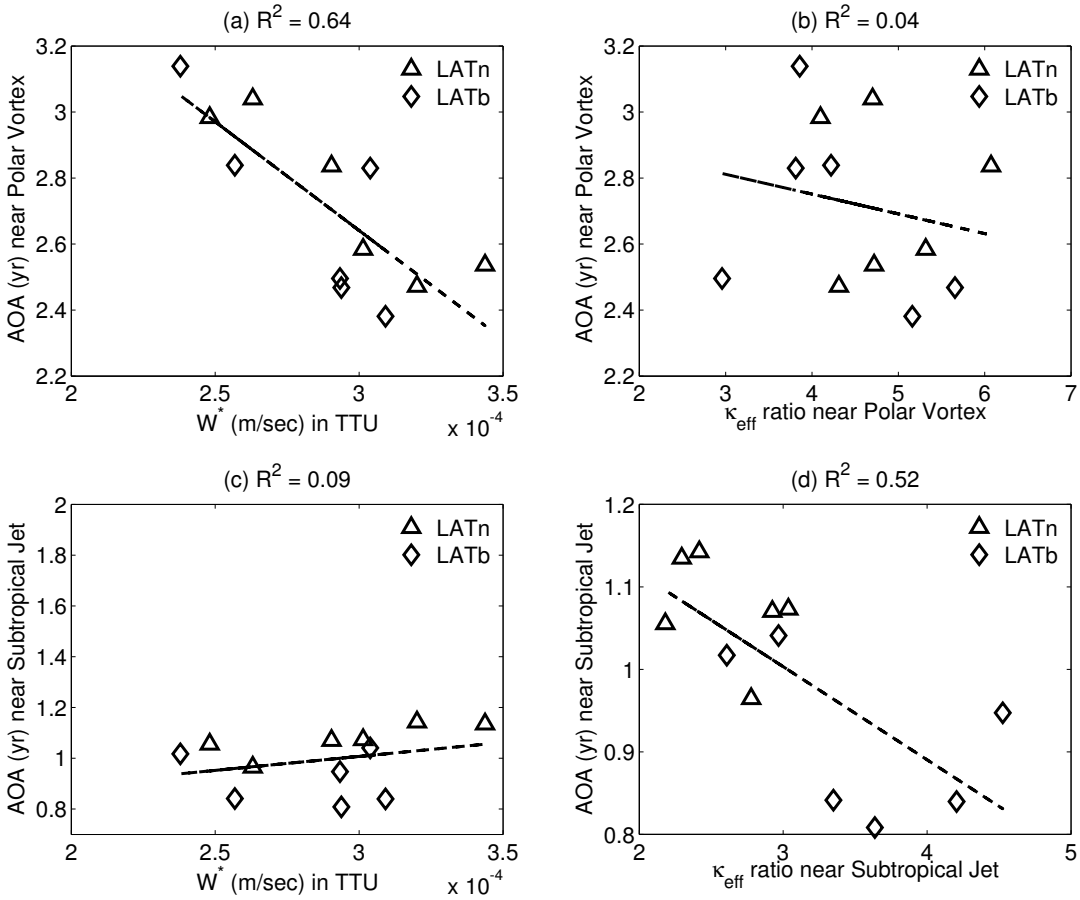

Figure 2.10: Scatter plots examining the correlation between: (a) strength of the BDC and mean AOA at the polar vortex; (b) strength of isentropic eddy mixing at the edge of the polar vortex and mean AOA at the polar vortex; (c) strength of the BDC and mean AOA on the poleward side near the subtropical jet; and (d) strength of isentropic eddy mixing and mean AOA both near the subtropical jet. Here, the strength of the BDC is denoted by the residual vertical velocity $\bar{w}^*$ ($\mathrm{m\,sec^{-1}}$) in the tropical tropopause upwelling (15°S – 15°N, 70 hPa); the strength of isentropic eddy mixing is assessed by the equivalent length ratio $\tilde{\kappa}_{eff}$ at the northern subtropical jet (25°N – 30°N, 330 K) and the edge of the northern polar vortex (55°N – 60°N, 450 K) separately; and, at last, the mean AOA (yr) is averaged near the subtropical jet (40°N – 45°N, 200 hPa) and at the polar vortex (60°N – 65°N, 70 hPa). Experiments with LATn and LATb heating are marked as △ and ◇, respectively.

$\bar{w}^*$, (dashed) the momentum balance via the 'downward control' mechanism $\bar{w}^*_m$, and (dash-dotted) the thermodynamic balance $\bar{w}^*_Q$. The anomalies are compared with the climatological residual vertical velocity in the control run scaled by a factor of 1/3 (thin solid line). For all SST forcings, the anomalies of $\bar{w}^*$, $\bar{w}^*_m$ and $\bar{w}^*_Q$ show a qualitatively good agreement with each other. This confirms that the acceleration of the residual circulation in the lower stratosphere in our SST experiments is eddy-driven and that the eddy-driven circulation is consistent with the diabatic heating change. Moreover, compared with the climatological single cell with tropical upwelling and extratropical downwelling, LONn heating tends to establish two anomalous cells (Figure 2.11 (a)(c)). One anomalous cell lies in the climatological upwelling zone and the other is located in the downwelling zone, which is consistent with the residual stream function changes shown in Figure 2.4 (a)(c). In particular, the anomalous downwelling in the high latitudes is associated with an anomalous upwelling in the midlatitudes. By contrast, for LONs heating (Figure 2.11 (b)(d)), the residual vertical velocities anomalies intensify the climatological mean pattern of tropical upwelling and extratropical downwelling, consistent with Figure 2.4 (b)(d). In summary, the shallow residual circulation response to the LONn heating is accompanied by an anomalous tropical cell and an extratropical cell out of phase with the climatological mean pattern, and the deep response to the LONs heating is associated with an anomalous equator-to-pole cell reinforcing the mean pattern.

Which mechanisms drive the distinct residual circulation changes with respect to the distribution of SST forcing? In the climatological mean (Figure 2.6, bottom), planetary waves propagate into the stratosphere and are dissipated in the midlatitude surf zone, driving the residual circulation through the

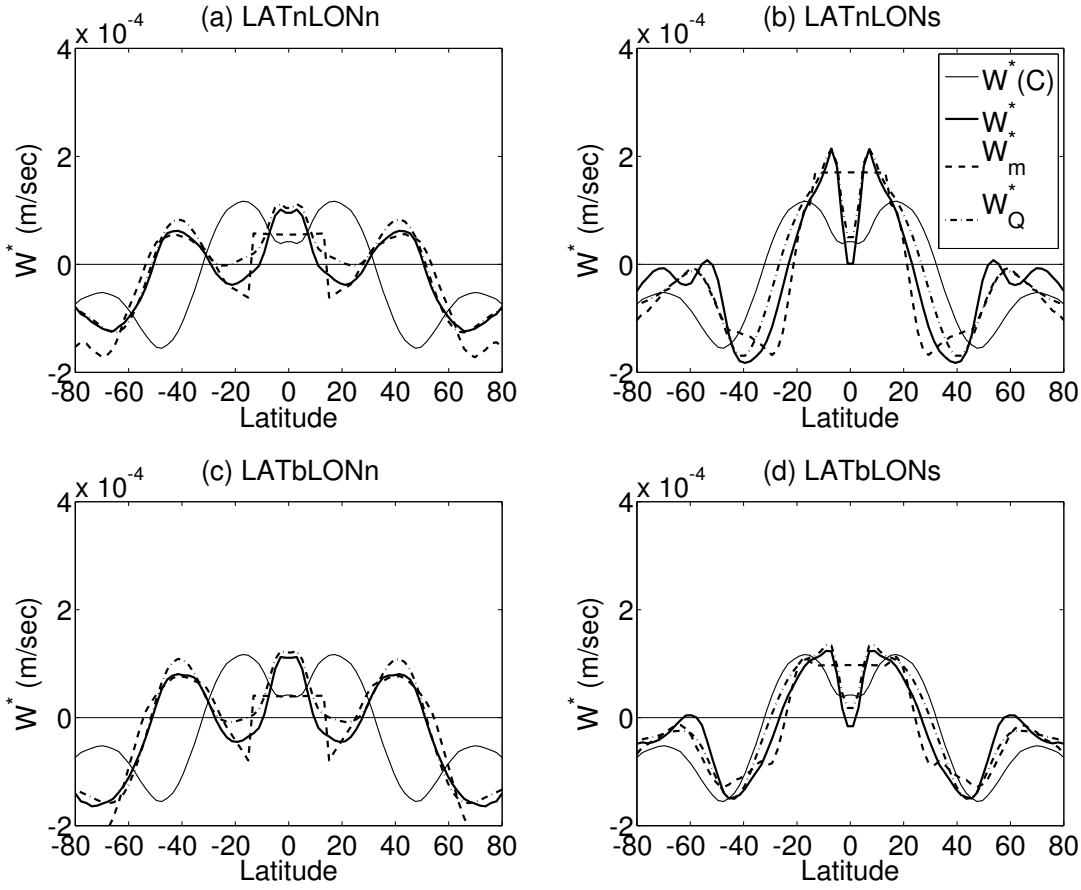

Figure 2.11: Anomaly of the residual vertical velocity at 70 hPa (units: $\mathrm{m\,sec^{-1}}$) from different definitions: $\bar{w}^*$ (bold); from 'downward control' (i.e. dynamic balance) $\bar{w}^*_m$ (dashed); and from thermodynamic balance $\bar{w}^*_Q$ (dash-dotted). The corresponding climatological $\bar{w}^*$ in the control run is shown as the thin solid line and has been scaled by a factor of 1/3. The anomalies are plotted for (a) LATnLONn; (b) LATnLONs; (c) LATbLONn; and (d) LATbLONs.

downward control mechanism. For LONn heating (Figure 2.12 (a)(c)), the deep convection generates stationary planetary waves in tropical upper troposphere. Additionally, the prescribed SST perturbation alters the extratropical baroclinity. This acts to generate more transient waves at the lower boundary, including both synoptic waves and planetary waves. The convection-induced stationary planetary waves not only dissipate heavily in the tropical lower stratosphere,

but also propagate away from their source and dissipate in the extratropical stratosphere. The extratropical transient waves, on the other hand, experience less dissipation in the mid-latitude troposphere ($40^\circ - 60^\circ$N/S, 200 – 400 hPa), resulting in increased dissipation in the stratosphere. The tropical cell of anomalous residual circulation (cf. Figure 2.4(a)(c)) is primarily due to the convection-induced stationary waves while the extratropical cell is attributed to changes in both convection-induced stationary waves and extratropical transient waves (not shown here).

For LONs heating (Figure 2.12 (b)(d)), there is also an anomalous EP flux divergence in the upper troposphere. The change in EP flux roughly follows the shift of the subtropical jet, and therefore the maximum anomalous divergence occurs on the equatorward side of 40°N for LATn heating and on the poleward side of 40°N for LATb heating at 200 – 400 hPa. In contrast to the responses to LONn heating, the upward propagation of these waves is not directly accompanied by an EP flux convergence between 40-100 hPa, where the zonal wind is increased considerably due to the upward shift of the subtropical jet. Instead, the planetary waves propagate either more equatorward or upward from these regions of enhanced zonal winds, which in turn drives a deeper overturning circulation (Figure 2.4 (b)(d)).

Given the remarkable similarity between the stratospheric circulation in the LATn and LATb runs, the generation and propagation of waves in the troposphere are of secondary importance in comparison with the eddy propagation and dissipation in the stratosphere, which drives distinct responses in the residual circulation between LONn and LONs heating. The lower stratospheric response is therefore investigated further: a key difference between the shallow

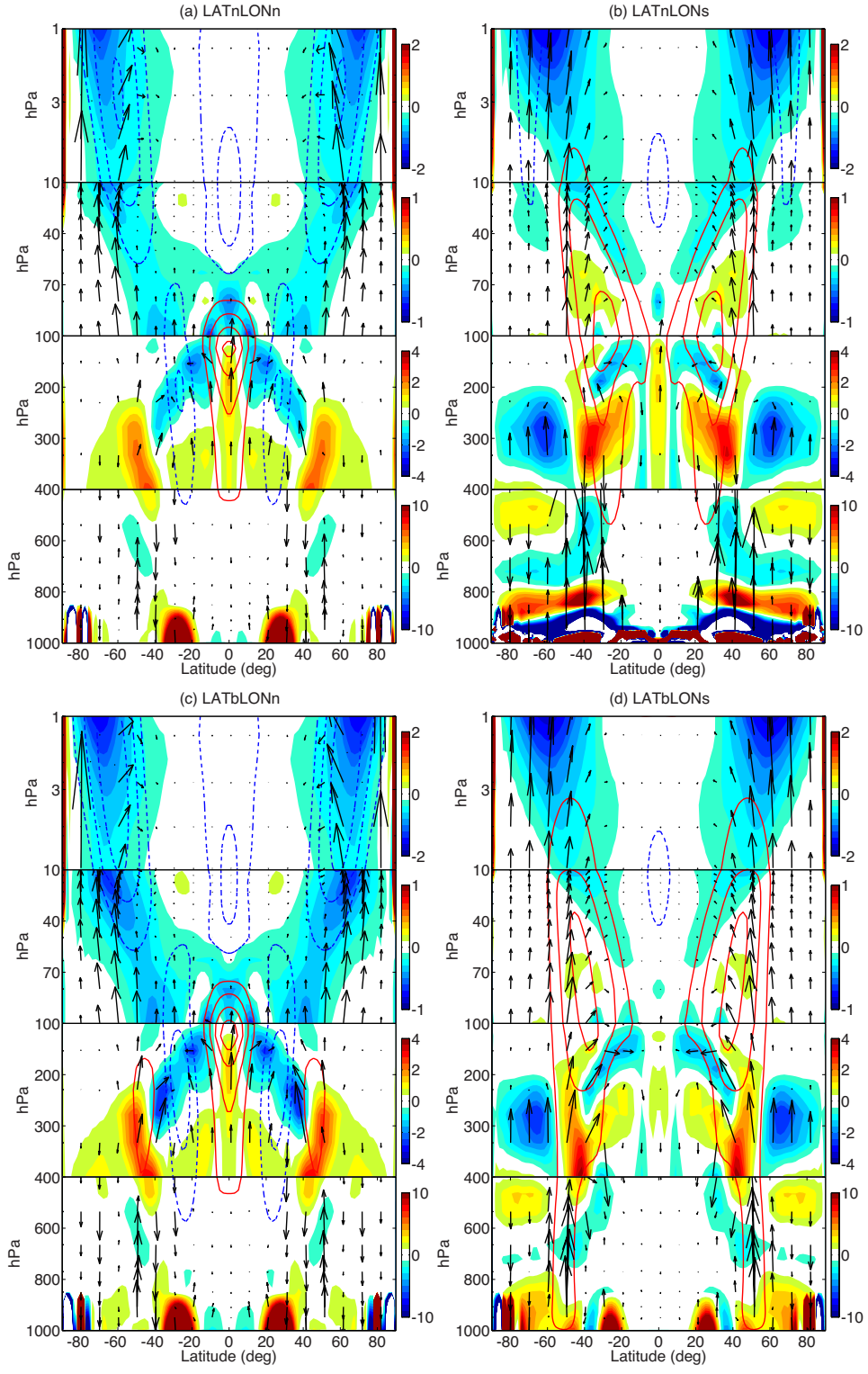

Figure 2.12: As in Figure 2.3, but for the EP flux (vectors) and associated divergence **DF** (shading, units: m $sec^{-1}day^{-1}$), and zonal mean zonal wind (contours, units: m sec^{-1}). The contour interval is 4 m sec^{-1}. Note that the vertical axis has been changed to 1-1000 hPa.

and deep responses in the residual circulation appears in the EP flux convergence (i.e. the eddy dissipation) in the subtropical lower stratosphere. With all the sensitivity experiments examined in Section 4, we further found a strong correlation in the lower stratosphere between the meridional component of the EP flux in the midlatitudes ($40^\circ - 60^\circ$) and the strength of subtropical eddy dissipation, suggesting that an increased equatorward propagation of midlatitude waves in the lower stratosphere leads to more eddy dissipation in the subtropics.

The changes in eddy propagation can be explained by a change in the refractive index of Rossby waves n^2 (Figure 2.13). Eddies are able to propagate in regions of positive refractive index n^2, and they propagate from the regions of low values of the refractive index to the regions of high index values. Our calculation of the refractive index follows Matsuno (1970). For the transient planetary waves which are dominant in our model, we set the value of the eddy phase speed to $c_p = 5\,\mathrm{m\,sec^{-1}}$, and the zonal wavenumber to $k = 3$. The results are qualitatively similar for choosing the wavenumber $k = 2$ or 4, or for a moderate variation of the phase speed c_p, and the conclusions made here are also valid for the stationary planetary waves which are important for LONn heating response.

For the LONn heating (Figure 2.13 (a)(c)), pronounced negative anomalies of the refractive index n^2 are found at $40^\circ - 50^\circ$ whereas positive anomalies are found poleward of 60° near and above 100 hPa. This enhances the meridional gradient of the refractive index from a minimum in the midlatitudes to a maximum at the edge of the polar vortex (contours in Figure 2.13(a)(c)). Considering that the majority of the anomalous waves penetrating the tropopause reside

poleward of 50° (cf. Figure 2.12 (a)(c)), the enhanced meridional gradient of the refractive index prevents equatorward wave propagation and guides these waves poleward. As the waves are approaching the critical line near the edge of the polar vortex, the waves break down and dissipate, driving a shallow, extratropical strengthening of the residual circulation. On the contrary, for the LONs heating (Figure 2.13 (b)(d)), the anomaly in the refractive index results in a decline or even reversal of the climatological meridional gradient of the refractive index (not shown). Given that the majority of anomalous waves penetrating the tropopause resides equatorward of 50° for LONs heating (cf. Figure 2.12 (b)(d)), the declined or reversed meridional gradient of the refractive index forces these anomalous waves to propagate equatorward and to dissipate near the critical line in the subtropical lower stratosphere. Consequently, this leads to a deeper and broader strengthening of the residual circulation. We have further decomposed the refractive index n^2 into the meridional wavenumber l and vertical wavenumber m using the diagnostic described in Harnik and Lindzen (2001) (Figures not shown here). The results confirm an equatorward shifted zone of meridional wave propagation given by l^2 and further an equatorward EP flux convergence in the middle and upper stratosphere (1 – 10 hPa) given by m^2 for LONs heating. This diagnostic suggests that the distinct responses of stratospheric eddy dissipation between LONn and LONs heating are indeed due to different pathways of eddy propagation in the stratosphere, which cause different types of strengthening of the stratospheric residual circulation.

With a simple diffusive closure, one can relate the pattern of EP flux divergence to the isentropic mixing of PV (Yang et al., 1990). Thus, it can be expected that the simulated changes in isentropic mixing are associated with changes in eddy dissipation through Rossby wave breaking. This can be confirmed by the

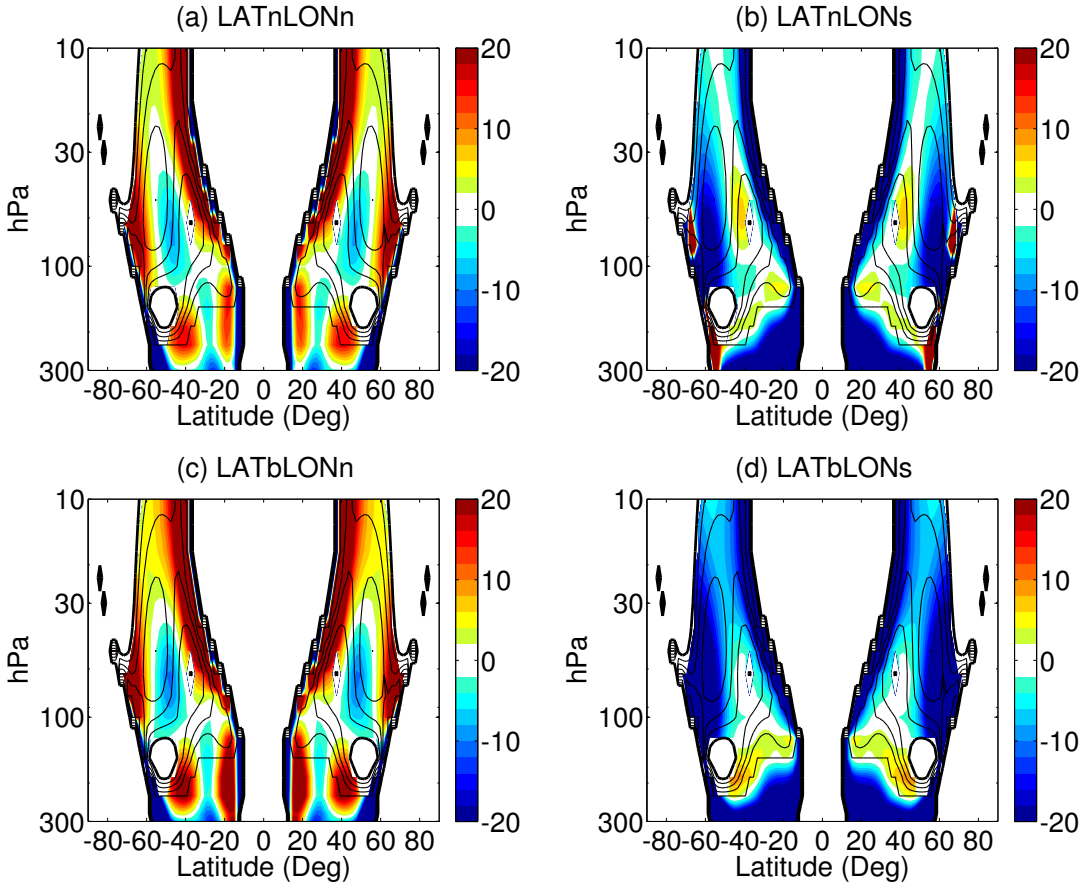

Figure 2.13: Anomaly of the refractive index for: (a) LATnLONn; (b) LATnLONs; (c) LATbLONn; and (d) LATbLONs, with the corresponding climatology in the control run shown as contours (interval: 10). The bold contour indicates both the zero line and the critical line, separating the regions of propagation from those of no propagation.

increase in isentropic mixing near the stratospheric jets ($50^\circ - 60^\circ$) (shading in Figure 2.7(a)(c)), which overlaps with the region of extratropical anomalous EP flux convergence (shading in Figure 2.12(a)(c)) for LONn heating. Similarly, the regions of decreased isentropic mixing within the surf zone ($20^\circ - 40^\circ$) (shading in Figure 2.7(b)(d)) overlap with the region of subtropical anomalous EP flux divergence (shading in Figure 2.12(b)(d)) for LONs heating.

As noted in Section 2.3, we also find that the response of the isentropic mix-

ing to tropical SST forcing generally mirrors the changes in zonal mean zonal wind in all our experiments (cf. Figure 2.7). Although both EP flux convergence and the zonal wind vary consistently with the changes of isentropic mixing in the stratosphere, it is interesting to note that changes in the zonal wind seem to be a better predictor of the changes in eddy mixing than the EP flux convergence in the troposphere. For example, there is a significant decrease in isentropic mixing in the tropical upper troposphere (cf. Figure 2.7(a)(c)) for LONn heating that mirrors the eastward acceleration of equatorial zonal mean zonal winds. This effect dominates over the increased local eddy dissipation (cf. Figure 2.12(a)(c)) in favor of a larger mixing. This seems to be consistent with simple kinematic models of tracer transport with a prescribed jet and stochastic noise, which suggests that the jet structure has a dominant control on tracer mixing (Haynes et al., 2007).

2.6 Summary and Discussion

The sensitivities of the BDC to tropical SST heating are investigated in an idealized aqua-planet model. It is found that an increase in tropical SSTs generally leads to an acceleration of tropical upwelling and an associated reduction in AOA in the polar stratosphere. AOA near the subtropical tropopause is correlated with local isentropic mixing of tropospheric and stratospheric air. The spatial distribution of the SST forcing influences stratospheric transport including the diabatic circulation, AOA, and isentropic mixing. More specifically, while the locations of tropospheric wave generation and propagation depend on the meridional width of the SST heating (see also Chen et al., 2010), the zonal distribution of SST perturbations has a more pronounced impact on the vertical

and meridional structures of transport and mixing in the stratosphere: Longitudinally narrow (LONn) SST heating tends to generate a shallow acceleration of the stratospheric residual circulation, enhanced isentropic mixing associated with a weakened stratospheric jet, and a reduction in the AOA mostly within the polar vortex. By contrast, longitudinally symmetric (LONs) SST heating tends to produce a deep strengthening of the stratospheric residual circulation, suppressed isentropic mixing associated with a stronger stratospheric jet, and a decline of AOA in the entire stratosphere. As the SST perturbation is gradually varied from zonally localized to zonally symmetric, the shallow residual circulation response abruptly transitions to a deep response. Gerber (2012) also found a tropospheric control of the shallow branch of the BDC by surface topographic forcing, and a stratospheric control of the deep branch by the intensity of the polar vortex. Our results suggest that a zonally symmetric SST heating can also control the deep branch of the BDC through the strength of the subtropical jet and the associated thermal wind aloft, while tropical SST heating localized in longitude can control the shallow branch by convection-induced planetary waves. Therefore, while our idealized model simulation corresponds to the annual mean circulation for simplicity, a similar mechanism can operate in the winter stratosphere where the stratosphere-troposphere coupling is more active with stationary waves.

The changes in the residual circulation are induced by the planetary wave drag through the downward control mechanism (Haynes et al., 1991). Although the meridional width of tropical SST heating influences the locations of baroclinic wave generation and propagation, it is the wave propagation and dissipation in the subtropical lower stratosphere that are responsible for the depth of the stratospheric residual circulation response. Zonally localized SST heat-

ing weakens the stratospheric jet and guides the planetary waves poleward in the lower stratosphere, leading to a shallow change in the residual circulation. By contrast, the zonal wind response to zonally symmetric SST heating is characterized by an upward shift of the subtropical jet, which in turn refracts the planetary waves equatorward and upward in the lower stratosphere, leading to a deep change in the residual circulation. This also yields weaker isentropic mixing associated with a more robust transport barrier due to a stronger subtropical jet. Our results suggest that while the recent decadal changes in the shallow branch of the BDC (Bönisch et al., 2011) may be partially attributed to a more basin-wide SST trend, the upward shift of the subtropical jet associated with zonally symmetric SST heating, as found in chemical climate model simulations under climate warming (Garcia and Randel, 2008, McLandress and Shepherd, 2009, Garny et al., 2011), can impact the deep branch of the BDC.

CHAPTER 3

STRATOSPHERIC IMPACTS ON THE TROPOSPHERE: THE ROLE OF OZONE DEPLETION

3.1 Introduction

Substantial evidences have suggested that the SH summertime circulation trends over the late twentieth century are primarily caused by the anthropogenic Antarctic ozone hole in spring (see Polvani et al., 2011, and references therein). These circulation changes are characterized by a strengthening of the circumpolar winds in the lower stratosphere, an accelerated polar downwelling in the stratosphere (McLandress et al., 2010, Lin and Fu, 2013), and a trend towards the positive phase of the Southern Annular Mode (SAM) in the troposphere associated with a poleward shift of the tropospheric eddy-driven jet (see the review by Thompson et al., 2011).

Given the complex interplay between chemistry, radiation, and dynamics in the tropospheric response to stratospheric ozone depletion, the underlying mechanism(s) have not been fully understood (Thompson et al., 2011). By directly imposing stratospheric ozone loss, Orr et al. (2012) found the feedback between the upward cross-tropopause propagation of planetary waves and the strength of the stratospheric polar vortex is crucial to explain the downward influence of the ozone depletion radiative cooling on the tropospheric jet shift. In an idealized model, Kushner and Polvani (2004, KP04 hereafter) showed the tropospheric jet moves poleward in response to idealized polar stratospheric cooling, and emphasized the importance of eddies. Using a similar model, Song and Robinson (2004) found that the tropospheric response to stratospheric forc-

ing is largely reduced when planetary waves are damped. Recently, Sun et al. (2014) stressed that the delay in the breakdown of the polar vortex is crucial in producing a deep response in planetary waves that can in turn influence the tropospheric circulation.

It is then important to understand how the stratospheric perturbation from ozone depletion can impact the synoptic waves in the troposphere that dominate the tropospheric variability. Three mechanisms are illustrated schematically in Fig. 3.1. Firstly, the radiative cooling from the ozone depletion can directly influence the synoptic eddies in the upper troposphere and lower stratosphere via increased tropopause height (Williams, 2006, Lorenz and DeWeaver, 2007, Simpson et al., 2009) or accelerated synoptic eddy phase speed (Wittman et al., 2007, Chen and Held, 2007). Through interactions with the zonal flow, these synoptic eddy anomalies in the lower stratosphere can further communicate with the tropospheric synoptic eddies. Secondly, the radiative cooling can produce a stratospheric planetary wave change, and this anomalous planetary wave drag can induce a residual mean meridional circulation that extends downwards into the troposphere, as described by the downward control mechanism (Haynes et al., 1991). In the troposphere, a weak zonal flow anomaly associated with the residual circulation can be amplified by a positive synoptic eddy feedback (e.g., Lorenz and Hartmann, 2001). This was summarized as the downward control with eddy feedback (DCWEF) mechanism by Song and Robinson (2004), who found a more poleward tropospheric jet when an eastward zonal torque is applied to the polar stratosphere. Lastly, the stratospheric zonal flow anomalies, initiated by the ozone depletion radiative cooling, can impact planetary eddies through wave propagation (Chen and Robinson, 1992) and wave refraction (Shaw et al., 2010). While propagating downward, the

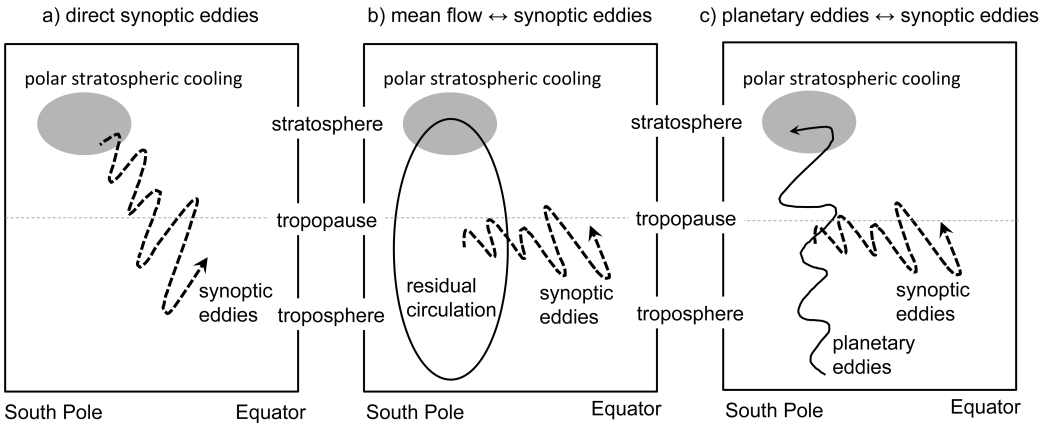

Figure 3.1: Mechanisms by which ozone depletion-like stratospheric cooling impacts synoptic eddies: a) the stratospheric radiative cooling induces a direct impact on synoptic eddies; b) the stratospheric radiative cooling generates planetary wave drag anomalies, and a planetary wave-induced residual circulation impacts synoptic eddies by the anomalous zonal flow associated with the residual circulation; c) the stratospheric radiative cooling impacts the planetary waves in the stratosphere and troposphere via changes in reflection and propagation, which altered planetary waves then interact with the synoptic eddies by nonlinear eddy-eddy interactions.

changes in planetary eddies can directly couple with synoptic eddies via nonlinear eddy-eddy interaction to produce a pronounced tropospheric response.

Although most previous studies have focused on the tropospheric responses to stratospheric perturbations in the winter solstice, idealized models can also simulate qualitatively the seasonal cycle in the Brewer-Dobson Circulation (BDC) from winter to summer (Chen and Sun, 2011) and the final breakdown of the polar vortex in spring (Sun and Robinson, 2009, Sun et al., 2011). Sun et al. (2014) used the idealized model of KP04 to simulate the pattern and timing of the observed trends in austral summer by applying idealized radiative

cooling to the polar stratosphere in spring. They found the timing of the stratospheric polar vortex breakdown and planetary wave drag is critical for the tropospheric response. Specifically, while the synoptic eddies can interact with the polar stratospheric cooling in both delayed stratospheric final warming (SFW) and undelayed SFW events, only the composite from the years with delayed SFW has a strong tropospheric circulation responses, accompanied by distinct behaviors of the lower-stratosphere temperature anomalies and planetary eddies (see their Fig. 10 and 11 respectively). This indicates that both the radiative cooling and the eddies can be crucial in interpreting the the downward influence of stratospheric ozone depletion-like cooling towards tropospheric circulation. As such, in this work, we will further separate the mechanisms of transient circulation responses simulated in this model (Sun et al., 2014).

The paper is organized as follows. Section 3.2 introduces the diagnostics in a quasi-geostrophic framework to separate the wind tendency into contributions from polar stratospheric cooling and eddy forcings. The idealized model of the atmosphere used in this study is described in Section 3.3. In Section 3.4, we present the analysis of the transient circulation responses to stratospheric ozone depletion-like cooling. Conclusions are given in Section 3.5. Details of the zonally symmetric model are summarized in the appendix.

3.2 Diagnostics in a quasi-geostrophic framework

For simplicity, we introduce the diagnostics using a quasi-geostrophic (QG) framework. Following Eq. (3.5.7) in Andrews et al. (1987), the zonal wind ten-

dency can be written as

$$\mathcal{L}(\frac{\partial \overline{u}}{\partial t}) \equiv [\frac{\partial^2}{\partial y^2} + \frac{1}{\rho_0}\frac{\partial}{\partial z}(\rho_0 \frac{f_0^2}{N^2}\frac{\partial}{\partial z})]\frac{\partial \overline{u}}{\partial t} = \frac{\partial^2}{\partial y^2}(\frac{1}{\rho_0}\nabla \cdot F + \overline{X}) - \frac{1}{\rho_0}\frac{\partial^2}{\partial z \partial y}(\frac{\rho_0 f_0 \overline{\mathcal{H}}}{d\theta_0/dz}) \quad (3.1)$$

where $\mathcal{L}(X) = \frac{\partial^2 X}{\partial y^2} + \frac{1}{\rho_0}\frac{\partial}{\partial z}(\rho_0 \frac{f_0^2}{N^2}\frac{\partial X}{\partial z})$ is a linear elliptic operator and its inversion, denoted as $\mathcal{L}^{-1}(X)$, can be nonlocal. $\rho_0(z) \propto e^{-z/H}$, $N^2(z) = \frac{g}{\theta_0}\frac{d\theta_0}{dz}$, $\nabla \cdot F$ denotes the Elliassen-Palm flux divergence, $\overline{X}$ denotes momentum forcing (i.e., surface friction and unresolved wave drag), $\overline{\mathcal{H}}$ denotes diabatic heating, and readers are referred to Andrews et al. (1987) for conventions of other symbols. Given appropriate boundary conditions, the zonal wind tendency can be attributed linearly through the inverted operator $\mathcal{L}^{-1}$ to the eddy forcing, momentum forcing, and diabatic heating, respectively. The nonlocal response takes place through altered residual overturning circulations that are implicit in the operator.

Using the radiative cooling rate from ozone depletion Q, we can obtain the tendency of the anomalous zonal wind ($\delta\overline{u}$) as

$$\frac{\partial \delta\overline{u}^Q}{\partial t} = -\mathcal{L}^{-1}[\frac{1}{\rho_0}\frac{\partial^2}{\partial z \partial y}(\frac{\rho_0 f_0 \overline{Q}}{d\theta_0/dz})] \quad (3.2)$$

Similarly, we can obtain the anomalous zonal wind tendencies due to the changes of planetary wave forcing δF^p and synoptic eddy forcing δF^s as

$$\frac{\partial \delta\overline{u}^p}{\partial t} = \mathcal{L}^{-1}[\frac{\partial^2}{\partial y^2}(\frac{1}{\rho_0}\nabla \cdot \delta F^p)] \quad (3.3)$$

$$\frac{\partial \delta\overline{u}^s}{\partial t} = \mathcal{L}^{-1}[\frac{\partial^2}{\partial y^2}(\frac{1}{\rho_0}\nabla \cdot \delta F^s)] \quad (3.4)$$

The total zonal wind response to radiative cooling and eddy forcings can be obtained as $\delta\overline{u} = \delta\overline{u}^Q + \delta\overline{u}^p + \delta\overline{u}^s$.

For the second mechanism shown in Fig. 3.1(b), the polar stratospheric cooling and planetary wave forcing can induce a zonal wind change via the residual circulations, as diagnosed from $\delta\overline{u}^Q + \delta\overline{u}^p$ (note that this includes planetary waves

in both the stratosphere and troposphere). As synoptic eddies can provide a positive feedback to the zonal jet variability (e.g., Lorenz and Hartmann, 2001), the positive feedback is expected to maintain or amplify the zonal jet shift that is diagnosed from $\delta\overline{u}^Q + \delta\overline{u}^p$. On the other hand, as shown in Fig. 3.1(c), stratospheric cooling and the resultant polar vortex change may alter planetary wave propagation (Chen and Robinson, 1992) and reflection (Shaw et al., 2010) in the vertical direction. The change in planetary waves may impact synoptic eddies directly via nonlinear eddy-eddy interactions.

It should be noted that boundary conditions are crucial for the diagnostics in the QG framework (Haynes and Shepherd, 1989). To avoid this problem, we have used the same idealized model (described in Section 3.3) to construct a zonally symmetric model with the same boundary conditions. Also, eddy forcings are computed directly within the same model (described in the appendix) to be consistent with the model discretization in the horizontal and vertical directions.

3.3 Model Setup

We use the Geophysical Fluid Dynamics Laboratory (GFDL) atmospheric dynamical core at T42 horizontal resolution and 40 unevenly-spaced sigma levels. Following Kushner and Polvani (2006), the control simulation is forced by a Newtonian relaxation towards a prescribed time-dependent zonally symmetric radiative equilibrium temperature profile, T_{eq}, and damped by a linear friction in the planetary boundary layer. As illustrated by contours in Fig. 3.2, T_{eq} in the polar stratosphere is set by the lapse rate $\gamma = 6\,\mathrm{K\,km^{-1}}$ in midwinter and $\gamma = 0$

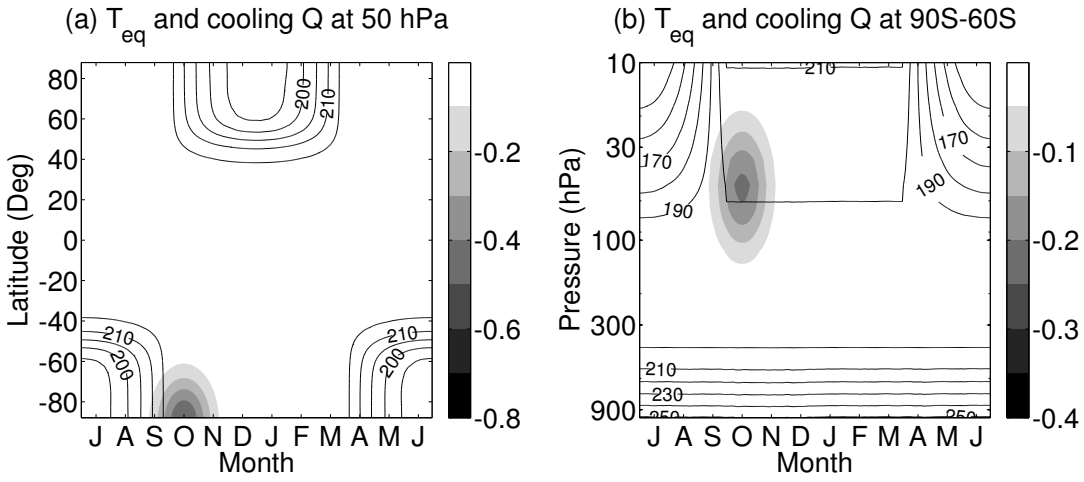

Figure 3.2: The annual cycle of the equilibrium temperature profile (contours, unit: K, interval: 5K) in the control run and additional ozone depletion-like radiative cooling in the perturbation run (shadings, unit: $\mathrm{K\,day^{-1}}$). The figure shows (a) the meridional distribution at 50 hPa and (b) vertical distribution averaged over polar cap (90°S – 60°S).

in midsummer, and the variation between midwinter and midsummer induces a stratospheric seasonal cycle (here γ is defined in the same way as in Eq. (3) of KP04). T_{eq} in the troposphere, on the other hand, is set by a hemispheric asymmetry parameter $\epsilon = 10\,\mathrm{K}$ to yield perpetual austral summer. This setup ensures that the downward influence of SFWs in the troposphere is initialized from the stratosphere. Moreover, there is no topography, but planetary waves can be generated through nonlinear interactions of baroclinic waves (Scinocca and Haynes, 1998).

In the perturbation run, following Sun et al. (2014), radiative cooling induced by stratospheric ozone depletion is mimicked by idealized polar stratospheric cooling in spring as

$$Q(\phi,\sigma,t) = 0.5\,\mathrm{K\,day^{-1}} \exp\left\{-\left[\frac{(\phi-\phi_0)^2}{2\sigma_\phi^2} + \frac{(-7000\ln\sigma + 7000\ln\sigma_0)^2}{2\sigma_\sigma^2} + \frac{(t-t_0)^2}{2\sigma_t^2}\right]\right\} \tag{3.5}$$

Here the parameters $\phi_0 = -1.57$, $\sigma_\phi = 0.28$, $\sigma_0 = 0.05$, and $\sigma_\sigma = 4000$ (where ϕ denotes the latitude, the sigma level $\sigma = p/p_s$, p is the pressure, and p_s is the surface pressure) define the spatial pattern of cooling (similar to Butler et al., 2010). The time t_0 (corresponds to October 1), $\sigma_t = 20$ days, and the time t define the peak and persistence of cooling. The pattern of cooling is shown by shadings in Fig. 3.2, which mimics the observed structure of the Antarctic ozone hole (e.g., Fig. 1 in Polvani et al., 2011). As such, we have assumed that the polar stratospheric cooling in observations is dominated by the radiative cooling due to the ozone depletion, although our simulations can also produce small dynamical cooling due to the residual circulation anomalies driven by altered wave forcing in the presence of anomalous radiative cooling (Fig. 3.4 (g)(i)).

The control run (FM_C) is integrated for 80 years after a year of spin-up is discarded. Starting from the beginning of austral autumn each year, a year of time slice experiment is performed with the polar stratospheric cooling (Eq. (3.5)) turned on in the spring to form an 80-year ensemble of perturbed run (FM_F). A brief summary of the numerical experiments and notations of experiments are described in Table 3.1. The perturbed run minus the control run is referred to as the *ozone depletion* response (i.e., $FM_F - FM_C$).

In order to assess the effects of planetary eddies and synoptic eddies in the downward influence of polar stratospheric cooling on the tropospheric circulation, a zonally symmetric model is constructed as in KP04. With only zonal mean quantities being resolved, the zonally symmetric model is unable to simulate eddy forcings directly. The eddy effect on the zonal mean flow can be assessed by adding the eddy forcings extracted from the full model (i.e., FM_F), as external forcings, to the zonally symmetric model for integration of the zonal

means of zonal wind, meridional wind, temperature, and surface pressure, respectively. Unlike KP04 who used the time-mean eddy forcings, here we have calculated 80-year mean annual cycles of eddy forcings in the full model (i.e., FM_F) to drive the zonally symmetric model (see the appendix for details).

As illustrated in the QG framework in Section 3.2, the transient *ozone depletion* responses (i.e., $FM_F - FM_C$) can be separated by individual responses to radiative cooling with no eddy forcing, planetary eddy changes alone (zonal wavenumbers 1-3), and synoptic eddy changes alone (zonal wavenumbers 4 and above). These three perturbation simulations minus the corresponding control run in the zonally symmetric model are separately referred to as *radiative cooling*, *planetary eddy*, and *synoptic eddy* responses (i.e., $ZM_Q - ZM_C$, $ZM_P - ZM_C$, and $ZM_S - ZM_C$). Furthermore, the zonally symmetric model simulation with all these three forcings included (i.e., $ZM_F - ZM_C$) successfully reproduces the *ozone depletion* responses in the full model (i.e., $FM_F - FM_C$, cf. the full model in Figs. 3.3 (d)(e)(f) and the zonally symmetric model in Figs. 3.4 (a)(b)(c)).

3.4 Results

We first compare the transient responses to polar stratospheric cooling simulated in the idealized model with the observed trends in the European Center for Medium-Range Weather Forecasts (ERA-Interim) reanalysis (Dee et al., 2011) (Fig. 3.3). The observed trends are calculated with a linear trend for the years 1979-2002 and the months of September-February, when pronounced ozone depletion has developed in the stratosphere followed by tropospheric signals (e.g., Thompson et al., 2011).

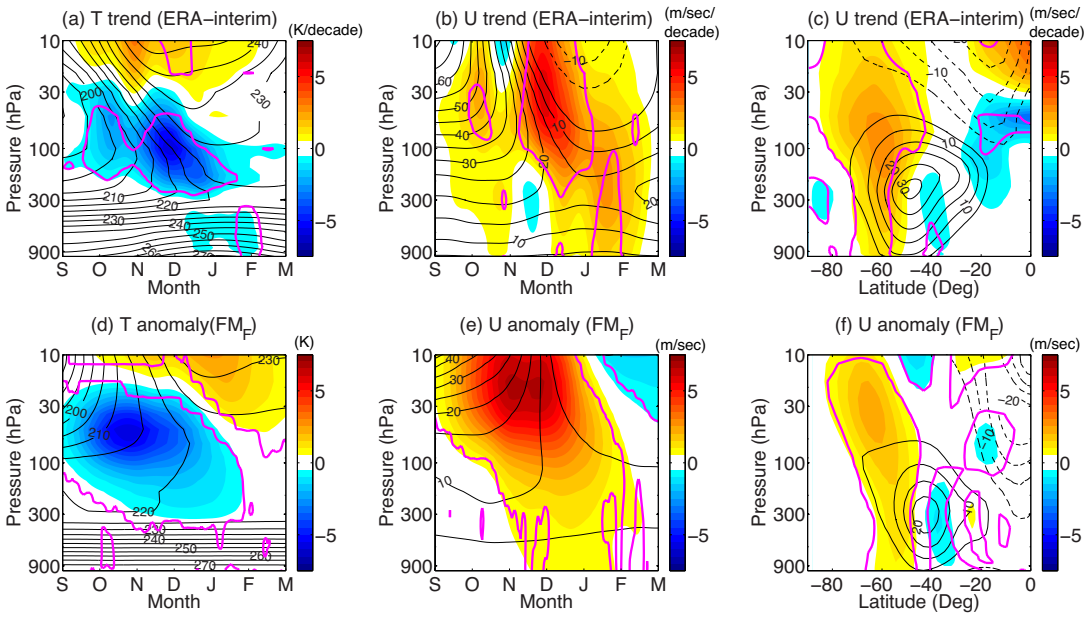

Figure 3.3: Comparison between the ERA-interim reanalysis (top) and the idealized full model with ozone depletion-like cooling (bottom). The figure shows: (a)(d) the temporal variation of zonal mean temperature within the polar cap (averaged over 90°S – 60°S), (b)(e) the temporal variation of zonal mean zonal winds at the edge of the polar cap (averaged over 70°S – 50°S), and (c)(f) latitude-altitude cross section of zonal mean zonal winds during the austral summer (DJF). Climatologies are shown as contours (solid for positive values and dashed for negative). Shades denote the trends over 1979-2002 (K dec^{-1} for temperature or m sec^{-1} dec^{-1} for zonal wind) in the ERA-interim reanalysis and the anomalies (K for temperature or m sec^{-1} for zonal wind) in the idealized model simulation, respectively. The signals in regions enclosed by purple contours are significant above the 95% confidence level using a two-sided student's t-test.

In spite of its simplicity, the idealized model can capture many important features of the observed trends in the reanalysis data. In the polar region (90°S–60°S), the temperature is cooled, as expected, in spring between 30 hPa and 300 hPa; this cooling migrates downward with dynamical warming aloft (Figs. 3.3 (a) and (d)). There is anomalous westerly wind at the edge of the polar vortex (70°S–50°S) in early summer, indicating a delayed breakdown of the polar vortex (Figs. 3.3 (b) and (e)). The westerly anomaly propagates from the stratosphere to the troposphere. In order to highlight the structure of tropospheric wind change, the zonal wind response in December-February (DJF) is plotted in the latitude-altitude cross section (Figs. 3.3 (c) and (f)). The tropospheric wind is characterized as a poleward shift of the tropospheric jet that projects positively onto the SAM. The similarities between the reanalysis data and the idealized model indicate that the polar stratospheric cooling induced by ozone depletion alone can contribute to the surface wind trends in observations, as in the idealized model.

There are also noticeable differences between the idealized model and observations. The seasonal transition of stratospheric anomalies in the model is more gradual than the observed trends, which may be attributed to the simplicity of idealized ozone-depletion cooling. In the idealized model, the maximum tropospheric zonal wind anomalies occur right after the corresponding maximum stratospheric anomalies in early summer (cf. Fig. 3.3(e)), while, in the observations, the tropospheric maximum occurs in midsummer with a distinct lag from its stratospheric counterpart. Also, the tropospheric zonal wind anomalies are more equatorward in the model than observations, which may be explained by an equatorward bias in the climatological jet. Despite these shortcomings, the model provides a simple framework to understand, at least qualitatively, the

mechanism(s) of the tropospheric response to stratospheric ozone loss.

Using the zonally symmetric model, we can separate the mechanisms of transient tropospheric response to individual forcings, as noted in Sections 3.2 and 3.3. Figure 3.4 shows a separation of atmospheric *ozone depletion* responses discussed above into contributions from radiative cooling, planetary waves, and synoptic waves. We find, as expected, that the lower stratospheric cooling initially in spring is dominated by prescribed radiative cooling. As the polar cooling without any eddy forcing tends to migrate upward as time evolves (Fig. 3.4(d)), the downward migration seen in the full model (i.e., $FM_F - FM_C$) should be attributed to the change in eddy forcing, consistent with Orr et al. (2013). Particularly, the mid-stratosphere warming in late spring and summer (Fig. 3.4(g)) is dynamically driven by the polar downwelling (not shown) associated with enhanced planetary wave drags. This is consistent with the strengthened polar downwelling of the BDC in summer simulated in chemistry-climate models with realistic ozone depletion (McLandress et al., 2010, Lin and Fu, 2013, Orr et al., 2013).

The change in subpolar zonal wind is consistent with polar cap temperature by the thermal wind relationship. Without any eddy forcing, the springtime strengthening of the polar vortex remains above the level of thermal forcing (Fig. 3.4(e)). It is therefore the eddy forcing that drives the downward propagation of westerly anomalies from the stratosphere into the troposphere. In response to planetary wave forcing, the polar stratospheric wind is strengthened in late spring and weakened in summer (Fig. 3.4(h)), which indicates a delay in the breakdown of polar vortex and planetary wave drag, as found in McLandress et al. (2010), Sun et al. (2014). For the downward propagation of anoma-

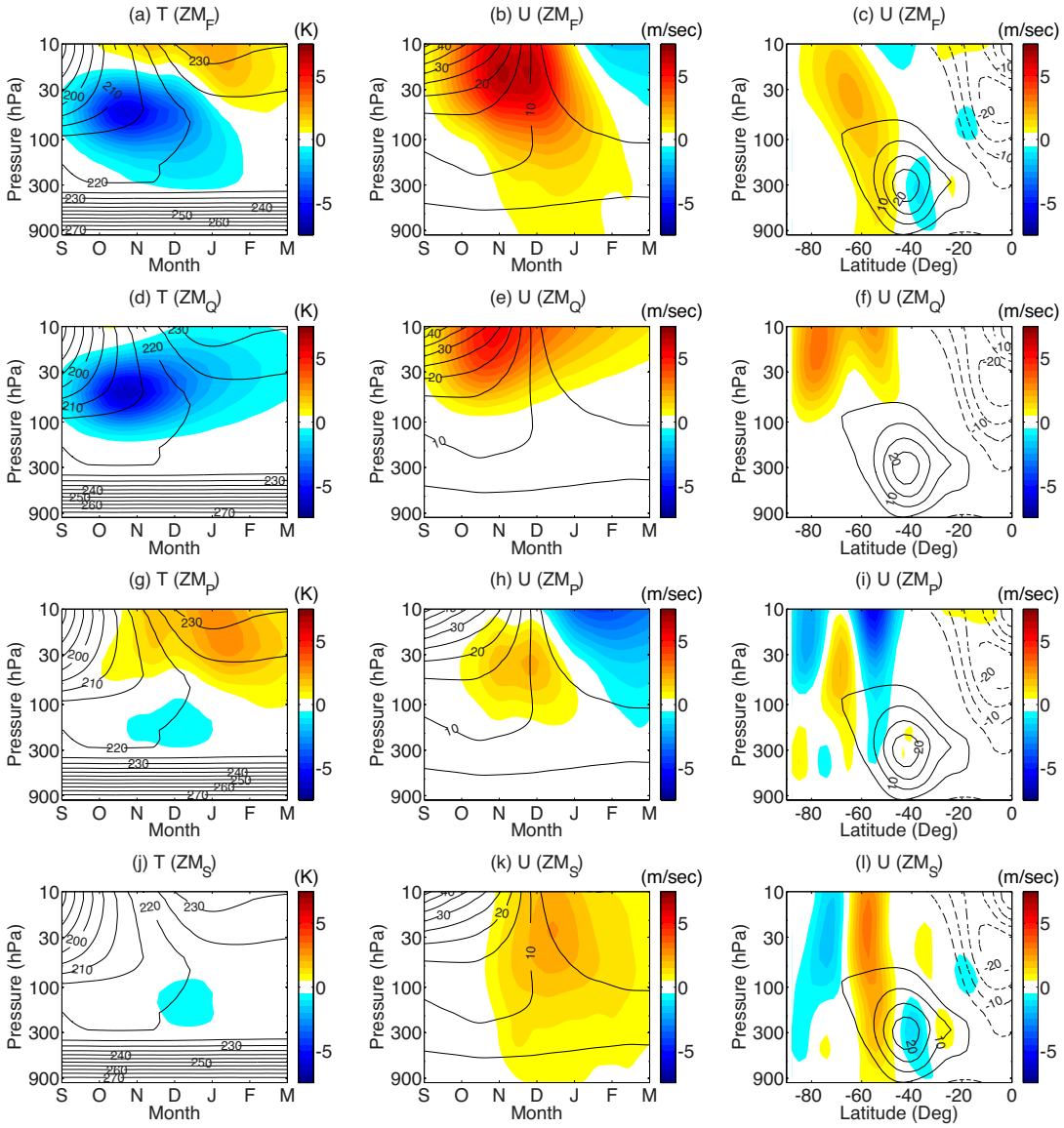

Figure 3.4: As the bottom row of Fig. 3.3, but for the anomalies in the zonally symmetric model separated by individual forcings: (a)(b)(c) with total forcing; (d)(e)(f) with *spring cooling* forcing only; (g)(h)(i) with *planetary eddy* forcing only; (j)(k)(l) with *synoptic eddy* forcing only. See the text in Section 3.3 for details.

lous westerlies, planetary waves and synoptic waves in early summer work constructively in the stratosphere and synoptic waves are the primary driver of the tropospheric signal. The increased planetary wave drag in late summer (not shown) causes anomalous stratospheric easterlies in the full model (i.e., $FM_F - FM_C$). While most of synoptic waves are confined in the troposphere, synoptic waves drive persistent anomalous westerlies from the surface to the stratosphere throughout the summer (Fig. 3.4(k), also seen in Fig. 3.4(l) and it will be discussed later).

As for the meridional structure of zonal wind in austral summer (DJF), spring cooling with no eddy forcing can induce a zonal wind increase only in the polar stratosphere (Fig. 3.4(f)). By contrast, planetary waves lead to the zonal wind deceleration at 50°S-60°S and acceleration at 60°S-70°S, and these signals extend downward into the upper troposphere and lower stratosphere, leading to a weak equatorward shift of the tropospheric jet (Fig. 3.4(i)). Moreover, synoptic waves shift the tropospheric jet poleward, with a deep acceleration on the jet's poleward flank from the surface to the stratosphere (Fig. 3.4(l)). This deep acceleration (i.e., a stratospheric control from synoptic waves) was also reported in KP04, and it can be partly understood by the downward control theory as a barotropic zonal wind response above the level of the eddy forcing (Haynes et al. (1991)). In addition, the zonal wind response to synoptic eddy forcing is partially canceled by the planetary eddy response in the troposphere, and leaves a net poleward shift of the tropospheric jet as observed in the full model (i.e., $FM_F - FM_C$).

What are the implications of the results above for our understanding of the tropospheric response to stratospheric ozone depletion-like cooling? If the

DCWEF mechanism were the dominant mechanism at play, the equatorward jet shift associated with the planetary wave-induced residual circulations in Fig. 3.4(i) is expected to be maintained or amplified by a positive synoptic eddy feedback. However, the stronger poleward tropospheric jet shift due to the synoptic eddy forcing in Fig. 3.4(l) suggests that the mechanism of DCWEF is not dominant.

To explicitly test the role of the synoptic eddy feedback, a synoptic-wave model would be the first choice. Ideally, in the synoptic-wave model, the planetary wave forcing due to ozone depletion-like cooling can be specified similarly to ZM_P, and these specified zonal flow anomalies represent the effects of downward control via altered residual circulation. In the meanwhile, only the zonal mean and the synoptic eddies are resolved in this synoptic-wave model. This setup not only allows the synoptic eddy feedback to dominate in the troposphere, but also eliminates the nonlinear eddy-eddy interaction between planetary waves and synoptic waves. However, as shown in Fig. 3.5, the control run of this synoptic-wave model (SM_C, see Table 3.1 for details) is characterized with a double-jet structure, which is different from the single-jet structure in the full model FM_C and the zonally symmetric model ZM_C. This indicates that the synoptic-wave model is practically inapproriate for the explicit test of DCWEF in this current study. This also suggests that the nonlinear eddy-eddy interaction between planetary waves and synoptic waves, which is missing in SM_C, is critical to maintain the reasonable jet structure, despite a small contribution from planetary waves to the zonal mean eddy forcing.

Instead, an additional experiment, denoted by FM_P in Table 3.1, is performed in the full model. In this experiment, we specify anomalous zonal mean

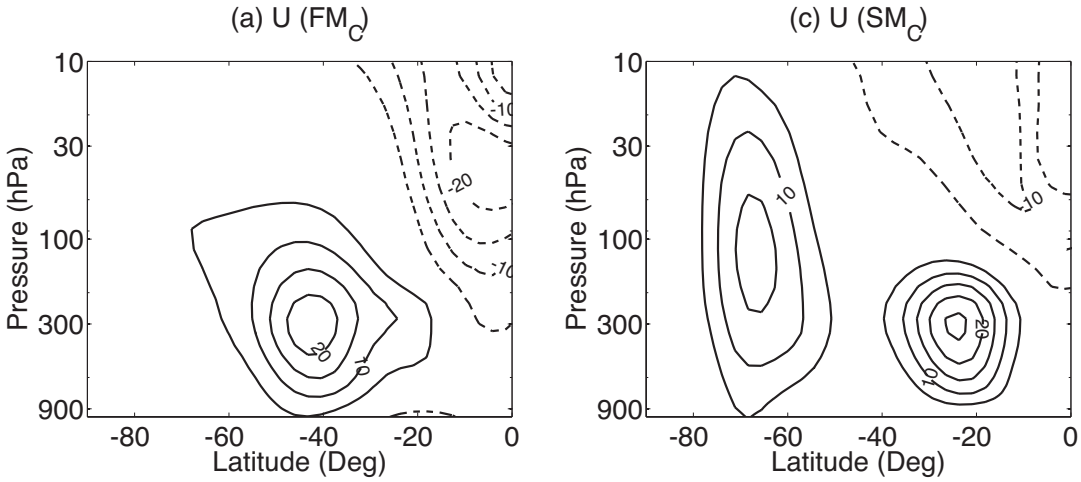

Figure 3.5: Comparison on the climatology of zonal mean zonal winds (unit: $\mathrm{m\,sec^{-1}}$) between: (a) in the full model (FM_C); and (b) in the synoptic-wave model (SM_C). See Table 3.1 for details. On the implications of the results — keeping the zonal mean planetary wave drags and resolving the synoptic eddies in SM_C produce a very different jet structure as compared with the control run FM_C. This indicates the synoptic eddy-planetary eddy interaction (e.g., wave breaking) is crucial in maintaining the mean jet structure.

planetary wave forcing extracted as the difference between the perturbed run and the control run, $FM_F - FM_C$. Compared with the full model simulation in FM_F, only the zonal mean forcings of anomalous planetary eddies are included in this experiment, and therefore the majority of the eddy-eddy interactions with planetary waves are excluded. Note that the resolved planetary waves in FM_P can also be affected by the specifed zonal mean planetary wave forcing (i.e. $FM_F - FM_C$). This limitation counts as an important factor to explain the simulated stratospheric zonal wind difference between FM_F and FM_P (compare Fig. 3.3(f) and Fig. 3.6(c)). In comparison with the corresponding zonally symmetric model simulation in ZM_P, the specified anomalous planetary wave forcing is identical, but the synoptic eddy feedback is allowed in FM_P. Therefore, this can be approximately thought of as a direct simulation of the DCWEF response to

the anomalous planetary wave drag induced by ozone depletion-like radiative cooling.

The results are displayed in Fig. 3.6. Generally speaking, the response to anomalous planetary wave forcing in the full model resembles its counterpart in the zonally symmetric model (cf. Fig. 3.6(a)(b)(c) with Fig. 3.4(g)(h)(i)), except for the meridional structure of the DJF stratospheric zonal wind anomaly seen in Fig. 3.6(c). This is not surprising as these stratospheric changes are primarily driven by specified anomalous planetary wave drag. Moreover, even in the presence of synoptic eddy feedbacks, the anomalous planetary eddy forcing produces a weak equatorward shift in the tropospheric jet (cf. Fig. 3.6(c)), in contrast to the poleward movement of the tropospheric jet in response to polar stratospheric cooling in the full model (cf. Fig. 3.3(f)). Therefore, this directly supports that DCWEF is not the dominant mechanism in generating the poleward tropospheric jet shift in response to stratospheric ozone depletion-like cooling in this full model. This is consistent with the implication deduced from Fig. 3.4(i) and Fig. 3.4(l), characterized with opposite tropospheric jet shifts under the influences of planetary waves versus synoptic waves.

As noted in Section 3.1, Sun et al. (2014) found that only the composite from the years with delayed SFW has a prominent tropospheric circulation response. The tropospheric response associated with the delayed SFW could be attributed to either an anomalous temperature cooling in the lowermost stratosphere (see their Fig. 10) that impacts synoptic eddies directly (i.e. the first mechanism in Fig. 3.1(a)), or the changes in the planetary eddies (see their Fig. 11) that further influence the synoptic eddies via nonlinear eddy-eddy interaction (i.e. the third mechanism in Fig. 3.1(c)). However, given that the stratospheric cooling tends

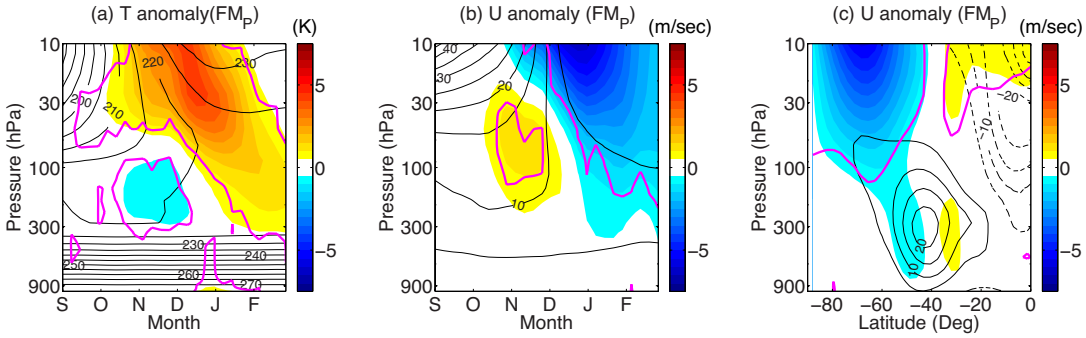

Figure 3.6: As the bottom row of Fig. 3.3, but for specified anomalous zonal mean planetary wave forcing extracted as the difference between the perturbed run (with ozone depletion-like cooling) and the control run in the full model (i.e. $FM_F - FM_C$). See the text in Section 3.4 for details.

to propagate upward in the summer by only imposing the radiative forcing with eddies being fixed, as shown in Fig. 4(d), we argue that the summertime temperature cooling in the lowermost stratosphere (cf. Fig. 3.3(d), similar to Fig. 10 in Sun et al. (2014)) is unlikely caused by a pure downward advection of the imposed radiative cooling, but with the aids of altered eddies (cf. Fig. 3.4(g)(j)).

Therefore, we propose that the tropospheric circulation response is less likely contributed solely by a direct impact on the synoptic eddies from the imposed radiative perturbation. A synthetic influence from both the imposed radiative cooling and resultant planetary wave changes onto the synoptic eddies in the upper troposphere and lower stratosphere that triggers the tropospheric circulation response remains possible in this model simulation, but the importance of eddies, in particular the planetary eddies at the altitude of the imposed radiative cooling, seem to be crucial in the downward influence. To further confirm the dominance of the altered planetary eddies and subsequent nonlinear eddy-eddy interaction in Fig. 3.1(c), one could investigate the planetary wave struc-

ture changes in response to the imposed perturbation, as in this mechanism, planetary waves can communicate between the stratosphere and troposphere by wave propagation (e.g., Chen and Robinson, 1992) or reflection (e.g., Shaw et al., 2010).

3.5 Conclusions

We have examined transient atmospheric responses to stratospheric ozone depletion-like cooling in the idealized model of KP04. Despite its simplicity, the idealized model captures approximately the pattern and timing of the austral summertime circulation trends associated with radiative cooling (McLandress et al., 2010, Lin and Fu, 2013, Thompson et al., 2011). In contrast to the unrealistic long persistence of the tropospheric response in KP04, the tropospheric persistence in our simulation is reasonable as compared with observations. This was also noted in Kushner and Polvani (2006) that the seasonal cycle of T_{eq} in the stratosphere helps to reduce the unrealistically long persistence in the tropospheric response seen in KP04.

By extending the method of KP04 and Domeisen et al. (2013) to different wave numbers in the context of the seasonal cycle, we are able to separate the mechanisms of transient atmospheric responses to stratospheric radiative cooling in a zonally symmetric model. While the initial responses, mostly in the stratosphere, are caused by a direct adjustment to thermal forcing, the subsequent downward migration of signals is primarily driven by eddy forcing. We found that the synoptic eddies shift the tropospheric jet poleward, as in the full model with ozone depletion-like radiative cooling, against a weak equatorward

tendency of the jet associated with the planetary wave forcing. This indicates that the equatorward tropospheric jet shift due to the planetary wave-induced residual circulations, arguably a result of stratospheric eddy-zonal flow interaction, is not maintained by a positive synoptic eddy feedback in the troposphere. This contrasts to the mechanism of planetary eddy-induced residual circulation in the tropospheric response to stratospheric forcing (Song and Robinson, 2004, Thompson et al., 2006). However, the stratospheric forcing considered by Song and Robinson (2004) and Thompson et al. (2006) is associated with major stratospheric variability, rather than an external forcing like the stratospheric ozone depletion-like cooling imposed in this study.

Furthermore, the tropospheric circulation response associated with the polar stratospheric cooling, consistent with the delayed SFW composite in Sun et al. (2014), could be contributed from either a direct impact from the imposed radiative perturbation to synoptic eddies in the upper troposphere and lower stratosphere, or an indirect impact from the radiative perturbation via resultant planetary wave changes and subsequent nonlinear eddy-eddy interaction, or a synthetic impact from both. However, the temperature decrease in the lowermost stratosphere, the key in the mechanism for a direct impact to the synoptic eddies, is unlikely a pure advection of the imposed radiative cooling from higher altitudes, but the aids from altered eddies are critical. Therefore, this mechanism for a direct impact alone is hardly to fully explain the downward influence of the polar stratospheric cooling towards tropospheric circulation response, and the role of the planetary eddies seem to be crucial. In this mechanism, resultant planetary wave changes from imposed radiative perturbation propagate from the stratosphere to the troposphere through wave propagation (e.g., Chen and Robinson, 1992) or reflection (e.g., Shaw et al., 2010), which in

turn impacts synoptic eddies through nonlinear eddy-eddy interactions.

While our simulations compare well with other studies with more sophisticated GCMs and realistic ozone depletion (McLandress et al., 2010, Orr et al., 2013), our results may be limited by the simplicity of the idealized model. One key simplification of the model is the flat lower boundary, and therefore the planetary waves are solely generated by nonlinear wave-wave interactions (Scinocca and Haynes, 1998). In reality, planetary waves in the SH may be additionally generated by land-sea contrast or topography. This is partly reflected in that the zero wind line in the summertime stratospheric wind is higher (or wave drag is weaker) in the idealized model as compared with the observations (cf. Figs. 3.3(c) and 3.3(f)). Meanwhile, the onset date for the stratospheric final warming is generally too late in the current climate models (e.g., Wilcox and Charlton-Perez, 2013). It would be interesting to explore the sensitivities of the dynamical mechanisms with respect to the model biases in the summer stratosphere relative to the observed climate.

Table 3.1: Summary of numerical experiments. 'Resolved' denotes the component is resolved in the model. 'Specified' denotes the component is specified using Eq. (A.4) and the simulation indicated in the bracket. See the text in Section 3.3 and appendix for details.

Model	Exps	Description	Zonal means	planetary eddies	synoptic eddies	ozone loss
Full	FM_C	control	resolved	resolved	resolved	no
Model	FM_F	forced ozone depletion	resolved	resolved	resolved	yes
	FM_P	planetary eddy	resolved	resolved plus specified anomaly ($FM_F - FM_C$)	resolved	no
Zonally Symmetric	ZM_C	control	resolved	specified (FM_C)	specified (FM_C)	no
Model	ZM_F	total forcing	resolved	specified (FM_F)	specified (FM_F)	yes
	ZM_Q	radiative cooling	resolved	specified (FM_C)	specified (FM_C)	yes
	ZM_P	planetary eddy	resolved	specified (FM_F)	specified (FM_C)	no
	ZM_S	synoptic eddy	resolved	specified (FM_C)	specified (FM_F)	no
Synoptic Wave Model	SM_C	control	resolved	specified (FM_C)	resolved	no

CHAPTER 4

STRATOSPHERE-TROPOSPHERE EXCHANGE OF OZONE

4.1 Introduction

Observational diagnostic (Olsen et al., 2013) suggests an increased downward stratosphere-troposphere exchange (STE) of ozone from the stratosphere to the troposphere. This increase is also widely reported in climate models (e.g. Hess et al., 2015), and is predicted to continue in the future (Collins et al., 2003, Hegglin and Shepherd, 2009). On the one hand, the increase of ozone STE will modify the tropospheric oxidative capacity (e.g. Kentarchos and Roelofs, 2003), influencing the lifetime of methane (Fiore, 2002) as well as the chemical cycles of other tropospheric pollutants. On the other hand, deep intrusion of stratospheric ozone, on some occasions, have been shown to greatly increase the surface ozone concentration and therefore becomes important for surface air quality prediction and control (Lin et al., 2012).

Quantification of STE on the global (or hemispheric) scale can be inferred either from the residual circulation (Holton, 1990) or from the lowermost stratosphere (LMS) mass budget (Appenzeller et al., 1996). A number of studies found that the annual global ozone STE is within the range of 400-600 Tg/year in both observations and chemistry transport models (CTMs) (e.g. Gettelman et al., 1997, Olsen et al., 2004, Hsu and Prather, 2005, Stevenson et al., 2006, Hsu and Prather, 2009). However, detailed spatial distribution of ozone STE is not as well quantified, in spite of the fact that ozone STE over different regions may have different tropospheric impacts via different transport mechanisms. Exchange across the higher-latitude tropopause may transport ozone along the

low isentropic surfaces that intersect the ground, resulting in a deep intrusion of stratospheric ozone into the planetary boundary layer (PBL) and with resultant air quality concerns. By contrast, ozone STE over lower latitudes limits its influence mostly to the middle and upper troposphere, and it is more likely to impact tropospheric oxidative capacity (Kentarchos and Roelofs, 2003). In this study, an isentropic STE diagnostic (Nakamura, 2007) is applied to a model simulation. This diagnostic extends Appenzeller et al. (1996)'s approach into individual isentropic layer in the LMS, such that the location of STE along different isentropic surfaces can be differentiated meridionally.

The seasonal cycle of ozone STE, particularly the timing of the maximum in STE, is also important, as the ozone STE may have a longer and more widespread influence in winter due to the longer photochemical timescale of ozone during the winter months (Liang et al., 2009). In the observations, there is a springtime maximum in the tropospheric column ozone in the Northern Hemisphere (NH) midlatitudes, particularly on the western edge of Europe (Monks, 2000). This maximum may be explained partly by the large ozone STE during spring months (Liang et al., 2009). A springtime ozone maximum is consistent with the seasonality of stratospheric fallout of radioactive debris from nuclear bomb tests (e.g Fry et al., 1960) as well as with the spring maximum in the extratropical downwelling air mass flux (e.g. Appenzeller et al., 1996, Gettelman et al., 1997). However, trajectory analysis (Wernli and Bourqui, 2002, James et al., 2003, Skerlak et al., 2014) find that deep stratospheric intrusions, that effectively transport ozone to the surface, maximize in winter. A springtime maximum also contrasts with various studies of tracer advection with reanalysis winds (Chen, 1995, Haynes and Shuckburgh, 2000b, Nakamura, 2007), where the largest isentropic air mass transport is associated with monsoonal

circulations during the summer months above the 340-K isentropic surface.

The widespread discrepancies in when and where ozone enters the troposphere may be attributed to the variety of mechanisms controlling STE and the lack of understanding about these mechanisms. It is well known that the Brewer-Dobson Circulation (BDC) (Brewer, 1949, Dobson, 1956) provides as a global contraint on the strength of ozone STE. The acceleration of BDC simulated in many models (e.g. Garcia and Randel, 2008, Chen and Sun, 2011, Yang et al., 2014) is consistent with the predicted increase of annual mean global mean ozone STE in a future climate. As to the temporal and spatial variability in the ozone STE, a number of studies have linked the occurence of STE to the tropopause folding or cut-off cyclones (Danielsen, 1968, Reed and Vicek, 1969, Holton et al., 1995), the summer monsoon or deep convection over continents (Tang et al., 2011), and large-scale wave breaking over the Pacific and Atlantic oceans leading to isentropic mixing within selected layers (Chen, 1995, Postel and Hitchman, 1999, Jing et al., 2004, Nakamura, 2007).

Although numerous mechanisms for STE have been analyzed, their relative contributions to the ozone STE variability have not been elucidated. Schoeberl (2004) divided the air mass STE flux into a diabatic flux across isentropic surfaces, representing the slow but long-term transport by the BDC, and a residual adiabatic flux along isentropic surfaces, representing the more effective and transient exchange mostly due to the isentropic mixing. However, constrained by the framework of Appenzeller et al. (1996), Schoeberl (2004) can only partition the STE budget on the hemispheric scale. By contrast, the isentropic STE diagnostic used in this study partitions the STE flux along different isentropic surfaces into components associated with either the differential diabatic heat-

ing or the isentropic mixing, and gives the meridional distribution about each component.

In addition, in terms of the interannual variability of ozone STE, rapid sulfate aerosol increase in the stratosphere by volcanic eruption has been shown to significantly decrease the ozone STE, primarily by reducing the stratospheric ozone concentration (Tang et al., 2013). Quasi-biennial Oscillation (QBO) in the stratosphere also controls the STE via modifying the strength of BDC (e.g. Neu et al., 2014). On the other hand, tropospheric climate forcing, like the El-Nino and Southern Oscillation (ENSO), tends to accelerate the BDC during its warm phase, and hence strengthen the STE of ozone (e.g. Yang et al., 2014, Neu et al., 2014). It is of equivalent importance to understand how strong these internal climate variability, either from troposphere or stratosphere, can affect the interannual behaviors of ozone STE, and, by which mechanism(s), the ozone STE is being affected.

A 19-year control simulation from the specified dynamics (SD) version of the Whole Atmosphere Community Climate Model (WACCM) and a 30-year control simulation from the SD version of the Canadian Middle Atmosphere Model (CMAM) are used in this study to examine the meridional distribution of ozone STE as well as to understand the mechanisms that affect the ozone STE. Section 4.2 specifically introduces the isentropic STE diagnostic that quantifies the STE flux along individual isentropic surface and partition the flux into components associated with different physical processes. Details about the model (SD-WACCM) is introduced in Section 4.3.1. Quantification of the spatiotemporal variability of ozone STE is given in Section 4.3. Potential dynamical mechanisms for this STE are discussed in Section 4.4. All discussions on the seaonality

of ozone STE and the beneath mechanisms are briefly examined and compared in the other model of SD-CMAM in Section 4.5. Section 4.6 gives a preliminary analysis on the interannual variability of ozone STE in both models. Lastly, conclusions are drawn in Section 4.7.

4.2 Isentropic STE diagnostic

4.2.1 Quantification of STE

Prior diagnostic of STE (Appenzeller et al., 1996) have considered the air mass budget over the entire LMS. As illustrated in Fig. 4.1(a), the rate of air mass change within the grey shaded LMS ($\partial m_{LMS}/\partial t$) can be calculated as the balance between the inward air mass flux across the upper boundary of 380-K isentropic surface (F_{380K}) and the outward flux across the lateral boundary of the tropopause, which is the targeted air mas STE flux (F_{STE}). Equivalently, the diagnosed air mass STE flux following the mass continuity in the LMS reads (if we assume no flux is crossing the poles and flux from the troposphere to the stratosphere is defined as positive)

$$F_{STE} = \frac{\partial m_{LMS}}{\partial t} + F_{380K} \tag{4.1}$$

where $F_{380K} = \left\langle \sigma \dot{\theta} \right\rangle_{380K}$ (Schoeberl, 2004), representing the hemispheically-integrated (indicated by the bracket) diabatic air mass flux across the 380-K isentropic surface. Specifically, σ is the isentropic mass density, $-g^{-1}\frac{\partial p}{\partial \theta}$, p is the pressure, θ is the isentropic temperature, and $\dot{\theta}$ denotes the diabatic heating rate. Note that it has been shown in many studies (e.g. Appenzeller et al., 1996) that both the inward flux across 380-K isentropic surface and the outward flux

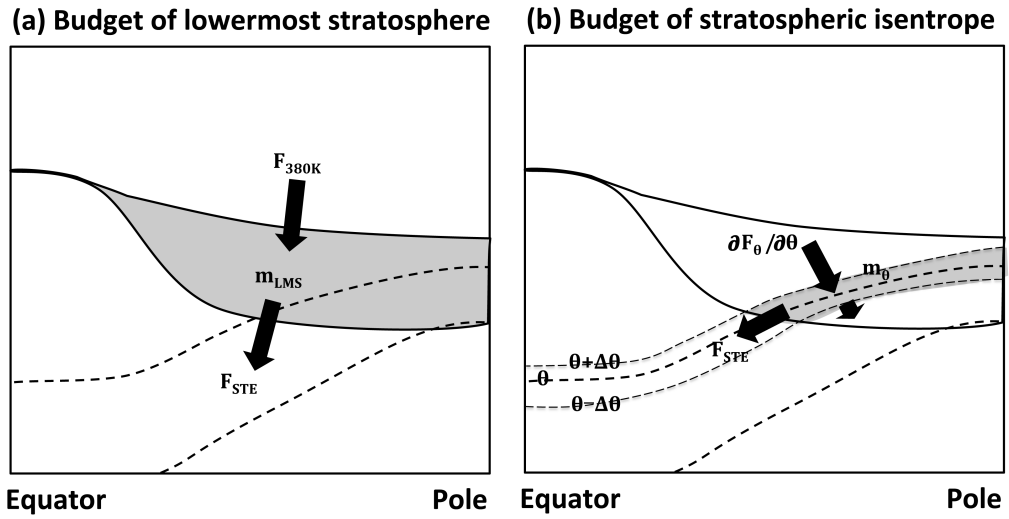

Figure 4.1: Schematic showing air mass budget: (a) in the lowermost stratosphere (LMS); (b) at each isentropic layer. Details are referred to the text in Section 4.2.1.

at the tropopause are dominantly from the stratosphere to the tropopshere, as depicted in Fig. 4.1. However, these fluxes are negative in Eq. 4.1.

In this LMS bulk methodology, the quantification of STE is contrained on the hemispheric scale, and therefore provides no information on the spatial distribution of STE. The latter is important so as to distinguish STE over high latitudes from its counterpart over low latitudes with distinct chemical and climate impacts as noted in the Section 4.1.

By contrast, Nakamura (2007) divides the LMS into stacks of slim slabs enclosed by adjacent isentropic surfaces (see their Figure 2). For each 'isentropic' slab (e.g. see the grey shaded region in Fig. 4.1(b)), the mass continuity still holds. Hence, the air mass tendency within the isentropic slab ($\frac{\partial m_\theta}{\partial t}$) is produced from the balance between the diabatic flux divergence ($\frac{\partial F_\theta}{\partial \theta}$) in the quasi-vertical

direction and the air mass STE flux across the lateral boundary (F_{STE}).

$$F_{STE} = \frac{\partial m_\theta}{\partial t} + \frac{\partial F_\theta}{\partial \theta} \tag{4.2}$$

$$F_\theta = M(\dot{\theta}) \tag{4.3}$$

where the operator $M(\cdot)$ defines the density-weighted integral about the quantity in parenthesis over the stratospheric region on the isentropic surface θ (see details in Nakamura (1995)). Note that Eq. (4.2) is is derived by assuming that the distance between adjacent isentropic surfaces is infinitesimal. and all terms are in the unit of $\mathrm{kg\,sec^{-1}\,K^{-1}}$. The hemispherically-integrated air mass STE in Eq. (4.1) can be regained by integrating up the 'isentropic' STE in Eq. (4.2) for all the isentropic slabs within the LMS.

Spatially, this 'isentropic' STE flux in each slab covers only a short meridional range on the tropopause between the two adjacent isntropic surfaces. However, as the isentropic temperature increases monotonically with height and higher isentropic surfaces normally intersect with the tropopause at lower latitudes, a vertically aligned series of diagnosed isentropic STE from high isentropic surfaces to low isentropic surfaces approximately renders the meridional distribution of STE from low latitudes to high latitudes. Note that although this isentropic STE diagnostic quantifies the meridional distribution of STE, the diagnosed fluxes do not map strictly onto the Eulerian latitudes, but the tropopause-contour averaged 'equivalent laltitudes' instead (see details in Nakamura (1995)). Similar to Nakamura (2007), we divide the LMS by isentropic surfaces ranging from 280 K to 380 K, with an evenly spaced 4-K interval. The seasonal averaged locations of selective isentropic surfaces are given as the dahsed contours in Fig. 4.2. Details of the discretization of this approach are given in Appendix B.

For ozone STE along isentropic surface θ (F^{χ}_{STE}), the equivalence of Eq. (4.2) is

$$F^{\chi}_{STE} = \frac{\partial M(\chi)}{\partial t} + \frac{\partial M(\chi\dot{\theta})}{\partial \theta} - M(\dot{\chi}) \tag{4.4}$$

where χ is the mass mixing ratio of ozone in the unit of kg/kg, and $\dot{\chi}$ denotes the chemical source of ozone.

4.2.2 Dynamic partition

The isentropic STE diagnostic not only quantifies the spatial distribution of STE, but provides a framework to dynamically partition the STE into components associated with different physical processes, facilitating our understanding on the mechanisms that control the STE.

For a tropopause defined as a potential vorticity (PV) surface (see Section 4.3.1), Nakamura (1995) documented that the isentropic air mass STE flux, an inflow/outflow across the PV isopleth Q, is strictly associated with the PV tendency ($\dot{q}$)

$$F_{STE} = -\frac{\partial M(\dot{q})}{\partial q}\bigg|_{q=Q} \tag{4.5}$$

There are numerous physical processes contributing to the PV tendency, but two are of primary importance.

$$\dot{q} \approx \dot{q}_s + \dot{q}_\kappa \tag{4.6}$$

Here, the $\dot{q}_s$ denotes the component of PV source associated with the differential diabatic heating with $\dot{q}_s \approx \frac{q}{\sigma}\frac{\partial(\sigma\dot{\theta})}{\partial\theta}$ (e.g. Holton, 2004), and $\dot{q}_\kappa$ denotes the component of PV source associated the isentropic eddy mixing with $\dot{q}_\kappa = \kappa\nabla^2 q$

(Nakamura, 2007). κ is the eddy diffusivity coefficient. Thus, we examine the mechanisms influencing the STE in this study by decomposing the diagnosed air mass STE in Eq. (4.2) into two components: the one associated with the differential diabatic heating (F_{dia} hereafter), and the other associated with the isentropic eddy mixing (F_{mix} hereafter).

$$F_{STE} = F_{dia} + F_{mix} = -\left.\frac{\partial M(\dot{q}_s)}{\partial q}\right|_{q=Q} - \left.\frac{\partial M(\dot{q}_\kappa)}{\partial q}\right|_{q=Q} \tag{4.7}$$

Given the difficulty in determining the eddy diffusivity coefficient κ, we compute F_{dia} directly, and attain F_{mix} indirectly as a residue from $F_{mix} = F_{STE} - F_{dia}$. We propose that this residue flux is dominantly contributed by the isentropic eddy mixing, as this residue flux resembles the STE flux F_{mix} roughly estimated by $\dot{q}_\kappa = \kappa\nabla^2 q$ with an assumed constant κ (not shown). Notice that, both the diabatic flux at the 380-K isentropic surface F_{380K} (or any isentropic surface) and F^{χ}_{dia} are associated with diabatic processes. However, they are essentially different, since the diabatic flux F_{380K} transports ozone across and perpendicular to the isentropic surface, while F^{χ}_{dia} transports ozone along the isentropic surface, but it is caused by the diabatic heating.

For ozone STE flux, Eq. (4.7) is rewritten as

$$F^{\chi}_{STE} = F^{\chi}_{dia} + F^{\chi}_{mix} = -\left.\frac{\partial M(\chi\dot{q}_s)}{\partial q}\right|_{q=Q} - \left.\frac{\partial M(\chi\dot{q}_\kappa)}{\partial q}\right|_{q=Q} \tag{4.8}$$

4.3 Seasonality of ozone STE

In this section, by applying the isentropic STE diagnostic, we examine a case study to illustrate the implementation of the method of diagnosing STE described above. The diagnosed climatology of ozone STE, including its hemispheric budget and meridional distribution, is then given using a 19-year dataset from the specified dynamics version of the Whole Atmosphere Community Climate Model (SD-WACCM). In this section, we focus on the seasonal variability of ozone STE.

4.3.1 Dataset

The data analyzed here is from a control simulation of the specified dynamics version of the Whole Atmosphere Community Climate Model (SD-WACCM) from 1990 to 2009, nudged by the Modern-Era Retrospective Analysis for Research and Application (MERRA) reanalysis at every model time step (Tang et al., 2013). We discard the first year of 1990 to avoid any spin-impacts, and thus analyze a 19-year climatology of diagnosed ozone STE. The SD-WACCM is a high-top climate-chemistry interactive model with an approximate horizontal resolution of 1.9 degrees longitude by 2.5 degrees latitude, and vertically ranges from the surface to a top lid near 140 km. There are 88 unevenly spaced hybrid layers and the vertical resolution near the tropopause is about 1 km. Details about the physical packages and nudging in the SD-WACCM are referred to Tang et al. (2013, and references therein).

Before implementing the isentropic STE diagnostic, the model data on the

hybrid coordinate is vertically interpolated onto the designated isentropic coordinate from 280 K to 380 K, following Edouard et al. (1997). Note that the isentropic STE diagnostic can be applied to any form of dataset (reanalysis and/or model simulation), once the diabatic heating $\dot{\theta}$ is known. However, in practice, the diagnostic further requires sufficient vertical resolution near the tropopause levels to constrain the errors induced by the interpolation. We argue that the current approximate 1 km resolution near the tropopause in the SD-WACCM is sufficient, as the diagnosed ozone STE converges as the density of interpolated isentropic layers increases.

As STE occurs on the tropopause, it is also interesting to investigate the sensitivity of diagnosed STE to the choice of tropopause. Here, we adopt four different types of tropopause definitions.

- **O3S:** O3S is ozone not produced by NOx catalyzed tropospheric photochemical reactions (see Hess and Zbinden, 2013). We define the O3S = 120ppbv as the O3S tropopause.
- **e90:** e90 is an idealized tracer in the model, which has an e-folding decay time of 90 days. The e90 tropopause is defined by the e90 concentration, at which 80% percent of the atmospheric mass is below. Here, the threshold is about $7.53 \times 10^{-30}\,\mathrm{mol\,mol^{-1}}$ of the e90 mixing ratio, and the molecular weight of e90 is set to 48 so as to mimic ozone (Prather et al., 2011).
- **WMO:** definition adopted by the World Meteorological Organization (WMO) using the lapse rate $\frac{dT}{dz} = -2\mathrm{K\,km^{-1}}$.
- **PV:** Ertel potential vorticity. Given its sharp vertical gradient across the tropopause, here we define the PV surface of 3 PVU as the PV tropopause.

Figure 4.2 gives the location of the different tropopauses as defined by these definitions in the SD-WACCM simulation in each of four seasons. Overall, all tropopauses are spatially close to each other, and there is a similar seasonal cycle in terms of tropopause height for all four tropopause defintions. However, there are also noticeable differences among these defintions. For example, the e90 tropopause is generally lower than others, paticularly over the deep tropics.

For the first three tropopause definitions, the tropopause pressure p_{trop} is output directly from the model simulation. Alternatively, PV, as diagnosed in isentropic coordinates, identifies the PV tropopause (see details in Appendix B).

4.3.2 Case study

Hsu and Prather (2005) identified a strong ozone STE event over the eastern Pacific in mid-March 2001 by considering the tropospheric ozone budget. Here, we seek to replicate this case study using the isentropic STE diagnostic, based on the SD-WACCM simulation. Figure 4.3(a) gives the NH longitude-latitude map of the 330-K isentropic surface on the day of March 16th, 2001 at 000 UTC. The stratosphere is characterized by relatively higher concentration of ozone (warm colors) poleward of the WMO tropopause (black solid contour), while the troposphere is demarcated by the lower ozone concentrations (cool colors). There is a noticeable anti-cyclonic wave breaking feature near 140°W (the eastern Pacific Ocean), transporting ozone-abundant stratospheric air into the troposphere with the aid of strong equatorward winds (vectors) near 160°W.

Depicted in an equivalent latitude-pressure cross section, Fig. 4.3(b) gives the corresponding isentropic STE flux of ozone (colors) across the WMO

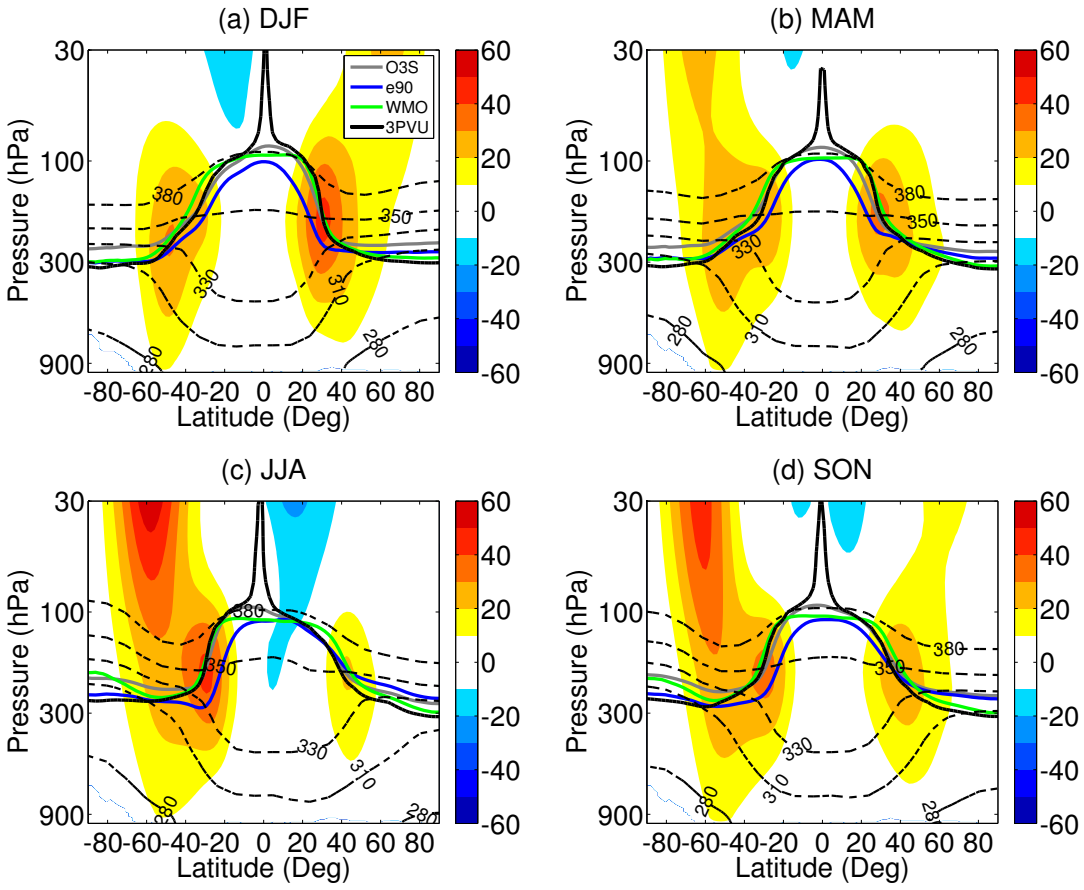

Figure 4.2: Latitude-altitude pattern of different tropopauses in four seasons: (a) DJF, (b) MAM, (c) JJA, and (d) SON. In each subplot, the tropopauses are shown as solid lines, and are separately defined by: stratospheric ozone (grey), idealized tracer e90 (blue), WMO standard (green), and 3 PVU (black), see Section **??** for details. The corresponding seasonal averaged zonal mean zonal winds (unit: m/sec) are displayed in shades and selected isentropic surfaces (K) are denoted as the dashed lines.

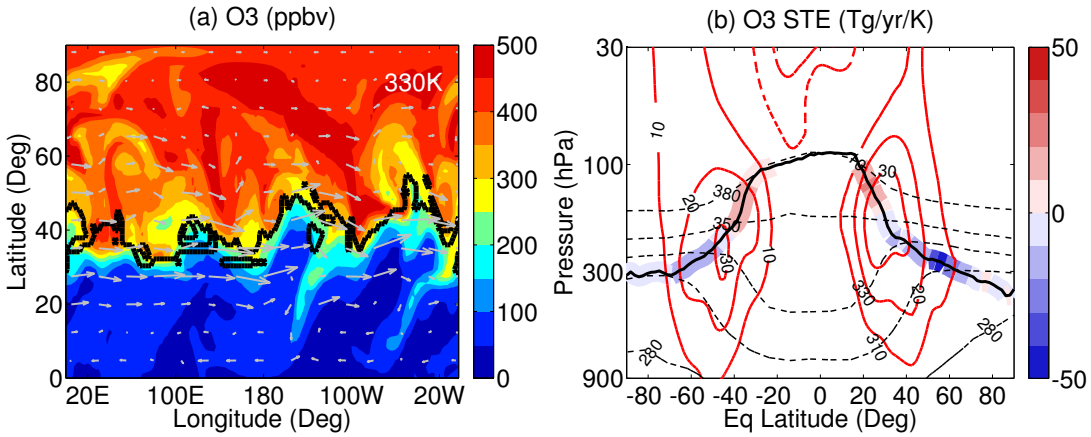

Figure 4.3: An ozone STE event at 000 UTC on the day of March 16th, 2001 in the SD-WACCM control simulation: (a) a snapshot on the 330-K isentropic surface showing the longitude-latitude distribution of ozone mixing ratio (colors, unit: ppbv), and wind (vectors). The WMO tropopause is denoted as the bold solid black line. (b) latitudinal distribution of the diagnosed isentropic ozone STE flux (color blocks) across the the WMO tropopause (solid black line). Important isentropic surfaces (dashed lines) and zonal mean zonal wind (red contours) are marked similar to Fig. 4.2.

tropopause (black solid contour) following Eq. (4.4). There is a clear spatial distribution about the diagnosed ozone STE, in terms of both isentropic surfaces (dashed lines) and equivalent latitudes. Specifically, troposphere-to-stratosphere (upward hereafter) transport of ozone occurs on higher isentropic surfaces (lower equivalent latitudes) equatorward of the tropospheric jets (red contours), while stratosphere-to-troposphere (downward hereafter) transport of ozone occurs on lower isentropic surfaces (higher equivalent latitudes) mostly poleward of the jets.

To further explain the upward (downward) ozone STE over high (low) isentropic surfaces in Fig. 4.3(b), the ozone budget in Eq. (4.4) is examined on two isentropic surfaces (330 K and 370 K) in the NH. In a similar fashion as Fig.

4.3(a), the longitude-latitude distribution of diabatic ozone flux ($\chi\sigma\dot{\theta}$) across the 330-K and 370-K isentropic surface is given in Fig. 4.4(a) and (b) respectively. Both isentropic surfaces show a predominantly downward diabatic ozone flux in the stratosphere, except, at 370 K, where robust upwelling is centered at 180° longitude corresponding to the daytime radiative heating of stratospheric ozone. Similar to the LMS bulk methodology, we find that the isentropic ozone STE is largely determined by the vertical divergence of diabatic ozone flux $\chi\sigma\dot{\theta}$ (not shown). Therefore, on the 330-K isentropic surface (Fig. 4.4(c)), the vertical ozone convergences (blue) in the stratosphere is balanced by a horizontal divergence resulting in the transport of ozone from the stratosphere to the troposphere. In contrast, on the 370-K isentropic surface (Fig. 4.4(d)), the vertical divergence of diabatic ozone flux in the stratosphere (red) is balanced by a horizontal convergence, transporting ozone from the troposphere to the stratosphere.

4.3.3 Hemispherically-integrated ozone STE

We further evaluate the isentropic STE diagnostic developed here by comparing the corresponding 19-year climatology of hemispherically-integrated ozone STE with that calculated using the LMS bulk methodology (see Fig. 4.1(a)). Here, the hemispherically-integrated ozone STE is attained by integrating all diagnosed isentropic STE flux from the 280-K isentropic surface to the 380-K isentropic surface, as suggested in Section 4.2.1.

Table 4.1 shows the climatological mean of hemispheric (and global) integrated ozone STE flux across all four defined tropopauses. The climatological

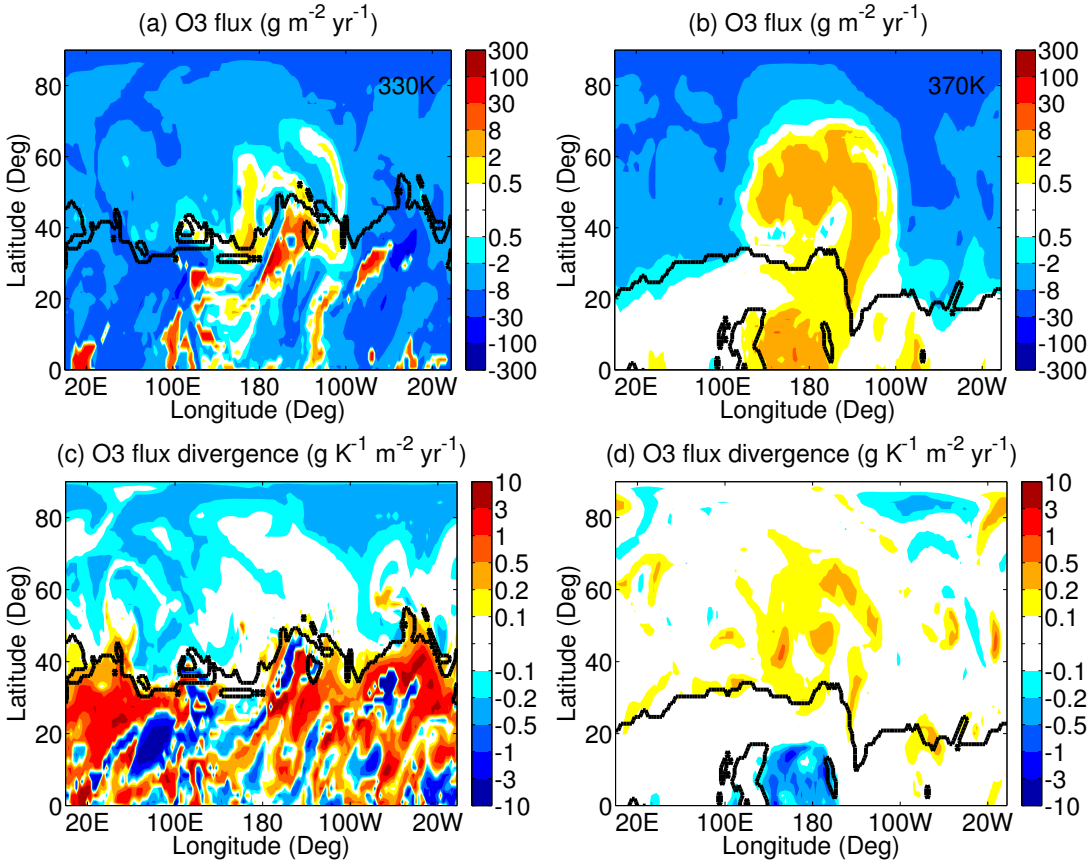

Figure 4.4: Examination on the isentropic STE diagnostic for the ozone STE event in Fig. 4.3: colors denote the diabatic ozone flux ($\chi\sigma\dot{\theta}$) in (a)(b), and the diabatic ozone flux divergence ($\frac{\partial\chi\sigma\dot{\theta}}{\partial\theta}$) in (c)(d) at (a)(c) the 330-K and (b)(d) 370-K isentropic surface. Other marks are following the same fashion as in Fig. 4.3(a). Details are referred to text in Section 4.3.2.

mean global ozone STE is in the range of 410-450 Tg/yr, and is generally consistent with the reported numbers in many other studies using the LMS bulk methodolgy (e.g. Gettelman et al., 1997, Hegglin and Shepherd, 2009). The ozone STE in the NH is 50-60 Tg/yr larger than its counterpart in the southern hemisphere (SH), highlighting the importance of eddy forcing in driving the stratospheric overworld residual circulation (Olsen et al., 2003). In addition, the diagnosed hemispheric or global integrated annually averaged ozone STE flux is relatively insensitive to the choice of tropopause definition.

Table 4.1: Hemispheric and global budgets for ozone STE (unit: Tg/ yr) across four tropopauses. See section 4.3.3 for details.

O3 STE (Tg/yr)	O3S	e90	WMO	3PVU
NH	−240 ± 20	−241 ± 19	−242 ± 19	−256 ± 20
SH	−178 ± 20	−190 ± 19	−176 ± 19	−191 ± 19
Global	−419 ± 36	−431 ± 35	−419 ± 34	−448 ± 35

As to temporal evolution, the climatological seasonal cycle of hemispherically-integrated ozone STE in the NH and in the SH are given in Fig. 4.5(a) and (b) respectively. The ozone STE is downward in both hemispheres throughout the year. In the NH, there is a noticeable peak in downward ozone STE in late spring and early summer, which is also consistent with the timing documented in many other studies using the LMS bulk methodlogy (e.g. Hegglin and Shepherd, 2009). In contrast, little seasonality is found in the SH. The seasonality of hemispherically-integrated ozone STE is not sensitive to the choice of tropopause defintion either, although the e90 tropopause exhibits a substantially larger seasonality in the NH. This insensivity to tropopause definition also applies to the remaining discussions of this paper. Therefore, we only use the 3 PVU tropopause definition hereafter, as it relates most directly to the dynamic partitioning.

4.3.4 Meridional distribution of ozone STE

As noted in Section 4.2.1, one of the important merits of the isentropic diagnostic used in this paper is that it gives the approximate meridional distribution of

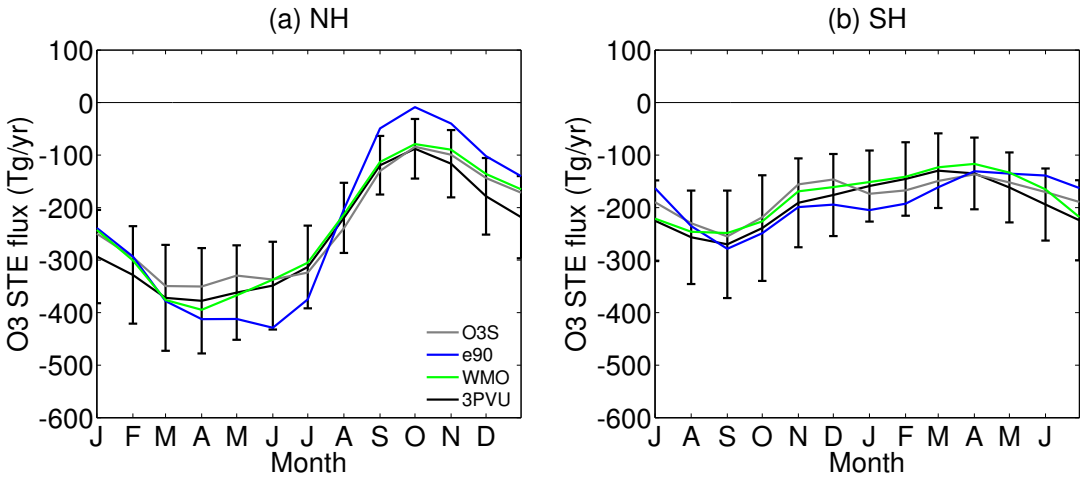

Figure 4.5: Seasonal cycle of the hemispherically-integrated ozone STE flux (unit: Tg/yr) across four different tropopauses (colored with the same fashion as in Fig. 4.2) in the: (a) northern hemisphere (NH); (b) southern hemisphere (SH). Error bars are depicted as the one standard deviation deduced from the 19-year time series. Note that the abscissa in the SH is shifted forward by 6 months, and troposphere-to-stratosphere flux is defined as positive.

ozone STE flux, with exchange across the higher isentropic surfaces corresponding to lower latitude exchange and exchange aross the lower isentropic surfaces corresponding to higher latitude exchange.

Figure 4.6 gives the climatological seasonal cycle of the isentropic ozone STE flux from the 280-K isentropic surface to the 380-K isentropic surface corresponding to a meridional STE distribution from the poles to the lower latitudes in subtropics. Upward ozone STE fluxes (warm colors) are found on the higher isentropic surfaces (lower latitudes), whereas downward ozone STE fluxes (cool colors) are found on the lower isentropic surfaces (higher latitudes). The boundary separating these two zones is situated near the core of the tropospheric jets (contours). More importantly, the maximum downward ozone

STE flux is found on the poleward flank of the jets on the lower isentropic surfaces, and the maximum moves seasonally with the jets, towards higher isentropic surfaces in summer and towards lower isentropic surfaces in winter (not necessarily equatorward or poleward in latitude, as individual isentropic surface moves seasonally and intersects with the tropopause at different location as well, see Fig. 4.2). All these features indicate an intimate connection between the variability in ozone STE and the variability in tropospheric jet, which will be further discussed in Section 4.4. Moreover, we again note that the NH ozone STE (Fig. 4.6(a)) is generally larger than its SH counterpart (Fig. 4.6(b)) on almost all isentropic surfaces throughout the year. Furthermore, the meridional distribution of diagnosed isentropic ozone STE is insensitive to the choice of tropopause defintion (not shown).

To explicitly interpret the seasonal variability in ozone STE over different meridional regions and to relate this to their distinct impacts on tropospheric chemistry and surface air quality, we further group the diagnosed isentropic ozone STE into four bins as indicated by the dashed isentropic surfaces in Fig. 4.2.

- **350 K-380 K:** subtropical region;
- **330 K-350 K:** core of the jet region;
- **310 K-330 K:** poleward flank of the jet region;
- **280 K-310 K:** polar region.

The ozone STE flux within each bin is obtained by integrating the isentropic ozone STE flux from the lowest isentropic surface to the highest isentropic surface in the bin. The seasonal cycles of the ozone STE within each bin are given

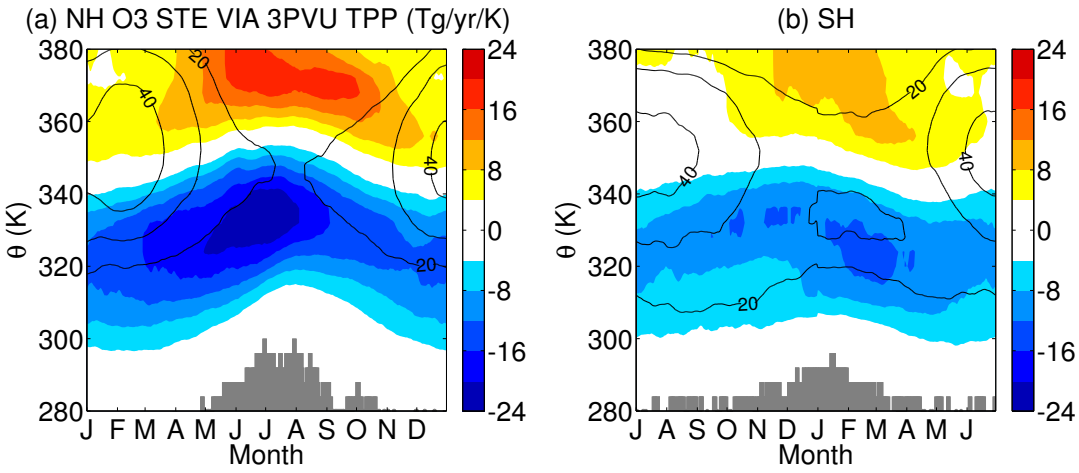

Figure 4.6: Seasonal cycle of the isentropic ozone STE flux (troposphere-to-stratosphere transport as positive) that transports ozone along isentropic surfaces across the 3 PVU tropopause (color, unit: Tg/yr/K) and the zonal mean zonal wind on this tropopause (contours, unit: m/sec) in (a) the NH, and (b) the SH. Grey shaded regions identify those lower isentropic surfaces that do not intersect with the tropopause, so that the corresponding isentropic ozone STE strictly equals zero. The results are shown after a 7-day box-moving smooth.

in Fig. 4.7. Consistent with the findings in Fig. 4.6, the subtropical region (350K-380K) is characterized by a prominent upward ozone STE flux, whereas the downward ozone STE fluxes prevail in other regions. In the NH, the upward ozone STE flux over the subtropical region maximizes in summer, while the maximum downward ozone STE flux gradually shifts from summer on lower isentropic surfaces to winter on higher isentropic surfaces. In the SH, the seasonal variability is less.

More importantly, from Fig. 4.7, we propose that the discrepancy with respect to the seasonality of ozone STE reported in previous studies (see Section 4.1) can be partly attributed to the different meridional regions of exchange analyzed in different papers. On the hemispheric scale, a late spring-early summer

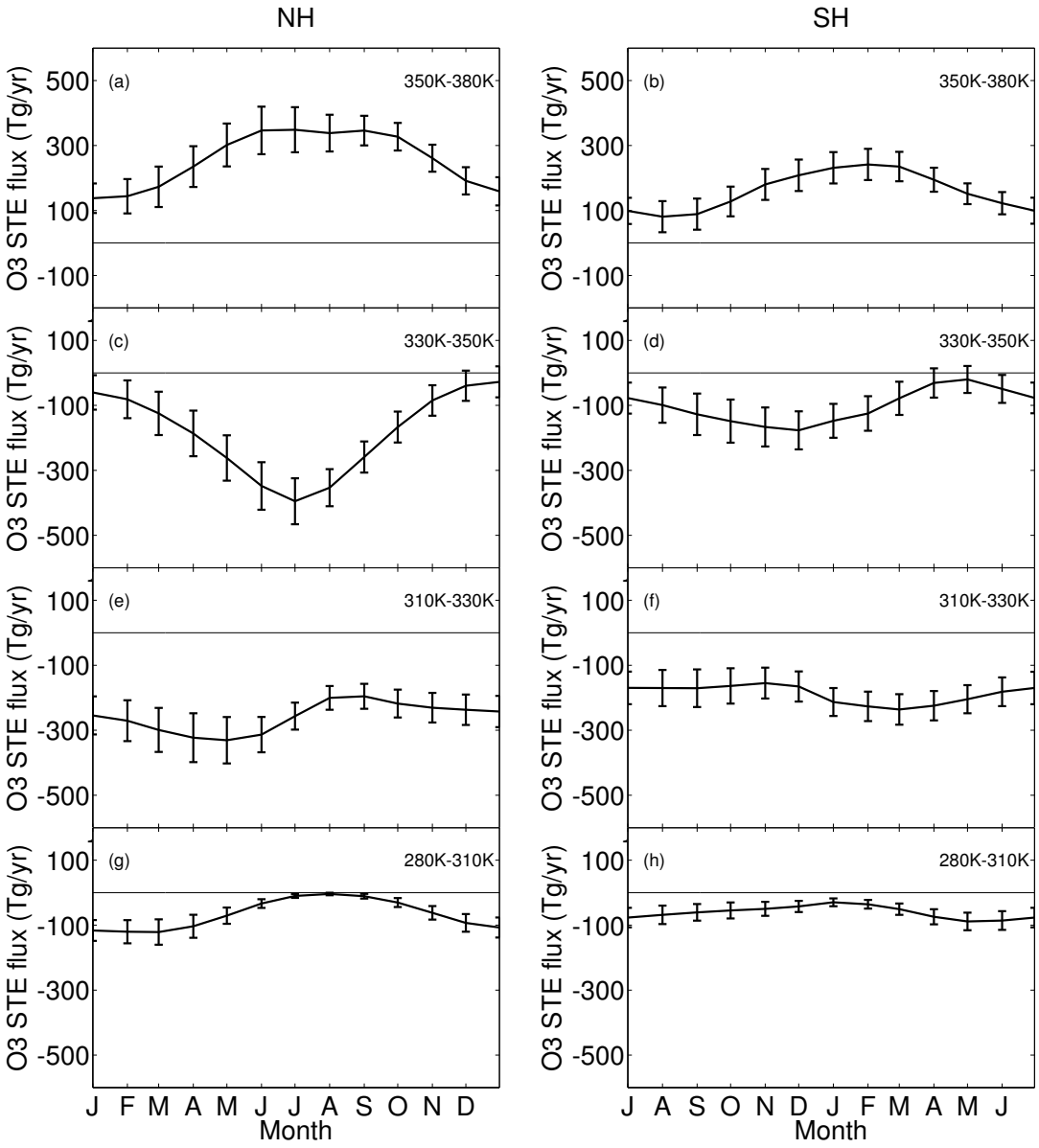

Figure 4.7: Similar to Fig. 4.5, but for: (a)(b) subtropical region with high isentropic surfaces, 350 K-380 K; (c)(d) core of the jet region with 330 K-350 K ranged isentropic surfaces; (e)(f) poleward flank of the jet region with 310 K-330 K ranged isentropic surfaces; and (g)(h) polar region with low isentropic surfaces, 280 K-310 K. See details in Section 4.3.4. Only ozone STE flux across the 3PVU tropopause is shown.

maximum (see Fig. 4.5) has been widely reported in the NH (e.g. Gettelman et al., 1997, Hsu and Prather, 2005). This maximum can be mostly attributed to the downward ozone STE flux over the region near the poleward flank of the NH tropospheric jet (310K-330K) that also peaks in the late spring (see Fig. 4.7(e)). By contrast, there is a large cancellation between the upward ozone STE over the subtropical region (350K-380K) and the downward ozone STE over the core of the jet region (330 K- 350 K) which both peak during NH summer, contributing relatively less to the hemispherically-integrated ozone STE. In the meantime, the wintertime maximum in ozone STE on the lower isentropic surfaces (280 K - 310 K, and see Fig. 4.7(g)) corresponds to the deep intrusion of stratospheric ozone reported in James et al. (2003), Skerlak et al. (2014). This component of the downward ozone STE flux, albeit relatively small, occurs on isentropic surfaces that intersect the surface of the Earth and can thus extend into the PBL with a lag of 2-3 months (Liang et al., 2009, see their Fig. 5). The summertime maximum of ozone (or air mass) STE above the 340-K isentropic surface (e.g. Nakamura, 2007), on the other hand, is related to the downward ozone STE near the core of the jet region (330 K - 350 K), where the moonsoonal circulations (or deep convection over continents) and associated large-scale isentropic mixing tend to play important roles (Chen, 1995, Tang et al., 2011).

4.4 Mechanisms

In order to understand why ozone STE exhibits such a spatial distribution, we partition the STE flux into a diffusive term and and a diabatic term (see Section 4.2.2). By doing this, we relate the diagnosed STE flux to different physi-

Table 4.2: On the hemispheric and global scale, a dynamic partition that separates the ozone STE (unit: Tg/ yr) across 3 PVU tropopause (F^{χ}_{STE}) into a flux component associated with diabatic heating (F^{χ}_{dia}) and a flux component associated with isentropic mixing (F^{χ}_{mix}) , see Eq. 4.8.

(unit: Tg/yr)	F^{χ}_{dia}	F^{χ}_{mix}	F^{χ}_{STE}
NH	713 ± 20	−969 ± 32	−256 ± 20
SH	681 ± 18	−872 ± 31	−191 ± 19
Global	1394 ± 34	−1841 ± 56	−448 ± 35

cal/chemical processes that result in PV sources/sinks, and hence to the mechanisms that control the spatiotemporal behaviors of ozone STE.

4.4.1 Partition

By applying Eq. 4.8, we can separate the ozone STE flux into the component associated with diabatic PV source F^{χ}_{dia} and the component associated with isentropic PV mixing F^{χ}_{mix}. For the climatological mean annual hemispheric budget, Table 4.2 shows that both components are about 3-4 times larger in magnitude than the net ozone STE flux. F^{χ}_{dia} contributes to a large upward ozone STE flux while F^{χ}_{mix} contributes to a large downward ozone STE flux. There is a large cancellation between the two, but the F^{χ}_{mix} is slightly larger than the F^{χ}_{dia}, yielding the downward net ozone STE flux (F^{χ}_{STE}).

The spatial distribution of patitioned components of ozone STE is further illustrated in Fig. 4.8. F^{χ}_{dia} is upward on all isentropic surfaces, while the F^{χ}_{mix} is predominantly downward on all isentropic surfaces outside the (sub)tropics.

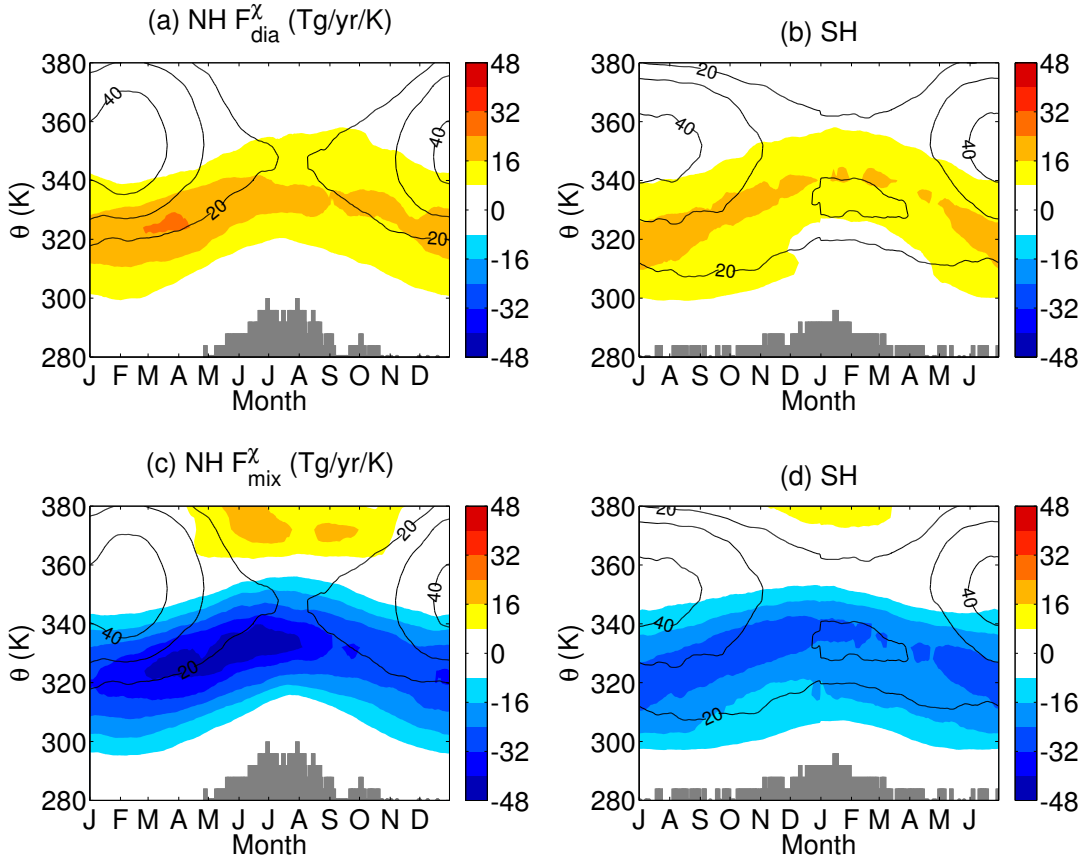

Figure 4.8: Similar to Fig. 4.6, but for the dynamic partition of ozone STE across 3 PVU tropopause, which: (a)(b) show the ozone STE component associated with diabatic PV source (F^{χ}_{dia}); and (c)(d) show the ozone STE component associated with isentropic PV mixing (F^{χ}_{mix}).

Both components maximize at the poleward edge of the tropospheric jets (contours), and the maxima shift seasonally with the jets. More importantly, the large cancellation between F^{χ}_{dia} and F^{χ}_{mix} reported on the hemispheric scale (see Table 4.2) occurs on almost all isentropic surfaces. As F^{χ}_{mix} is slightly larger than F^{χ}_{dia}, the net ozone STE flux is relatively smaller, and with a spatiotemporal pattern similar to that of F^{χ}_{mix} (compare Fig. 4.8(c)(d) with Fig. 4.6).

4.4.2 Isentropic PV mixing

Physically, the isentropic mixing tends to induce PV sink and thus to move the tropopause boundary upward, leading to transport of the stratospheric air into the troposphere. To explicitly document how the isentropic eddy mixing impacts the spatiotemporal variability of isentropic ozone STE, the extent of isentropic mixing is independently quantified by the effective diffusivity based solely on the distortion of PV (Nakamura, 1995, Haynes and Shuckburgh, 2000b).

Figure 4.9 shows a clear connection between the air mass STE component associated with isentropic PV mixing F_{mix} and the effective diffusivity $\tilde{\kappa}_{eff}$. In general, strong F_{mix} occurs over the region where mixing is robust, indicated by the high effective diffusivity $\tilde{\kappa}_{eff}$. In particular, the strong shear instability and resultant wave breaking near the edge of jets provide a favorable condition for isentropic mixing, contributing to the relatively large F_{mix} on both sides of the jets (either upward in subtropics or downward in extratropics). In contrast, within the jet cores near the 350-K isentropic surface, isentropic mixing is largely suppressed due to the strong zonal winds and resultant reduced wave breaking. Consequently, relatively small air mass STE flux is induced in the regions with the limited isentropic mixing.

Moreover, the zonal wind, isentropic mixing and F_{mix} variablity show similar seasonal variation. As the tropospheric jet tends to weaken and shrinks in size from winter to summer, its poleward flank shifts towards higher isentropic surfaces. Consequently, the maximum of downward F_{mix} simultaneously shifts towards higher isentropic surfaces, following the movement of the jet edge and zone of strong isentropic mixing (high $\tilde{\kappa}_{eff}$). Note that the flux F_{mix} maximum

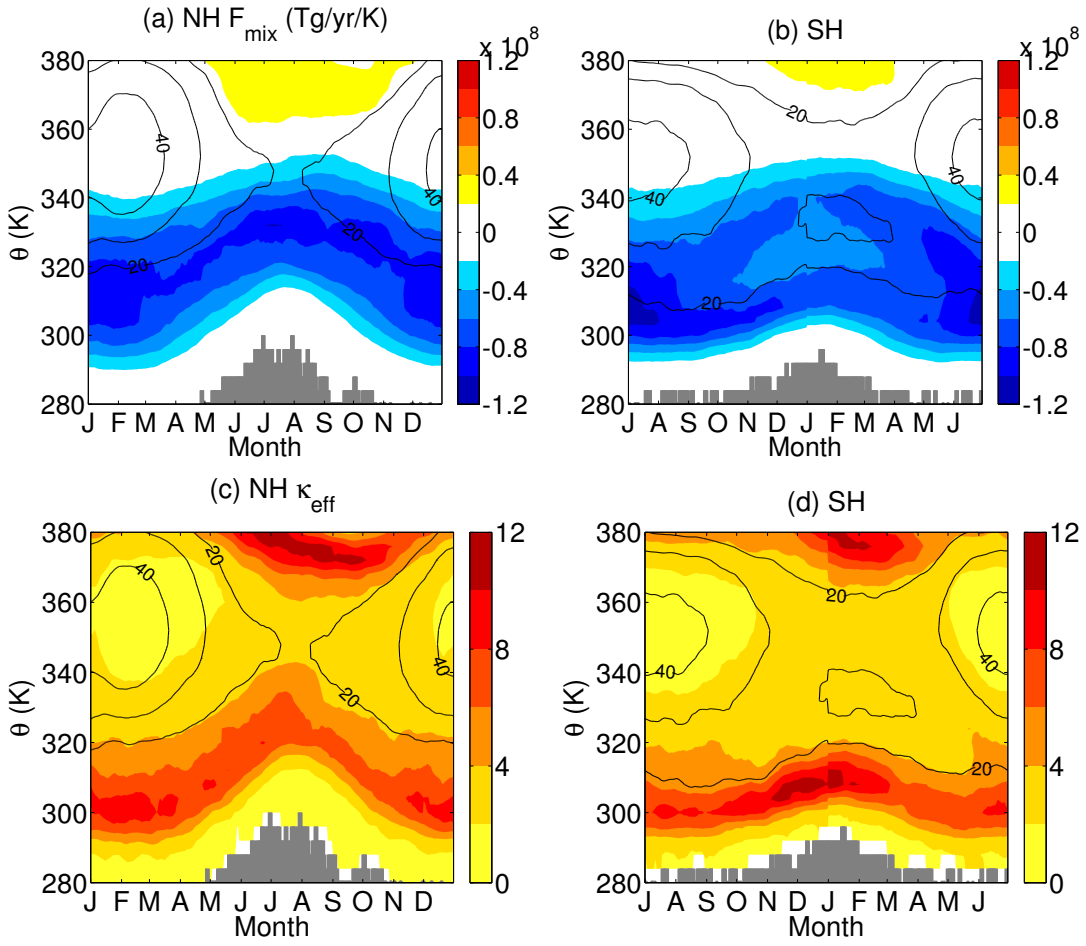

Figure 4.9: Similar to Fig. 4.6, but for (a)(b) the air mass STE component associated with isentropic PV mixing (F_{mix}, unit: Tg/yr/K), and (c)(d) extent of the isentropic mixing represented by the effective diffusivity $\tilde{\kappa}_{eff}$.

at 310 K-330 K is equatorward of the effective diffusivity $\tilde{\kappa}_{eff}$ maximum at 300 K-320 K throughout the year. This can be attributed to the relatively large cross-tropopause air mass gradient near the 320-K isentropic surface (not shown), as the flux F_{mix} is a convolution of the flow rate (i.e. extent of isentropic mixing, denoted by the effective diffusivity $\tilde{\kappa}_{eff}$) and this air mass gradient.

As ozone is a chemical tracer, the seasonal cyle of ozone STE flux is addition-

ally affected by the seasonal variability in ozone mixing ratio at the tropopause. If the ozone mixing ratio is annually constant, the ozone can be regarded as a fixed portion of any air parcel, and thus the ozone STE flux F^{χ}_{mix} is expected to vary seasonally in phase with the air mass STE flux F_{mix}. Although Fig. 4.10 shows that, in terms of hemispheric budget, the seasonal cycle of F^{χ}_{mix} (Fig.4.10(c)(d), solid) resembles that of the F^{mix} (Fig.4.10(a)(b), dashed), it lags by a few months. This lag is plausibly influenced by the seasonal varibility in ozone mixing ratio at the tropopause (Fig.4.10(e)(f), dot-dashed), which maximizes in May in the NH (Thouret et al., 2006) and is later than the air mass STE flux F_{mix} maximum in January. Both the tropical ozone chemical production/destruction and the dynamic transport in the stratophere can contribute to this seasonal variation in ozone mixing ratio at the tropopause, but the relaive importance of each process remains unclear.

4.4.3 Diabatic PV source

To further interpret the diagnosed upward STE associated with the diabatic PV source, we use the fact that the air mass STE associated with diabatic PV source F_{dia} is approximately propotional to the diabatic PV source ($\dot{q}_S$) at the tropopause, and the two quantities should be in the same sign in the NH (and opposite in the SH).

$$F_{dia} \propto \dot{q}_S|_{q=Q} \tag{4.9}$$

Therefore, the direction of F_{dia} is determined by the sign of the diabatic PV source ($\dot{q}_S$) at the tropopause Q.

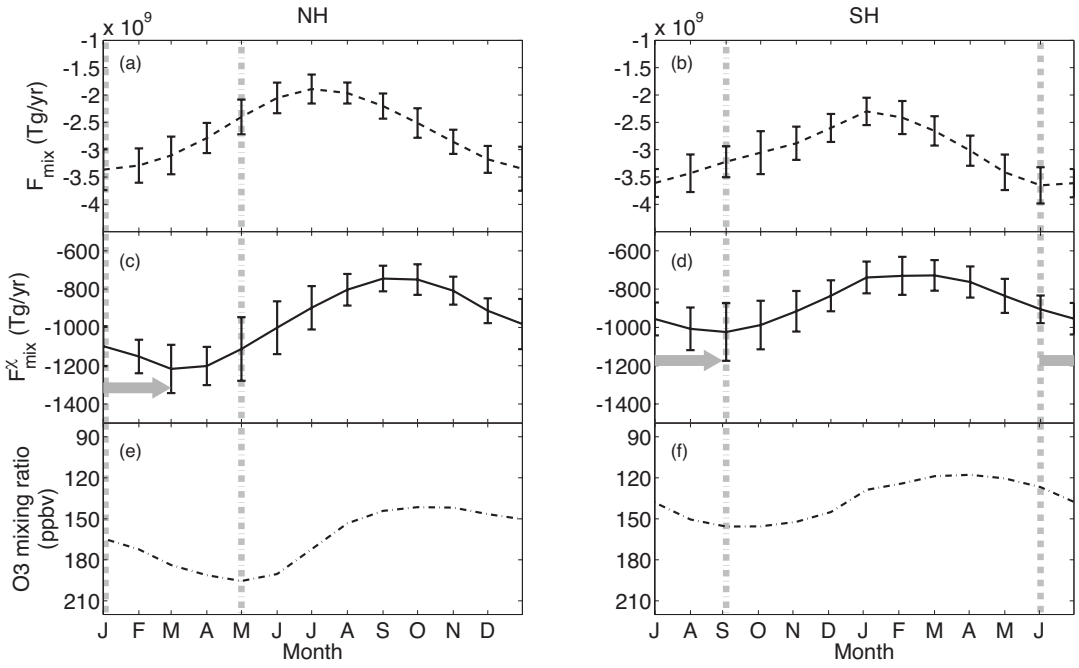

Figure 4.10: Similar to Fig. 4.5, but for (a)(b) the hemispherically-integrated air mass STE component associated with isentropic PV mixing F_{mix} (dashed, unit: Tg/yr); (c)(d) the ozone STE component associated with isentropic PV mixing F^{χ}_{mix} (solid, unit: Tg/yr); and (e)(f) the ozone mixing ratio at the 3 PVU tropopause χ (dot-dashed, unit: ppbv). Vertically aligned grey dashed lines denote the month with maximum F_{mix}, and grey dot-dashed lines denote the month with maximum χ. Grey arrows denote the temporal shift of F_{mix} maximum to F^{χ}_{mix} maximum, probably due to the seasonal cycle of χ. Note that the y-axis for ozone mixing ratio is reversed.

Fig. 4.11 shows the isentropic air mass STE flux associated with the diabatic PV source (F_{dia}, top) and the corresponding diabatic PV source ($\dot{q}_S$, bottom) at the $Q = 3$ PVU tropopause. Note that the sign of $\dot{q}_S$ has been flipped in the SH. Clearly, the upward F_{dia} can be understood as a decrease in tropopause height due to the differential diabatic heating (e.g. $\dot{q}_S > 0$ at the tropopause in the NH), engulfing the 'original' tropospheric air into the expanding stratosphere. More interestingly, the maxima of both F_{dia} and $\dot{q}_S$ exhibit an arch-type shape,

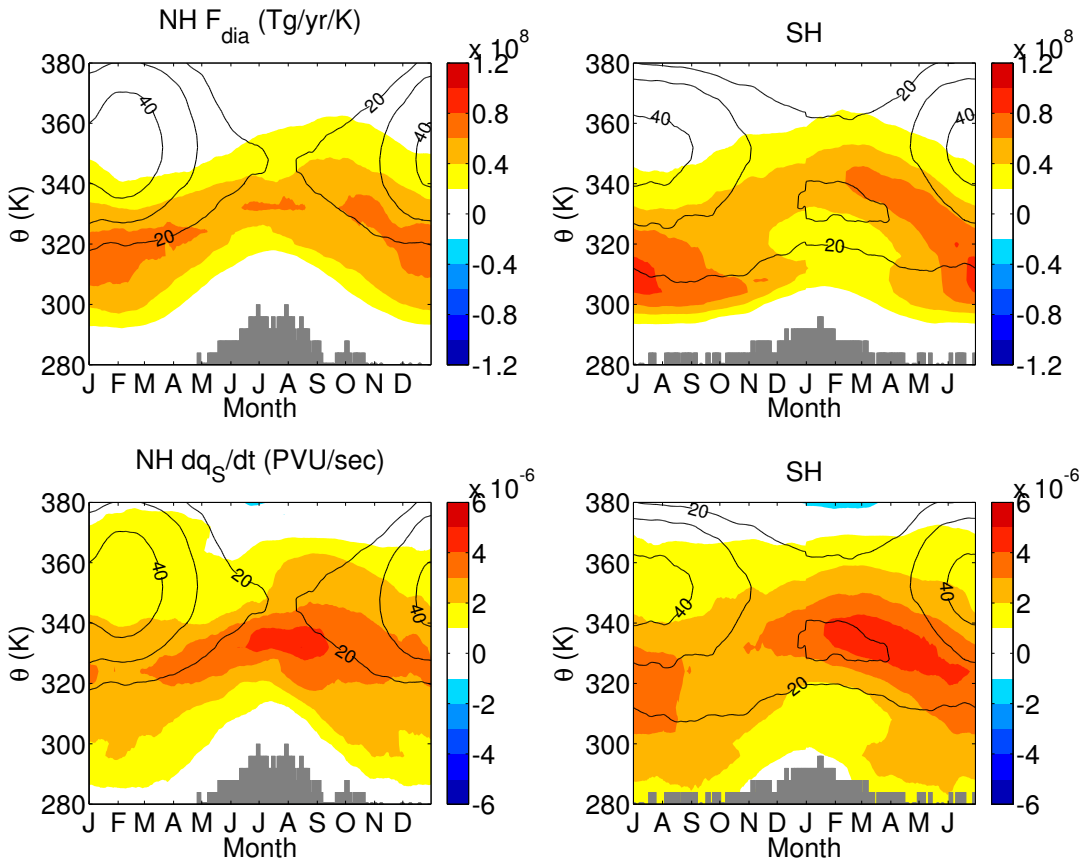

Figure 4.11: Similar to Fig. 4.9, but for: (a)(b) the air mass STE component associated with diabatic PV source (F_{dia}, unit: Tg/yr/K), and (c)(d) diabatic PV source ($\dot{q}_S$, unit: PVU/sec) on the 3 PVU tropopause.

as they follow the seasonal movement of the poleward jet flanks (contours). This suggests that the spatial distribution of F_{dia} is highly affected by the spatial variability in $\dot{q}_S$. Similar to F^{χ}_{mix}, the seasonality in F^{χ}_{dia} is additionally affected by the seasonal cycle of ozone mixing ratio χ at the tropopause (not shown here).

4.5 Model comparison

To further confirm that the diagnosed STE flux in Section 4.3 is physically robust, we replicate the above analyses in another model, which is the SD version of the Canadian Middle Atmosphere Model (CMAM). We expect the diagnosed ozone STE exhibits a similar spatiotemporal pattern in the CMAM comparing with that in the WACCM, as the overall decription on the climate system should be consistent among different models. However, differences are inevitable, as individual model is distinguishable from the others in either the dynamic core discretization or the parameterization on specific physical and chemical processes.

Table 4.3 briefly summarizes the most noticeable differences between the SD-WACCM model and the SD-CMAM model. Although both models are high-top models in this new generation of climate models, the CMAM model is relatively coarser in the horizontal resolution. The number of vertical layers is less in the SD-CMAM model, but the vertical resoltion near the tropopause level (about 1 km) is close to that in the SD-WACCM. In addition, the nudging scheme is different between the two models, as the SD-WACCM uses the MERRA reanalysis data whereas the SD-CMAM uses the ERA-interim reanalysis data. As the CMAM model, in practice, enables solely the diagnostic of ozone STE across the PV tropopause, we only compare the results from the two different models on the 3 PVU tropopause in this section.

The hemispherically-integrated ozone STE is first examined in Fig. 4.12. In the NH, the diagnosed ozone STE in the SD-CMAM (gray) displays a general consistent seasonal cycle as that in the SD-WACCM (black), with the maximum

Table 4.3: Comparison between the specified dynamics (SD) version of the Whole Atmosphere Community Climate Model (WACCM) and the SD version of the Canadian Middle Atmosphere Model. Here, MERRA is the reanlysis data from the Modern-Era Retrospective Analysis for Research and Application, and ERA-interim is the reanalysis data from the European Center for Medium-Range Weather Forecasts.

Models	Horizontal	Vertical	Lid	Duration	Nudging
SD-WACCM	$1.5° \times 2°$	88	0.0006 hPa	1991-2009	MERRA
SD-CMAM	$3.75° \times 4°$	63	0.07 hPa	1981-2010	ERA-interim

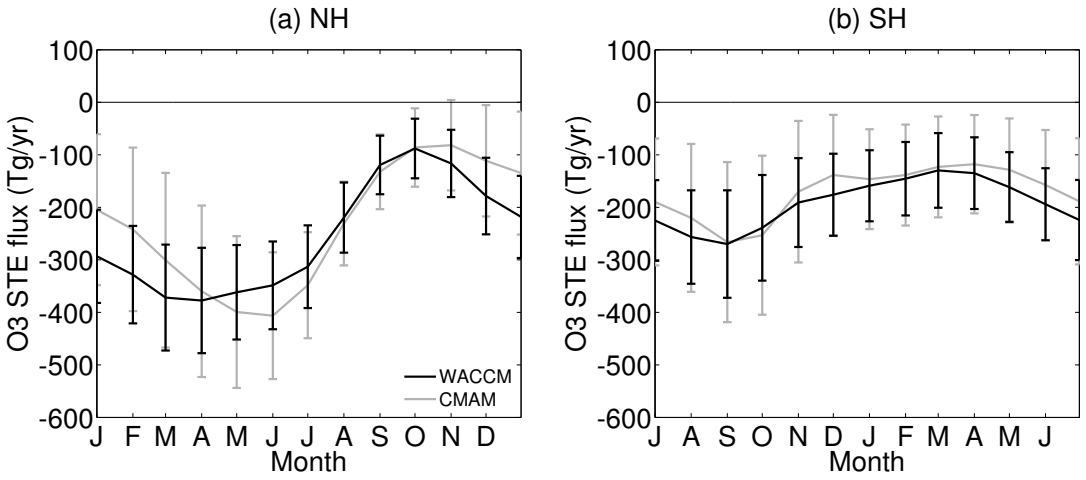

Figure 4.12: Similar to Fig. 4.5, but the results from anaylsis on the CMAM dataset are shown in the gray lines.

downward ozone STE also occurs in late spring and early summer (only 1-2 month(s) later than that in the SD-WACCM). The difference in the SH between the two models is even less. These results suggest that, at the hemispheric scale, the isentropic diagnostic is isensitive to different choices of model, and thus becomes extremely useful to render robust physical diagnosis on the ozone STE flux.

The meridional distribution of ozone STE is further compared in Fig. 4.13, the general spatiotemporal patterns are consistent as expected. Both models diagnose an upward ozone STE on the higher isentropic surfaces in (sub)tropics and an downward ozone STE on the lower isentropic surface in extratropics., with an arch-type maximum of downward ozone STE situating on the poleward flank of the tropospheric jets and moving seasonally with the jets. However, the diagnosed ozone STE is relatively smaller in magnitude in the SD-CMAM, particularly over the region equatorward of the 320-K isentropic surface in the NH (also seen in Fig. 4.14(a)). Moreover, the late-spring early-summer maximum of downward ozone STE over the region on the poleward flank of the tropospheric jets shifts towards lower isentropic surface (poleward) from 330 K in the SD-WACCM to 320 K in the SD-CMAM.

The differences (i.e. CMAM - WACCM) are further explicitly examined in Fig. 4.14. Consistent with Fig. 4.13, the NH net ozone STE reduces in magnitude almost everywhere in the CMAM model, as less upward flux (negative anomalies) in (sub)tropics and less downward flux (positive anomalies) in extratropics is diagnosed. Such a reduction is less discernible in the SH. By dynamically partitioning the net ozone STE flux into a diabatic component of F^{χ}_{dia} and a diffusive component of F^{χ}_{mix}, the difference of diagnosed ozone STE between the two models (see Fig. 4.14(a)(b)) is dominantly attributed to the diffusive component F^{χ}_{mix}, which is highly associated with the extent of isentropic mixng near the tropopause. In particular, the relatively lower horizontal resolution in the CMAM model can numerically contribute to the relatively suppressed isentropic mixing and resultant reduced isentropic ozone STE.

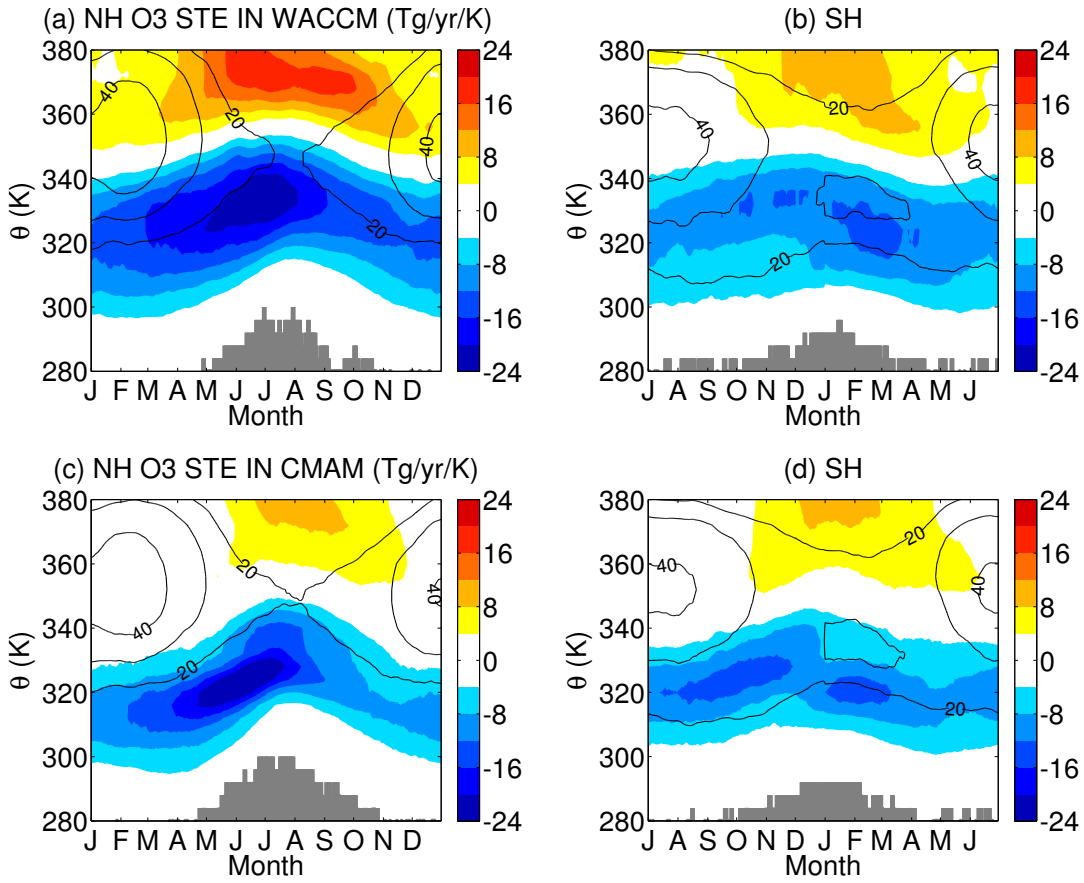

Figure 4.13: Similar to Fig. 4.6, but the results from anaylsis on the CMAM dataset are shown in the bottom row.

4.6 Preliminary results on interannual variability of ozone STE

Despite the seasonality, the interannual variability of ozone STE is also intriguing, as it is intensively impacted by the major climate variabilites and thus becomes essential for future climate projection. Fig. 4.15 shows the temporal evolution of diagnosed ozone STE (contours) and corresponding interannual variability inferred by the deseasonalized ozone STE (colors). In general, the downward maximum of ozone STE in the mid-latitude NH might increase gently through the 19 years in the SD-WACCM (left), but this trend is not obvious in the SD-CMAM (right). Also, significant ozone STE event can be identified.

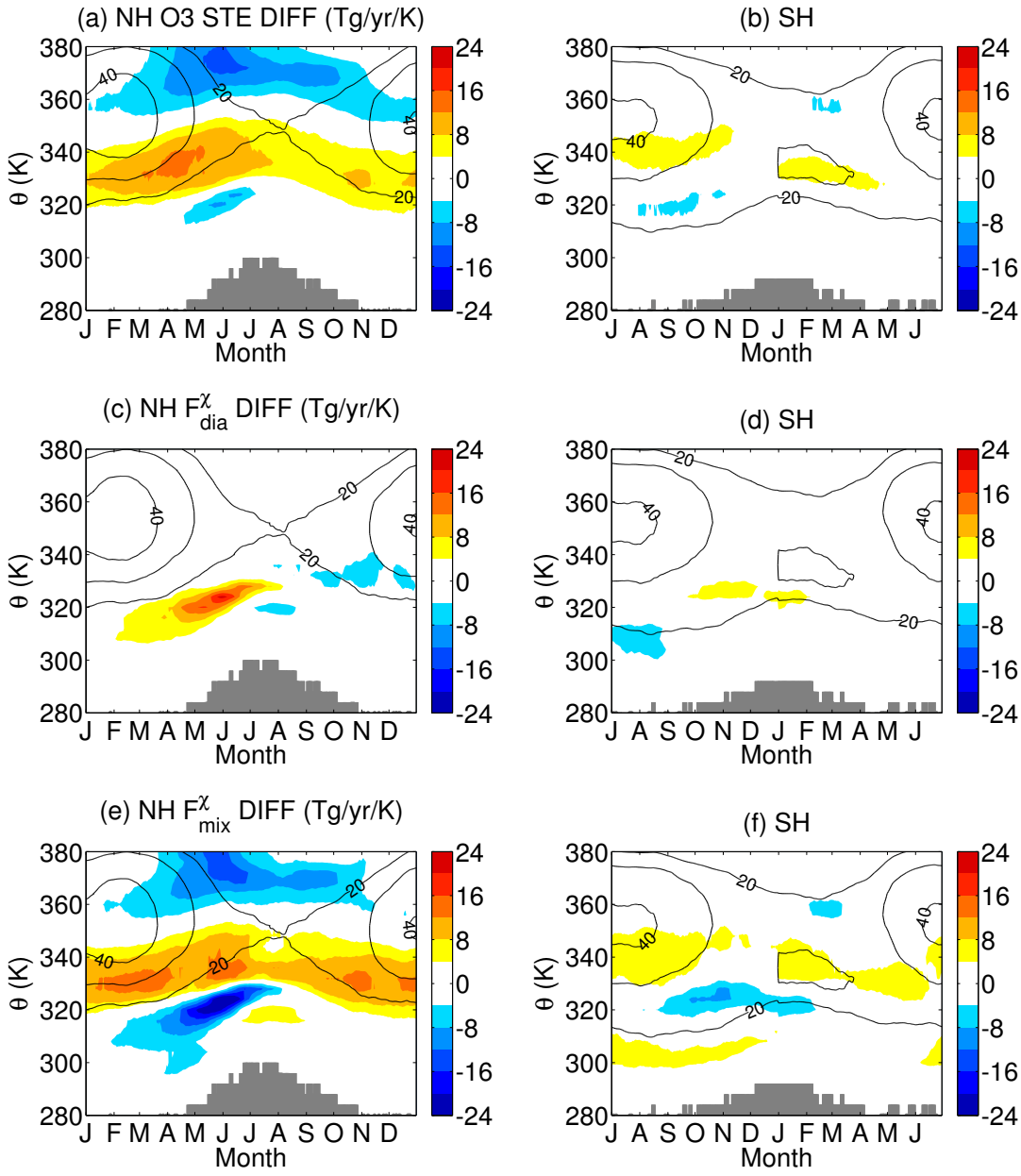

Figure 4.14: Similar to Fig. 4.13, but for the difference of diagnosed ozone STE between the WACCM and the CMAM (CMAM-WACCM): (a)(b) the difference in the net ozone STE flux; (c)(d) the difference in the diabatic component F^{χ}_{dia}; and (e)(f) the difference in the diffusive component F^{χ}_{mix}. Gray shades are defined following the same fashion in Fig. 4.6, but for the CMAM model only.

The strong suppression of mid-latitude downward ozone STE in the years from 1992 to 1995 corresponds to the gigantic volcanic eruption of Mount Pinatubo in 1991 (Tang et al., 2013), which Tang et al. (2013) further argues that the decrease of downward ozone STE primarily results from the reduction of ozone concentration in the stratosphere intead of a potentially slow-down stratospheric residual circulation related to the superbly cooled polar vortex. The enhanced downward ozone STE in 1999 might be related to the informed El Niño event peaking in the winter of 1997 and the spring of 1998, as Neu et al. (2014) have documented a positive correlation between the extratropical ozone STE and the ENSO index. The ENSO physically affect the ozone STE via adjusting the strength and spatial structure of BDC (Yang et al., 2014).

The diagnosed interannual variabiity of ozone STE is also smaller in the SD-CMAM on most of the isentropic surfaces (equivalent latitudes). However, in terms of the hemispherically-integrated ozone STE, the SD-CMAM shows a larger interannual variability (see Fig. 4.12. This might be due to a larger cancellation between the (sub)tropical upward ozone STE and the extratropical downward ozone STE in the SD-WACCM. Although both components are larger in the SD-WACCM, a larger cancellation may yield smaller hemispherically-integrated residue. Moreover, in the NH, the climatological maximum of downward ozone STE ($50^\circ - 70^\circ$ N) in the SD-CMAM lies poleward of the counterpart ($40^\circ - 60^\circ$ N) in the SD-WACCM, as well as the corresponding interannual anomalies, which is consistent with the findings in Fig. 4.13.

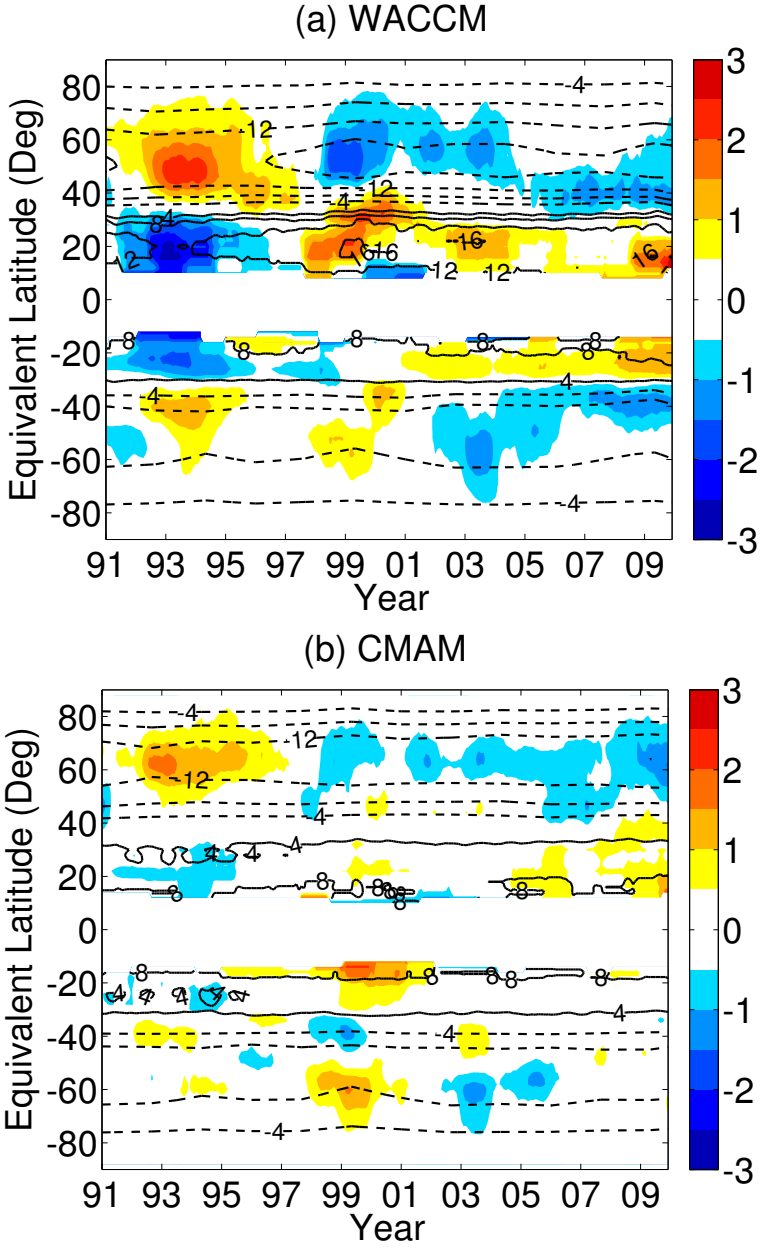

Figure 4.15: The long-term trend and the interannual variability of ozone STE on different isentropic surfaces corresponding to different equivalent latitude (the latitude approximately identifies the location of tropopause on the specific isentropic surface) in the (top) SD-WACCM and the (bottom) SD-CMAM. The trend can be inferred by the diagnosed ozone STE after a 12-month running smooth (contours), and the interannual variability is denoted by the deseasonalized ozone STE with the same 12-month running smooth (colors). All fluxes are upward postive as defined in the previous figures, and only year from 1991 to 2009 are shown for the SD-CMAM dataset.

4.7 Conclusions and discussions

An isentropic STE diagnostic has been implemented onto two datasets. One is a 19-year dataset generated from the control simulation of the Specified Dynamics (SD) version of the Whole Atmosphere Community Model (WACCM), and the other is a 30-year dataset generated from the control simulation of the Specified Dynamics (SD) version of the Canadian Middle Atmosphere Model (CMAM). The diagnostic extends the hemispheric ozone budget in the lowermost stratosphere (LMS) to the budget over discretized isentropic layers. Given that low (high) isentropic surfaces intersect the tropopause at high (low) latitudes, the vertical distribution of STE along different isentropic surfaces corresponds to a meridional distribution of STE over different latitudinal regions.

The overall findings are summarized in Fig. 4.16. This figure shows a noticeable meridional and seasonal distribution of the 19-year climatological mean ozone STE flux, characterized by different directions, magnitudes and seasonalities of STE on different isentropic surfaces.

- **Directions:** net troposphere-to-stratosphere (upward) transport of ozone is analyzed in the (sub)tropics while net stratosphere-to-troposphere (downward) transport of ozone is analyzed in the extratropic. The boundary separating these two regions lies at the core of the subtropical jets.
- **Magnitudes:** the maxima in the extratropical downward ozone STE lies between 40° and 60° N/S on the poleward edge of the tropospheric jets, overlapping the core of normally indiscernible eddy-driven jets where baroclinity is the strongest. Also, these maxima move seasonally with the jet location.

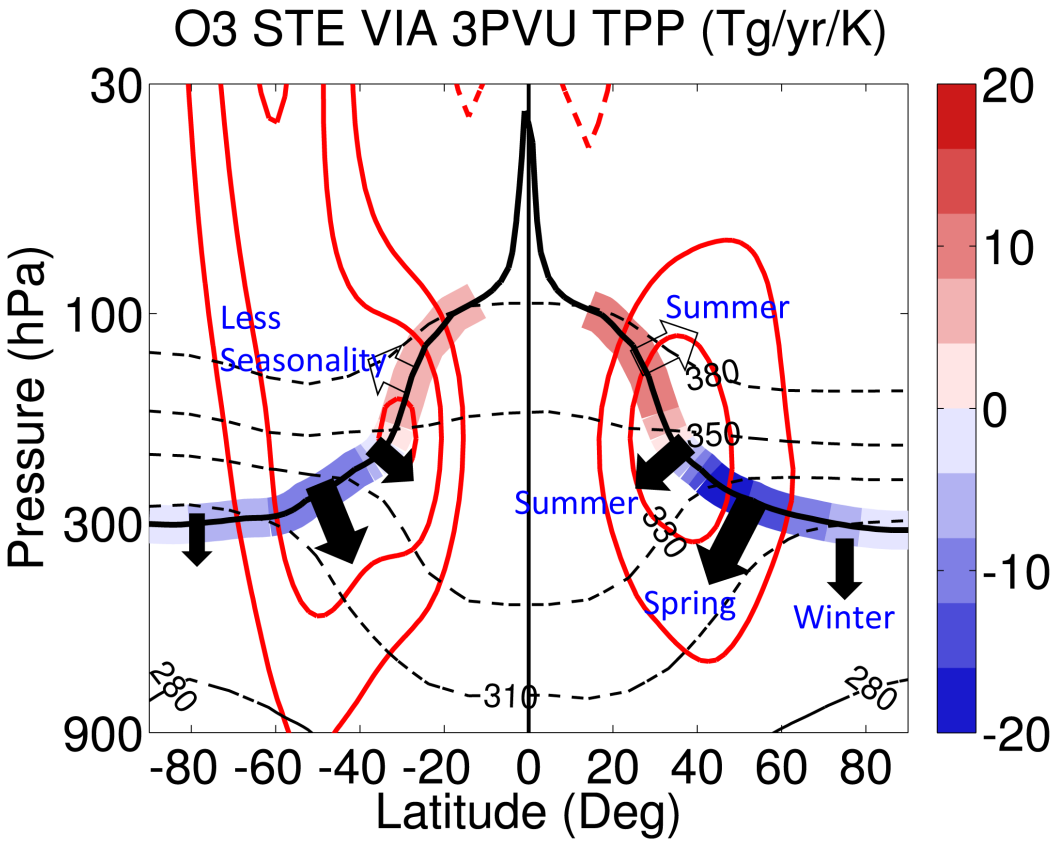

Figure 4.16: Schematic summerizing the direction, magnitude and seasonality of the climatological ozone STE over different isentropic (meridional) regions diagnosed from the SD-WACCM model. Plotting is following the same fashion as in Fig. 4.3(b). Net stratosphere-to-troposphere ozone STE fluxes are denoted as open arrows, while net troposphere-to-stratosphere ozone STE fluxes are denoted as filled arrows. The size of arrow schematically scales the magnitude of the ozone STE flux.

- **Seasonality:** the seasonal maximum of the ozone STE gradually migrates from summer on the higher isentropic surfaces to winter on the lower isentropic surfaces. The summertime maximum on the higher isentropic surfaces is hypothetically associated with the monsoonal circulation (or deep convection over continents) and resultant mixing, while the wintertime maximum on the lower isentropic surfaces facilitates the deep intrusion of

stratospheric ozone into the troposphere, with resultant surface air quality problems in spring after an approximately 3-month transport of stratospheric ozone from the tropopause to the surface (Liang et al., 2009). In addition, less seasnality is diagnosed in the SH.

To interpret the diagnosed spatiotemporal behaviors of ozone STE, a dynamic partition, embedded within the isentropic STE diagnostic, decomposes the net ozone STE flux into two components associated with different PV sources, either differential diabatic heating or isentropic PV mixing. It is shown that the diagnosed spatiotemporal behaviors of ozone STE results from a large cancellation between the predominantly upward ozone STE component associated with the diabatic PV source and the predominantly downward component associated with the isentropic PV mixing. As the latter is slightly larger than the former on almost all isentropic surfaces, the net ozone STE flux spatially and temporally resembles the ozone STE component associated with isentropic PV mixing. The upward ozone STE component associated with the diabatic PV source is induced by differential diabatic heating, driving the tropopause downward so that tropospheric air is brought into the expanding stratosphere. The seasonality of the ozone STE component associated with isentropic PV mixing is due to the seasonality of the mixing and the seasonality of the ozone mixing ratio at the tropopause.

We show that the diagnosed ozone STE is generally insensitive to different tropopause defintions, but the isentropic STE decreases in magnitude as the defined tropopause is moved sufficiently higher (not shown here). An interesting analysis would be to to investigate the sensitivity of the isentropic STE diagnostic to the sampling frequency of the dataset, as the chemical quantities

(e.g. ozone mixing ratio) in some datasets are only available monthly. Hsu and Prather (2014) has recently proposed that the ozone STE flux diagnosed by using the residual vertical velocity fails to capture its interannual variability, suggesting a broad analysis of the characteristic forcing time scale of the stratosphere-troposphere transport is necessary. We detect no significant difference in seasonality of ozone STE using the daily data from SD-WACCM as used in this study vis-à-vis monthly mean data, suggesting that the climatological seasonality of ozone STE is predominantly driven by steady circulation systems (e.g. the residual circulation) instead of transient synoptic variabilities. The mismatch in the interannual variability noted in Hsu and Prather (2014) needs further investigation.

The diagnostic gives a general consistent spatiotemporal pattern about the diagnosed isentropic ozone STE flux between the WACCM model and the CMAM model, with net troposphere-to-stratosphere transport of ozone in (sub)tropics and net stratosphere-to-troposhere transport of ozone in extratropics. Still, noticeable differences can be found, as the diagnosed ozone STE corresponding to the CMAM dataset is relatively smaller in magnitude. This difference is mainly attributed to the diffusive component of the flux F^{χ}_{mix} associated with the isentropic mixing. The underresolved isentropic mixing in the CMAM model might be due to its relatively coarser horizontal resolution. Preliminarly analysis on the interannual variability of ozone STE shows consistent spatiotemporal patterns in both models, and several significant ozone STE events are diagnosed which can be linked to volcanic eruption and tropical sea surface temperature forcing (e.g. warm ENSO).

Given that the ozone mixing ratio decreases significantly from the stratosphere to the troposphere, the upward ozone STE component associated with isentropic PV mixing in (sub)tropics (see Fig. 4.8(c)(d)) suggests an up-gradient transport of ozone from the troposphere to the stratosphere, which is not commonly observed for mixing. One possibllity could be that the mixing is not entirely symmetric due to the asymmetric wave breaking. In the subtropics during the monsoon, persistent cyclonic wave breaking can lead to preferred tropopshere-to-stratosphere transport of ozone, corresponding to the downward movement of tropopause. By contrast, in the extratropics, anticyclonic wave breaking favors net stratosphere-to-troposphere transport of ozone, corresponding to the upward movement of tropopause.

CHAPTER 5

CONCLUSION

In this thesis, we explore the interaction between the stratosphere and the troposphere by enriching our understanding on (a) the dynamic impacts from the troposphere to the stratosphere, (b) the dynamic impacts from the stratosphere to the troposphere, and (c) the chemical transport between the stratosphere and the troposphere.

The tropospheric impacts on the stratosphere via dynamic coupling between the two layers is first investigated in terms of the role of tropical sea surface temperature (SST) forcing in Chapter 2. We identify two distinct patterns of Brewer-Dobson circulation (BDC, the residual circulation in the stratosphere) responses to varied idealized tropical SST perturbations. A shallow strengthening of BDC corresponds to a longitudinally narrow tropical SST heating, while a deep strengthening of BDC corresponds to a zonally symmetric tropical SST heating. We further find that the key causing the shallow versus deep strengthening of BDC lies in the different routes of wave propagation (equatorward versus poleward) and resultant different regions of wave dissipation (subtropical versus high-latitudes) in the lower stratosphere. These results suggest that, while the longitudinally localized SST trends under climate change may contribute to the change in the shallow branch of the BDC, the upward shift of the subtropical jet associated with the zonal SST heating can impact the deep branch of the BDC.

The dynamic impacts from the stratosphere to the troposphere is then discussed in Chapter 3. In this chapter, we examine three possible mechanisms interpreting the downward influence of polar stratospheric ozone depletion. We

find that the mechanism of downward control with eddy feedback (DCWEF, Song and Robinson (2004)), regarding the downward influence from the polar stratospheric ozone depletion to the tropospheric circulation as a downward development of secondary residual circulation and subsequent tropospheric synoptic eddy amplification, is unlikely the dominant mechanism here. Instead, we argue that the altered downward propagation of planetary eddy anomalies and nonlinear planetary eddy - synoptic eddy interaction could be more essential.

In Chapter 4, the chemical transport between the stratosphere and the troposphere is lastly studied. We concentrate on the stratosphere-troposhere exchange (STE) of ozone, and implement an isentropic STE diagnostic that quantifies the STE flux along different isentropic surfaces. Therefore, this diagnostic extends the traditional diagnostic, that is constrained at the hemispheric scale, to give an approximate meridional distribution of the ozone STE flux. We find that net troposphere-to-stratosphere ozone STE occurs on the higher isentropic surfaces in (sub)tropics while net stratosphere-to-troposphere ozone STE prevails on the lower isentropic surfaces in extratropics. The meridional distribution of ozone STE is further complicated by different magnitudes and seasonalities of ozone STE on different isentropic surfaces. Both diabatic heating and isentropic mixing are shown to affect the net ozone STE flux, but their contributions are opposite in sign. The isentropic mixing induces stratosphere-to-troposphere ozone STE and this component is slightly larger than that associated with the diabatic heating. In addition, the diagnosed isentropic ozone STE is generally robust between different models, and a clear interannual variability of ozone STE can be diagnosed.

With all above results, we confirm the importance of stratosphere-troposphere interaction while discussing the status quo of our climate system. In the meantime, it also intrigues us to wonder about the future. Given the importance of stratosphere-troposphere interaction in the current climate, comprehensive climate models, with physical and chemical descriptions of the stratosphere in more sophiscated details, are required to make the projection.

Additionally, more interesting questions have been raised for future potential researches in this subject. In Chapter 2, we have unveiled the zonal asymmetry of SST forcing can lead to different structural change of BDC in stratosphere. It is still mysterious on how this zonally-asymmetric perturbation can result in the changes of circulation, mixing and transport in the troposphere, which is essential to the hydrological and biogeochemical cycles on Earth.

Chapter 3 reveals the mechanism for the downward influence of stratospheric ozone depletion-like cooling and highlight the importance of wave propagation and refraction. However, how specifically the stratospheric circulation and wind changes, initiated by the polar ozone depletion, affect the propagation and refraction of waves require extended dynamic analyses. Also, the details of tropospheric circulation responses to the stratospheric ozone depletion is worthy of investigation. We have shown a poleward shift of the zonal-mean tropospheric jet associated with the stratospheric ozone depletion-like cooling, but the longitudinal structure of the jet change is less known. While discussing the regional impacts via the stratosphere-troposphere dynamic coupling, this factor becomes non-negligible.

Finally, Chapter 4 develops a new STE diagnostic and intensively analyzes the seasonality of ozone STE. In fact, more interesting scientific questions can be

drawn associated with the interannual variability of ozone STE. For example, both stratospheric forcing of ozone variability and tropospheric forcing of global warming are suggested to affect the potential increasing trend of ozone STE in the future, but which one might be more important. Also, the interannual varation of ozone STE is strongly modulated by the ENSO in the troposphere and QBO in the stratosphere (Neu et al., 2014), but the mechanisms beneath are less elucidated.

Besides the scientific scope, studies on the stratosphere-troposphere interaction relies heavily on the model simulations, from simplifed models in Chapter 2 and Chapter 3 to comprehensive models in Chapter 4. Some features about the stratosphere-troposphere coupling are consistent between these two groups of models, and some are inevitably inconsistent. Anayzing their similarities and differences is helpful for not only knowing the important physical processes controlling the stratosphere-troposphere exchange, but offering ideas on the future construction of climate models that can build more coherent physical linkages between these two group of distinct models.

APPENDIX A

CALCULATION OF THE ANNUAL CYCLE OF EDDY FORCINGS

We follow the method described in Domeisen et al. (2013) that extends the time mean eddy forcing in KP04 to instantaneous eddy forcing and to zonal wavenumber decomposition. The method can be illustrated using an advection equation with a damping term

$$\frac{\partial q}{\partial t} = -u \cdot \nabla q - k(q - q_{eq}) \equiv F(u, q), \tag{A.1}$$

where q is a tracer, k is a damping rate, and q_{eq} is a prescribed zonally symmetric equilibrium profile of the tracer. $F(u, q)$ is an operator for the instantaneous local tendency of q associated with advection and damping. We apply the tendency operator $F(.)$ to the zonal mean terms

$$\overline{F(\overline{u}, \overline{q})} = -\overline{u} \cdot \nabla \overline{q} - k(\overline{q} - q_{eq}) \tag{A.2}$$

and then to the zonal means plus an eddy component (e.g., synoptic, planetary, or total eddies)

$$\overline{F(\overline{u} + u^e, \overline{q} + q^e)} = -\overline{u} \cdot \nabla \overline{q} - k(\overline{q} - q_{eq}) - \overline{u^e \cdot \nabla q^e} \tag{A.3}$$

Here overbars denote the zonal means, and the superscript e denotes an eddy term. The eddy forcing can be obtained from the difference between (A.2) and (A.3) to yield

$$\overline{u^e \cdot \nabla q^e} = \overline{F(\overline{u}, \overline{q})} - \overline{F(\overline{u} + u^e, \overline{q} + q^e)}\,. \tag{A.4}$$

In practice, the tendency operator $F(.)$ is calculated by integrating the primitive equation model forward by one time step using instantaneous daily zonal and meridional winds, temperature, and surface pressure. We first calculate the

tendencies for the zonal mean fields and then compute the tendencies for zonal means plus the eddy term. The difference of the two yields the instantaneous eddy forcing in Eq. (A.4). The annual cycle of the eddy forcing is obtained by averaging on the same day of all the 80 years. The same procedure is repeated for synoptic, planetary, and total eddy forcings.

The zonally symmetric model, corresponding to the full model as described by Eq. (A.1), is constructed as follows,

$$\frac{\partial \tilde{q}}{\partial t} = -\tilde{u} \cdot \nabla \tilde{q} - k(\tilde{q} - q_{eq}) - \overline{u^s \cdot \nabla q^s} - \overline{u^p \cdot \nabla q^p} \tag{A.5}$$

where the model variables $\tilde{q}$ and $\tilde{u}$ are zonally symmetric, i.e., only the zonal means are resolved and integrated forward in the model. The synoptic eddy forcing $-\overline{u^s \cdot \nabla q^s}$ and planetary eddy forcing $-\overline{u^p \cdot \nabla q^p}$ are derived from the corresponding full model by Eq. (A.4), and then these eddy forcings are specified in the zonally symmetric model. More explicit expressions of the zonally symmetric model with zonal winds, temperature, and surface pressure can be found in appendix B of Sun et al. (2011). As shown by a comparison between Figs. 3.3 (d)(e)(f) and Figs. 3.4 (a)(b)(c), the zonally symmetric model simulation successfully reproduces the full model responses to polar stratospheric cooling.

APPENDIX B

DISCRETIZATION OF THE ISENTROPIC STE DIAGNOSTICS

Following Eq. (4.4), the isentropic ozone diagnostics at time step τ, and isentropic layer k is discretized as

$$F^{\chi}_{STE}|_{\tau,k} = \frac{M(\chi)|_{\tau+1,k} - M(\chi)|_{\tau-1,k}}{t|_{\tau+1} - t|_{\tau-1}} + \frac{M\left(\chi\dot{\theta}\right)\Big|_{\tau,k+1} - M\left(\chi\dot{\theta}\right)\Big|_{\tau,k-1}}{\theta|_{k+!} - \theta|_{k-1}} - M(\dot{\chi})|_{\tau,k} \quad \text{(B.1)}$$

where the density-weighted integral of quantity $\mathcal{A}$ in the stratosphere (the same operator $M(\cdot)$ in Eq. (4.4) and (4.6)) is defined as

$$M(\mathcal{A})|_{\tau,k} = \sum_{j=j^*} \sum_{i=i^*} \mathcal{A}_{j,i}\sigma_{j,i}\mathrm{dS}_{j,i}|_{\tau,k} \quad \text{(B.2)}$$

for the pairs of j^* (latitude), i^* (longitude) identifying the points in the stratosphere by satisfying either

$$p_{j^*,i^*}|_{\tau,k} \le p_{trop\ j^*,i^*}|_{\tau,k} \quad \text{(B.3)}$$

or

$$\begin{aligned} q_{j^*,i^*}|_{\tau,k} &\ge Q_{j^*,i^*}|_{\tau,k} \qquad \text{in the NH} \\ q_{j^*,i^*}|_{\tau,k} &\le Q_{j^*,i^*}|_{\tau,k} \qquad \text{in the SH} \end{aligned} \quad \text{(B.4)}$$

Here σ denotes the isentropic density, and $\mathrm{dS}_{j,i}$ denotes the area for the grid element at latitudinal point j and longitudinal point i, and adjacent half-grid points are used for the calculation of $\mathrm{dS}_{j,i}$, which $\mathrm{dS}_{j,i} = a^2\left(\sin\phi_{j+1/2} - \sin\phi_{j-1/2}\right)(\lambda_{i+1/2} - \lambda_{i-1/2})$. ϕ is latitude, λ is longitude, and a is the planetary radius of the Earth. Note that isentropic STE flux is calculated in each hemisphere by only considering half grid points in Eq. B.3 and B.4.

BIBLIOGRAPHY

Allen, D. and N. Nakamura, 2001: A seasonal climatology of effective diffusivity in the stratosphere. *Journal of Geophysical Research*, **106 (D8)**, 7917–7935.

Andrews, D., J. Holton, and C. Leovy, 1987: *Middle Atmosphere Dynamics*. Academic Press, 489 pp.

Appenzeller, C., J. R. Holton, and K. H. Rosenlof, 1996: Seasonal variation of mass transport across the tropopause. *Journal of Geophysical Research*, **101 (D10)**, 15 071, doi:10.1029/96JD00821.

Baldwin, M. P. and T. J. Dunkerton, 2001: Stratospheric harbingers of anomalous weather regimes. *Science*, **294 (5542)**, 581–4.

Birner, T. and H. Bönisch, 2011: Residual circulation trajectories and transit times into the extratropical lowermost stratosphere. *Atmospheric Chemistry and Physics*, **11 (2)**, 817–827, doi:10.5194/acp-11-817-2011.

Bönisch, H., A. Engel, T. Birner, P. Hoor, D. W. Tarasick, and E. a. Ray, 2011: On the structural changes in the Brewer-Dobson circulation after 2000. *Atmospheric Chemistry and Physics*, **11 (8)**, 3937–3948.

Brewer, A. W., 1949: Evidence for a world circulation provided by the measurements of helium and water vapor distribution in the stratosphere. *Quarterly Journal of the Royal Meteorological Society*, **75 (326)**, 351–363.

Butchart, N., M. Office, and H. Centre, 2014: Reviews of Geophysics The Brewer-Dobson circulation. *Reviews of Geophysicseophysics*, **52**, 157–184, doi:10.1002/2013RG000448.One.

Butchart, N., et al., 2010: Chemistry-climate model simulations of twenty-First century stratospheric climate and circulation changes. *Journal of Climate*, **23**, 5349–5374.

Butler, A. H., D. W. J. Thompson, and R. Heikes, 2010: The Steady-State Atmospheric Circulation Response to Climate Changelike Thermal Forcings in a Simple General Circulation Model. *Journal of Climate*, **23 (13)**, 3474–3496, doi:10.1175/2010JCLI3228.1.

Calvo, N., R. R. Garcia, W. J. Randel, and D. R. Marsh, 2010: Dynamical mechanism for the increase in tropical upwelling in the lowermost tropical stratosphere during warm ENSO events. *Journal of the Atmospheric Sciences*, **67 (7)**, 2331–2340.

Chapman, S., 1930: On ozone and atomic oxygen in the upper atmosphere. *Philosophical Magazine*, **10 (64)**, 369–383.

Chen, G. and I. M. Held, 2007: Phase speed spectra and the recent poleward shift of Southern Hemisphere surface westerlies. *Geophysical Research Letters*, **34 (21)**, L21 805, doi:10.1029/2007GL031200, URL `http://doi.wiley.com/10.1029/2007GL031200`.

Chen, G., J. Lu, and D. M. W. Frierson, 2008: Phase Speed Spectra and the Latitude of Surface Westerlies: Interannual Variability and Global Warming Trend. *Journal of Climate*, **21 (22)**, 5942–5959.

Chen, G., R. A. Plumb, and J. Lu, 2010: Sensitivities of zonal mean atmospheric circulation to SST warming in an aqua-planet model. *Geophysical Research Letters*, **37 (12)**, L12 701.

Chen, G. and L. Sun, 2011: Mechanisms of the tropical upwelling branch of the BrewerDobson circulation: The role of extratropical waves. *Journal of the Atmospheric Sciences*, **68 (12)**, 2878–2892.

Chen, P., 1995: Isentropic cross-tropopause mass exchange in the extratropics. *Journal of Geophysical Research*, **100 (95)**, 661–673, URL `http://www.agu.org/pubs/crossref/1995/95JD01264.shtml`.

Chen, P. and W. Robinson, 1992: Propagation of Planetary Waves between the Troposphere and Stratosphere. *Journal of the Atmospheric Sciences*, **49 (24)**, 2533–2545.

Collins, W. J., R. Derwent, B. Garnier, C. E. Johnson, and M. G. Sanderson, 2003: Effect of stratosphere-troposphere exchange on the future tropospheric ozone trend. *Journal of Geophysical Research*, **108 (D12)**, 8528, doi: 10.1029/2002JD002617.

Crutzen, P. J. and M. Oppenheimer, 2008: Learning about ozone depletion. *Climatic Change*, **89**, 143–154, doi:10.1007/s10584-008-9400-6.

Danielsen, E., 1968: Stratospheric-Tropospheric Exchange Based on Radioactivity, Ozone and Potential Vorticity. *Journal of the Atmospheric Sciences*, **25**, 502–518.

Deckert, R. and M. Dameris, 2008: Higher tropical SSTs strengthen the tropical upwelling via deep convection. *Geophysical Research Letters*, **35 (10)**, L10 813.

Dee, D. P., et al., 2011: The ERA-Interim reanalysis: configuration and performance of the data assimilation system. *Quarterly Journal of the Royal Meteorological Society*, **137 (656)**, 553–597.

Delworth, T. L., et al., 2006: GFDL's CM2 Global Coupled Climate Models. Part I: Formulation and Simulation Characteristics. *Journal of Climate*, **19 (5)**, 643–674, doi:10.1175/JCLI3629.1.

Dobson, G. M. B., 1956: Origin and distribution of the polyatomic molecules in the atmosphere. *Proceedings of the Royal Society of London. Series A*, **236 (1205)**, 187–193.

Domeisen, D. I., L. Sun, and G. Chen, 2013: The role of synoptic eddies in the tropospheric response to stratospheric variability. *Geophysical Research Letters*, doi:10.1002/grl.50943.

Donner, L. J., et al., 2011: The Dynamical Core, Physical Parameterizations, and Basic Simulation Characteristics of the Atmospheric Component AM3 of the GFDL Global Coupled Model CM3. *Journal of Climate*, **24 (13)**, 3484–3519.

Edmon Jr, H. J., B. J. Hoskins, and M. E. McIntyre, 1980: Eliassen-Palm cross sections for the troposphere. *Journal of Atmospheric Sciences*, **37 (12)**, 2600–2616.

Edouard, S., R. Vautard, and G. Brunet, 1997: On the maintenance of potential vorticity in isentropic coordinates. *Quarterly Journal of the Royal Meteorological Society*, **123 (1997)**, 2069–2094.

Eichelberger, S. J. and D. L. Hartmann, 2005: Changes in the strength of the Brewer-Dobson circulation in a simple AGCM. *Geophysical Research Letters*, **32 (15)**, L15 807.

Engel, A., et al., 2008: Age of stratospheric air unchanged within uncertainties over the past 30 years. *Nature Geoscience*, **2 (1)**, 28–31.

Fiore, A. M., 2002: Linking ozone pollution and climate change: The case

for controlling methane. *Geophysical Research Letters*, **29 (19)**, 1919, doi: 10.1029/2002GL015601.

Fry, L. M., F. a. Jew, and P. K. Kuroda, 1960: On the stratospheric fallout of strontium-90: The spring peak of 1959. *Journal of Geophysical Research*, **65 (7)**, 2061–2066, doi:10.1029/JZ065i007p02061.

Garcia, R. R. and W. J. Randel, 2008: Acceleration of the BrewerDobson circulation due to increases in greenhouse gases. *Journal of the Atmospheric Sciences*, **65 (8)**, 2731–2739.

Garcia, R. R., W. J. Randel, and D. E. Kinnison, 2011: On the Determination of Age of Air Trends from Atmospheric Trace Species. *Journal of the Atmospheric Sciences*, **68 (1)**, 139–154.

Garcia-Herrera, R., N. Calvo, R. R. Garcia, and M. A. Giorgetta, 2006: Propagation of ENSO temperature signals into the middle atmosphere: A comparison of two general circulation models and ERA-40 reanalysis data. *Journal of Geophysical Research*, **111**, 1–14.

Garny, H., M. Dameris, W. J. Randel, G. E. Boderker, and R. Deckert, 2011: Dynamically forced increase of tropical upwelling in the lower stratosphere. *Journal of the Atmospheric Sciences*, **68**, 1214–1233.

Gerber, E. P., 2012: Stratospheric versus Tropospheric Control of the Strength and Structure of the BrewerDobson Circulation. *Journal of the Atmospheric Sciences*, **69 (9)**, 2857–2877.

Gettelman, A., J. Holton, and K. Rosenlof, 1997: Mass fluxes of O3, CH4, N2O and CF2Cl2 in the lower stratosphere calculated from observational data. *Journal of Geophysical Research*, **102 (97)**.

Hall, T. M. and R. A. Plumb, 1994: Age as a diagnostic of stratospheric transport. *Journal of Geophysical Research*, **99 (D1)**, 1059–1070.

Hardiman, S. C., N. Butchart, P. H. Haynes, and S. H. E. Hare, 2007: A note on forced versus internal variability of the stratosphere. *Geophysical Research Letters*, **34 (12)**, L12 803.

Harnik, N. and R. S. Lindzen, 2001: The effect of reflecting surfaces on the vertical structure and variability of stratospheric planetary waves. *Journal of the Atmospheric Sciences*, **58**, 2872–2894.

Haynes, P. and T. Shepherd, 1989: The importance of surface pressure changes in the response of the atmosphere to zonallysymmetric thermal and mechanical forcing. *Quarterly Journal of the Royal Meteorological Society*, **115 (490)**, 1181–1208.

Haynes, P. and E. Shuckburgh, 2000a: Effective diffusivity as a diagnostic of atmospheric transport 1. Stratosphere. *Journal of Geophysical Research*, **105 (D18)**, 22 777–22 794.

Haynes, P. and E. Shuckburgh, 2000b: Effective diffusivity as a diagnostic of atmospheric transport 2. Troposphere and lower stratosphere. *Journal of Geophysical Research*, **105 (D18)**, 22 795–22 810.

Haynes, P. H., C. J. Marks, M. E. Mcintyre, T. G. Shepherd, and K. P. Shine, 1991: On the "Downward Control" of extratropical diabatic circulation by eddy-induced mean zonal forces. *Journal of Atmospheric Sciences*, **48 (4)**, 651–678.

Haynes, P. H., D. A. Poet, and E. F. Shuckburgh, 2007: Transport and Mixing in Kinematic and Dynamically Consistent Flows. *Journal of the Atmospheric Sciences*, **64 (10)**, 3640–3651.

Hegglin, M. I. and T. G. Shepherd, 2009: Large climate-induced changes in ultraviolet index and stratosphere-to-troposphere ozone flux. *Nature Geoscience*, **2 (10)**, 687–691.

Hess, P., D. Kinnison, and Q. Tang, 2015: Ensemble simulations of the role of the stratosphere in the attribution of tropospheric ozone variability. *Atmospheric Chemistry and Physics*, **15**, 2341–2365, doi:10.5194/acpd-14-20461-2014.

Hess, P. G. and R. Zbinden, 2013: Stratospheric impact on tropospheric ozone variability and trends: 19902009. *Atmospheric Chemistry and Physics*, **13 (2)**, 649–674.

Hoinka, K. P., 1997: The tropopause: Discovery, definition and demarcation. *Meteorologische Zeitschrift*, **6**, 281–303.

Holton, J., 1986: Meridional distribution of stratospheric trace constituents. *Journal of the Atmospheric Sciences*, **43 (12)**, 1238–1242.

Holton, J. R., 1990: On the global exchange of mass between the stratosphere and troposphere. *Journal of the Atmospheric Sciences*, **47 (3)**, 392–395, doi: 10.1175/1520-0469(1990)047¡0392:OTGEOM¿2.0.CO;2.

Holton, J. R., 2004: *An Introduction to Dynamic Meteorology*. 4th ed., Academic Press, Burlington, MA, 535 pp.

Holton, J. R., P. H. Haynes, M. E. Mcintyre, A. R. Douglass, and R. B. Rood, 1995: Stratosphere-troposphere exchange. *Review of Geophysics*, **33 (4)**, 403–439.

Hsu, J. and M. J. Prather, 2005: Diagnosing the stratosphere-to-troposphere flux of ozone in a chemistry transport model. *Journal of Geophysical Research*, **110 (D19)**, D19 305, doi:10.1029/2005JD006045.

Hsu, J. and M. J. Prather, 2009: Stratospheric variability and tropospheric ozone. *Journal of Geophysical Research*, **114 (D6)**, D06 102, doi:10.1029/2008JD010942.

Hsu, J. and M. J. Prather, 2014: Is the residual vertical velocity a good proxy for stratosphere-troposphere exchange of ozone? *Geophysical research letters*, 9024–9032, doi:10.1002/2014GL061994.1.

James, P., A. Stohl, C. Forster, S. Eckhardt, P. Seibert, and A. Frank, 2003: A 15-year climatology of stratospheretroposphere exchange with a Lagrangian particle dispersion model 2. Mean climate and seasonal variability. *Journal of Geophysical Research*, **108 (D12)**, 8522, doi:10.1029/2002JD002639.

Jing, P., D. M. Cunnold, H. J. Wang, and E.-S. Yang, 2004: Isentropic Cross-Tropopause Ozone Transport in the Northern Hemisphere. *Journal of the Atmospheric Sciences*, **61 (9)**, 1068–1078, doi:10.1175/1520-0469(2004)061¡1068:ICOTIT¿2.0.CO;2.

Kentarchos, A. S. and G. J. Roelofs, 2003: A model study of stratospheric ozone in the troposphere and its contribution to tropospheric OH formation. *Journal of Geophysical Research*, **108 (D12)**, 8517, doi:10.1029/2002JD002598.

Kerr-Munslow, A. M. and W. A. Norton, 2006: Tropical wave driving of the annual cycle in tropical tropopause temperatures. Part I: ECMWF analyses. *Journal of the Atmospheric Sciences*, **63**, 1410–1419.

Kolstad, E. W., T. Breiteig, and A. a. Scaife, 2010: The association between stratospheric weak polar vortex events and cold air outbreaks in the Northern Hemisphere. *Quarterly Journal of the Royal Meteorological Society*, **136 (649)**, 886–893, doi:10.1002/qj.620, 0906.0027.

Kushner, P. and L. Polvani, 2004: Stratosphere-troposphere coupling in a relatively simple AGCM: The role of eddies. *Journal of Climate*, **17**, 629–639.

Kushner, P. and L. Polvani, 2006: Stratosphere Troposphere Coupling in a Relatively Simple AGCM: Impact of the Seasonal Cycle. *Journal of Climate*, **19**, 5721–5727.

Lee, S. and S. B. Feldstein, 2013: Detecting ozone- and greenhouse gas-driven wind trends with observational data. *Science*, **339 (6119)**, 563–7, doi: 10.1126/science.1225154.

Li, F., J. Austin, and J. Wilson, 2008: The Strength of the BrewerDobson Circulation in a Changing Climate: Coupled ChemistryClimate Model Simulations. *Journal of Climate*, **21 (1)**, 40–57.

Liang, Q., A. R. Douglass, B. N. Duncan, R. S. Stolarski, and J. C. Witte, 2009: The governing processes and timescales of stratosphere-to-troposphere transport and its contribution to ozone in the Arctic troposphere. *Atmospheric Chemistry and Physics*, **9**, 3011–3025.

Lin, M., et al., 2012: Springtime high surface ozone events over the western United States: Quantifying the role of stratospheric intrusions. *Journal of Geophysical Research: Atmospheres*, **117 (D21)**, n/a–n/a, doi: 10.1029/2012JD018151.

Lin, P. and Q. Fu, 2013: Changes in various branches of the Brewer-Dobson circulation from an ensemble of chemistry climate models. *Journal of Geophysical Research: Atmospheres*, **118 (1)**, 73–84, doi:10.1029/2012JD018813.

Liu, J. and T. Schneider, 2011: Convective Generation of Equatorial Superro-

tation in Planetary Atmospheres. *Journal of the Atmospheric Sciences*, **68 (11)**, 2742–2756.

Lorenz, D. J. and E. T. DeWeaver, 2007: Tropopause height and zonal wind response to global warming in the IPCC scenario integrations. *Journal of Geophysical Research*, **112 (D10)**, D10 119, doi:10.1029/2006JD008087.

Lorenz, D. J. and D. L. Hartmann, 2001: EddyZonal Flow Feedback in the Southern Hemisphere. *Journal of the Atmospheric Sciences*, **58 (21)**, 3312–3327, doi:10.1175/1520-0469(2001)058¡3312:EZFFIT¿2.0.CO;2.

Lu, J., G. Chen, and D. M. W. Frierson, 2008: Response of the Zonal Mean Atmospheric Circulation to El Niño versus Global Warming. *Journal of Climate*, **21 (22)**, 5835–5851.

Mahlman, J. D., H. I. Levy, and W. J. Moxim, 1986: Three-Dimensional Simulations of Stratospheric N2O: Predictions for Other. *Journal of Geophysical Research*, **91**, 2687–2707.

Matsuno, T., 1970: Vertical Propagtion of Stationary Planetary Waves in the Winter Northern Hemisphere. *Journal of the Atmospheric Sciences*, **27**, 871–883.

McLandress, C., A. I. Jonsson, D. A. Plummer, M. C. Reader, J. F. Scinocca, and T. G. Shepherd, 2010: Separating the dynamical effects of climate change and ozone depletion. Part I: southern hemisphere stratosphere. *Journal of Climate*, **23 (18)**, 5002–5020.

McLandress, C. and T. G. Shepherd, 2009: Simulated Anthropogenic Changes in the BrewerDobson Circulation, Including Its Extension to High Latitudes. *Journal of Climate*, **22 (6)**, 1516–1540.

Monks, P. S., 2000: A review of the observations and origins of the spring ozone maximum. *Atmospheric Environment*, **34 (21)**, 3545–3561, doi:10.1016/S1352-2310(00)00129-1.

Nakamura, N., 1995: Modified Lagrangian-Mean Diagnostics of the Stratospheric Polar Vorticies. Part I: Formulation and Analysis of GFDL SKYHI GCM. *Journal of the Atmospheric Sciences*, **52 (11)**, 2096–2108.

Nakamura, N., 1996: Two-dimesional mixing, formation, and permeability diagnosed in an area coordinate. *Journal of Atmospheric Sciences*, **53 (11)**, 5002–5020.

Nakamura, N., 2007: Extratropical stratosphere-troposphere mass exchange associated with isentropic mixing: A 19922005 climatology derived from advection-diffusion calculations. *Journal of Geophysical Research*, **112 (D24)**, D24 303, doi:10.1029/2006JD008382.

Neale, R. B. and B. J. Hoskins, 2000: A standard test for AGCMs including their physical parametrizations: I: The proposal. *Atmospheric Science Letters*, **1 (2)**, 101–107.

Neu, J. L., T. Flury, G. L. Manney, M. L. Santee, N. J. Livesey, and J. Worden, 2014: Tropospheric ozone variations governed by changes in stratospheric circulation. *Nature Geoscience*, **7 (5)**, 340–344, doi:10.1038/ngeo2138.

Norton, W. A., 2006: Tropical wave driving of the annual cycle in tropical tropopause temperatures. Part II: model results. *Journal of the Atmospheric Sciences*, **63 (5)**, 1420–1431.

Olsen, M. a., A. R. Douglass, and T. B. Kaplan, 2013: Variability of extratropical ozone stratosphere-troposphere exchange using microwave limb sounder

observations. *Journal of Geophysical Research: Atmospheres*, **118 (2)**, 1090–1099, doi:10.1029/2012JD018465.

Olsen, M. A., A. R. Douglass, and M. R. Schoeberl, 2003: A comparison of Northern and Southern Hemisphere cross-tropopause ozone flux. *Geophysical Research Letters*, **30 (7)**, doi:10.1029/2002GL016538.

Olsen, M. A., M. R. Schoeberl, and A. R. Douglass, 2004: Stratosphere-troposphere exchange of mass and ozone. *Journal of Geophysical Research*, **109 (D24)**, D24 114, doi:10.1029/2004JD005186.

Olsen, M. a., M. R. Schoeberl, and J. E. Nielsen, 2007: Response of stratospheric circulation and stratosphere-troposphere exchange to changing sea surface temperatures. *Journal of Geophysical Research*, **112 (D16)**, D16 104.

Orr, A., T. J. Bracegirdle, J. S. Hosking, W. Feng, H. K. Roscoe, and J. D. Haigh, 2013: Strong Dynamical Modulation of the Cooling of the Polar Stratosphere Associated with the Antarctic Ozone Hole. *Journal of Climate*, **26 (2)**, 662–668, doi:10.1175/JCLI-D-12-00480.1.

Orr, A., T. J. Bracegirdle, J. S. Hosking, T. Jung, J. D. Haigh, T. Phillips, and W. Feng, 2012: Possible Dynamical Mechanisms for Southern Hemisphere Climate Change due to the Ozone Hole. *Journal of the Atmospheric Sciences*, **69 (10)**, 2917–2932, doi:10.1175/JAS-D-11-0210.1.

Plumb, R. A., 2002: Stratospheric transport. *Journal of the Meteorological Society of Japan. Ser. II*, **80**, 793–809.

Polvani, L. and P. Kushner, 2002: Tropospheric response to stratospheric perturbations in a relatively simple general circulation model. *Geophysical research letters*, **29 (7)**, 40–43.

Polvani, L. M., D. W. Waugh, G. J. P. Correa, and S.-W. Son, 2011: Stratospheric Ozone Depletion: The Main Driver of Twentieth-Century Atmospheric Circulation Changes in the Southern Hemisphere. *Journal of Climate*, **24 (3)**, 795–812, doi:10.1175/2010JCLI3772.1.

Postel, G. and M. Hitchman, 1999: A Climatology of Rossby Wave Breaking along the Subtropical Tropopause. *Journal of the Atmospheric Sciences*, **56**, 359–373.

Prather, M. J., X. Zhu, Q. Tang, J. Hsu, and J. L. Neu, 2011: An atmospheric chemist in search of the tropopause. *Journal of Geophysical Research*, **116 (D4)**, D04 306, doi:10.1029/2010JD014939.

Randel, W. J., R. R. Garcia, N. Calvo, and D. Marsh, 2009: ENSO influence on zonal mean temperature and ozone in the tropical lower stratosphere. *Geophysical Research Letters*, **36 (15)**, L15 822.

Randel, W. J., R. R. Garcia, and F. Wu, 2008: Dynamical balances and tropical stratospheric upwelling. *Journal of the Atmospheric Sciences*, **65 (11)**, 3584–3595.

Ray, E. A., et al., 2010: Evidence for changes in stratospheric transport and mixing over the past three decades based on multiple data sets and tropical leaky pipe analysis. *Journal of Geophysical Research*, **115 (D21)**, D21 304.

Reed, R. and C. Vicek, 1969: The Annual Temperature Variation in the Lower Tropical Stratosphere. *Journal of the Atmospheric Sciences*, **26**, 163–167.

Rind, D., D. Shindell, P. Lonergan, and N. K. Balachandran, 1998: Climate change and the middle atmosphere. Part III: The doubled CO2 climate revisited. *Journal of Climate*, **11**, 876–894.

Ryu, J.-H. and S. Lee, 2010: Effect of Tropical Waves on the Tropical Tropopause Transition Layer Upwelling. *Journal of the Atmospheric Sciences*, **67 (10)**, 3130–3148.

Schoeberl, M. R., 2004: Extratropical stratosphere-troposphere mass exchange. *Journal of Geophysical Research*, **109 (D13)**, D13 303, doi:10.1029/2004JD004525.

Scinocca, J. and P. Haynes, 1998: Dynamical forcing of stratospheric planetary waves by tropospheric baroclinic eddies. *Journal of the Atmospheric Sciences*, **55 (14)**, 2361–2392.

Scott, R. and J. Cammas, 2002: Wave breaking and mixing at the subtropical tropopause. *Journal of the Atmospheric Sciences*, **59**, 2347–2361.

Scott, R. K., E. F. Shuckburgh, J. P. Cammas, and B. Legras, 2003: Stretching rates and equivalent length near the tropopause. *Journal of Geophysical Research*, **108 (D13)**, 4394.

Shaw, T. a., J. Perlwitz, and N. Harnik, 2010: Downward Wave Coupling between the Stratosphere and Troposphere: The Importance of Meridional Wave Guiding and Comparison with Zonal-Mean Coupling. *Journal of Climate*, **23 (23)**, 6365–6381, doi:10.1175/2010JCLI3804.1.

Shepherd, T. G. and C. McLandress, 2011: A Robust Mechanism for Strengthening of the BrewerDobson Circulation in Response to Climate Change: Critical-Layer Control of Subtropical Wave Breaking. *Journal of the Atmospheric Sciences*, **68 (4)**, 784–797.

Shuckburgh, E., F. DOvidio, and B. Legras, 2009: Local Mixing Events in the Upper Troposphere and Lower Stratosphere. Part II: Seasonal and Interannual Variability. *Journal of the Atmospheric Sciences*, **66 (12)**, 3695–3706.

Simpson, I. R., M. Blackburn, and J. D. Haigh, 2009: The Role of Eddies in Driving the Tropospheric Response to Stratospheric Heating Perturbations. *Journal of the Atmospheric Sciences*, **66 (5)**, 1347–1365.

Simpson, I. R., T. G. Shepherd, and M. Sigmond, 2011: Dynamics of the lower stratospheric circulation response to ENSO. *Journal of the Atmospheric Sciences*, **68**, 2537–2556.

Sjoberg, J. P. and T. Birner, 2012: Transient tropospheric forcing of sudden stratospheric warmings. *Journal of the Atmospheric Sciences*, **69**, 3420–3432, doi:10.1175/JAS-D-11-0195.1.

Skerlak, B., M. Sprenger, and H. Wernli, 2014: A global climatology of stratosphere-troposphere exchange using the ERA-interim dataset from 1979 to 2011. *Atmospheric Chemistry and Physics*, **14**, 913–937, doi:10.5194/acp-14-913-2014.

Song, Y. and W. Robinson, 2004: Dynamical mechanisms for stratospheric influences on the troposphere. *Journal of the Atmospheric Sciences*, **61**, 1711–1725.

Stevenson, D. S., et al., 2006: Multimodel ensemble simulations of present-day and near-future tropospheric ozone. *Journal of Geophysical Research*, **111 (D8)**, D08 301, doi:10.1029/2005JD006338.

Stocker, T. F., et al., 2001: Intergovenmental Panel on Climate Change (IPCC) Climate Change. Tech. rep., 417–457 pp.

Sun, L., G. Chen, and W. A. Robinson, 2014: The Role of Stratospheric Polar Vortex Breakdown in Southern Hemisphere Climate Trends. *Journal of Atmospheric Sciences*, doi:10.1175/JAS-D-13-0290.1.

Sun, L., C. Deser, and R. A. Tomas, 2015: Mechanisms of Stratospheric and Tropospheric Circulation Response to Projected Arctic Sea Ice Loss. *Journal of Climate*, submitted.

Sun, L. and W. a. Robinson, 2009: Downward influence of stratospheric final warming events in an idealized model. *Geophysical Research Letters*, **36 (3)**, L03 819, doi:10.1029/2008GL036624.

Sun, L., W. a. Robinson, and G. Chen, 2011: The Role of Planetary Waves in the Downward Influence of Stratospheric Final Warming Events. *Journal of the Atmospheric Sciences*, **68 (12)**, 2826–2843, doi:10.1175/JAS-D-11-014.1.

Tang, Q., P. G. Hess, B. Brown-Steiner, and D. E. Kinnison, 2013: Tropospheric ozone decrease due to the Mount Pinatubo eruption: Reduced stratospheric influx. *Geophysical Research Letters*, **40 (20)**, 5553–5558, doi:10.1002/2013GL056563.

Tang, Q., M. J. Prather, and J. Hsu, 2011: Stratosphere-troposphere exchange ozone flux related to deep convection. *Geophysical Research Letters*, **38 (3)**, L03 806, doi:10.1029/2010GL046039.

Thompson, D., J. Furtado, and T. Shepherd, 2006: On the Tropospheric Response to Anomalous Stratospheric Wave Drag and Radiative Heating. *Journal of the Atmospheric Sciences*, **63**, 2616–2629.

Thompson, D. W. J. and S. Solomon, 2005: Recent stratospheric climate trends as evidenced in radiosonde data: Global structure and tropospheric linkages. *Journal of Climate*, **18**, 4785–4795.

Thompson, D. W. J., S. Solomon, P. J. Kushner, M. H. England, K. M. Grise, and D. J. Karoly, 2011: Signatures of the Antarctic ozone hole in Southern

Hemisphere surface climate change. *Nature Geoscience*, **4 (11)**, 741–749, doi: 10.1038/ngeo1296.

Thouret, V., J.-P. Cammas, B. Sauvage, G. Athier, R. Zbinden, P. Nédélec, P. Simon, and F. Karcher, 2006: Tropopause referenced ozone climatology and inter-annual variability (19942003) from the MOZAIC programme. *Atmospheric Chemistry and Physics*, **6 (4)**, 1033–1051, doi:10.5194/acp-6-1033-2006.

Waugh, D. and T. M. Hall, 2002: Age of stratospheric air: Theory, observations, and models. *Reviews of Geophysics*, **40 (4)**, 1010.

Waugh, D. W., 2009: Atmospheric dynamics: The age of stratospheric air. *Nature Geoscience*, **2**, 14–16.

Wernli, H. and M. Bourqui, 2002: A Lagrangian 1-year climatology of (deep) cross-tropopause exchange in the extratropical Northern Hemisphere. *Journal of Geophysical Research*, **107 (D2)**, 4021.

Wilcox, L. and A. Charlton-Perez, 2013: Final warming of the Southern Hemisphere polar vortex in high- and low- top CMIP5 models Final warming of the Southern Hemisphere polar. *Journal of Geophysical Research*, **118 (6)**, 2535–2546, doi:10.1002/jgrd.50254.

Williams, G. P., 2006: Circulation Sensitivity to Tropopause Height. *Journal of the Atmospheric Sciences*, **63 (7)**, 1954–1961, doi:10.1175/JAS3762.1.

Wittman, M. a. H., A. J. Charlton, and L. M. Polvani, 2007: The Effect of Lower Stratospheric Shear on Baroclinic Instability. *Journal of the Atmospheric Sciences*, **64 (2)**, 479–496, doi:10.1175/JAS3828.1.

Yang, H., G. Chen, and D. I. V. Domeisen, 2014: Sensitivities of the Lower-Stratospheric Transport and Mixing to Tropical SST Heating. *Journal of the Atmospheric Sciences*, **71 (7)**, 2674–2694, doi:10.1175/JAS-D-13-0276.1.

Yang, H., L. Sun, and G. Chen, 2015: Separating the Mechanisms of Transient Responses to Stratospheric Ozone DepletionLike Cooling in an Idealized Atmospheric Model. *Journal of the Atmospheric Sciences*, **72 (2)**, 763–773, doi:10.1175/JAS-D-13-0353.1.

Yang, H., K. Tung, and E. Olaguer, 1990: Nongeostrophic Theory of Zonally Averaged Circulation. Part II: Eliassen-Palm Flux Divergence and Isentropic Mixing Coefficient. *Journal of Atmospheric Sciences*, **47 (2)**, 215–241.